The Dissertation Committee for Matthew Chu Cheong
certifies that this is the approved version of the following dissertation:

# Model-Based Decentralized Optimal Control of a Microgrid

Committee:

Dongmei Chen, Supervisor

Efstathios Bakolas

Pengwei Du

Matthew J. Hall

Carolyn Seepersad

# Model-Based Decentralized Optimal Control of a Microgrid

**by**

**Matthew Chu Cheong**

**DISSERTATION**

Presented to the Faculty of the Graduate School of

The University of Texas at Austin

in Partial Fulfillment

of the Requirements

for the Degree of

**DOCTOR OF PHILOSOPHY**

THE UNIVERSITY OF TEXAS AT AUSTIN

August 2019

Dedicated to my dog, Vanilla, and Katie.

# Acknowledgments

I would like to thank those who have helped me through this journey. It is no understatement to say that this has been the most difficult endeavor in my life to date; perhaps that is the mark of a blessed life. At the time of writing this, the status of my defense is unknown. But 'win or lose,' the time, effort, and support I've received has helped me immeasurably.

To my advisor, Dongmei Chen, without whom I would likely have studied something completely different- thank you. Your creative research goals and insightful questions pushed me in ways I wouldn't have imagined, and in ways that will forever shape my thinking. This was in a lot of ways an unknown research area for the both of us, and I sincerely appreciated your wisdom in navigating the storm.

To my unofficial "co-advisor," Pengwei Du, thank you for your patience and experience. I came into this knowing nothing about power systems, which was a bold move, to phrase it positively. I'm sure my questions must have seemed elementary or trivial, and I sincerely appreciated not only your willingness to help, but your encouragement and support throughout the process.

To my other dissertation committee members, Drs. Carolyn Seepersad, Matthew J. Hall, and Efstathios Bakolas, thank you for taking the time to contribute to this process, and for your insightful questions that have helped shape my final research direction. I often wondered why a professor would ever agree to be a part of this process; it's time consuming

and burdensome. But I never felt as though I were an inconvenience, and quite the opposite, your guidance has provided invaluable outside perspectives to my research cocoon. Even in the classroom, Dr. Bakolas' humor and mathematical intuition sparked a real passion for many of the fundamental concepts I've worked with over these years.

Outside the academic spectrum, I of course need to thank my parents and siblings for being there for me, clichéd though it may be to say. I intentionally avoided discussing my research with my family, but they were always available to talk with me and laugh with me, regardless of the topic, and that has made this process immensely more bearable. However this ends, I hope you can be proud.

To Katie, I love you and thank you. There have been so many times I've wanted to quit, or where I've felt as though I wasted my time, or that my research was a failure, or that my code would never work (the list goes on). And at every turn you've been there to put me back on track, to support me, and to encourage me to keep going. I only hope I can help you in the same way one day.

To Vanilla, I love you too buddy. I know you can't read, but you've been at my side every day, every hour of this process. You've bitten and scratched me more times than I can count, but you keep me grounded in ways that I don't think dogs can understand.

# Abstract

## Model-Based Decentralized Optimal Control of a Microgrid

Matthew Chu Cheong, Ph.D.
The University of Texas at Austin, 2019

Supervisor: Dongmei Chen

Power networks have experienced dramatic changes with the growth of renewable energy and 'smart' grids. To accommodate the challenges posed to traditional power system control architectures, the microgrid concept has gained traction. Microgrids are small-scale power networks that can disconnect from the main grid and operate autonomously if necessary. These systems add robustness and facilitate the incorporation of renewable power, but they face control challenges of their own due to the lack of significant inertial generation. Without the main grid to provide balance, the high proportion of electrically-interfaced power resources can cause significant deterioration in microgrid stability.

This dissertation proposes designs to improve decentralized control in microgrids; model based information is incorporated into controllers and estimators to more optimally guide control signals, while still only using local data for real-time computation.

We outline the role that microgrid topology can have on stability, and how judicious power injection can mitigate instabilities. These results are extended to a decentralized

H-infinity control design for microgrid frequency; even with limited model-based information and controller distribution, the design offers significant improvements over traditional controllers.

Building upon the idea of microgrid stabilization, we also present a control method by which a wind turbine can be coordinated for microgrid support. The wind turbine is used as a controllable power source by utilizing the rotational energy stored in its rotor; this design incorporates an aerodynamic wind turbine model and a novel optimal blade pitch angle controller to ensure stable turbine operation. This allows for rapid power injection for grid support.

This theme concludes with a decentralized estimation scheme to facilitate coordinated control across a microgrid using only local data. We leverage the frequency synchronization and load-sharing intrinsic to the microgrid so that local measurements can provide insight about grid-wide conditions. This allows for effective implementation of optimal filtering techniques so that remote conditions can be estimated using only local data; this allows for grid-wide coordination and optimization. Together these ideas represent the concept that the microgrid model, even in a limited and inaccurate sense, can be manipulated to provide significant benefits for decentralized control across the network.

# Table of Contents

# List of Tables

# List of Figures

# Chapter 1

# Introduction

The focus of this dissertation is on decentralized estimation and control in islanded microgrids. The results presented here will allow these systems to operate robustly and stably with high penetrations of distributed and renewable power resources.

Microgrids are small-scale power networks that may disconnect from the main grid and operate autonomously. This islanding feature allows microgrids to better recover from grid failures, but it also complicates the associated control challenges. Microgrids typically have a much higher penetration of electrically interfaced distributed energy resources which facilitate this autonomous operation. These sources, such as wind turbines or photovoltaic arrays, lack physical inertia since they do not possess the large spinning rotors of traditional generators; microgrid disturbances result in swings in power quality, and threaten the stability of these networks.

The research in this dissertation explores how we can optimally control microgrids to better address this issue. The designs outlined in this work are constrained by the physical obstacles and requirements posed by a microgrid; microgrid power sources are expected to be 'plug and play,' and data transmission between controllers is limited at best.

First, we explore how H-infinity control methods may be used for decentralized model-based control in microgrids. Controllers utilize the full microgrid model to guide their control

decisions, but real-time operation of the synthesized controller is constrained to only use local sensor data. These methods are used to improve voltage and frequency stability in islanded microgrids.

We then explore decentralized power injection in a traditionally controlled microgrid- we control only one of the power sources in a microgrid to identify the limits of control in these systems. We outline the role that microgrid and controller topology may have in terms of the limits of controlling the transient response.

We expand upon these topics by then proposing a decentralized improvement to the droop method, where instead of explicitly controlling the power supplied to the microgrid, we change the droop control command. This new design maintains the steady-state power sharing that makes droop controllers attractive, but improves the transient microgrid performance and stability. In addition, it allows for seamless integration in a traditionally controlled microgrid, offering notable improvements even when the microgrid model is not entirely available or not all inverters can be equipped with this new design.

These methods so far present ways that power quality can be improved without modifying the total power supplied to the system. We then explore how wind turbines may be used to add power to the system so as to improve the microgrid stability: we design a control method to allow wind turbines to act as a robust, controllable power source in order to provide frequency support to a microgrid. The power electronics in a wind turbine allow for fast power injection for grid support, where this power injection is balanced against wind turbine operation constraints, power output, and stability criteria, in order to ensure stable control.

Finally we expand upon the wind turbine controller, by presenting a decentralized estimation scheme for microgrid applications. This method allows for state estimation of the full microgrid using only local measurement data; for this we leverage the idea that there is intrinsic synchronism in a power system, and thus local measurements provide some insight into system-wide measurements. This estimation allows for coordinated control, as with the wind turbine, by providing local controllers with a communication-free means for state estimation.

This work provides insight into how model-based designs can be used to significantly improve microgrid performance, and allow for features not typically encountered in these networks. The results provide means to significantly improve microgrid stability and robustness, using only the sensor data and infrastructure that is presently available in these systems. This in turn will allow for increased security in these networks, and will facilitate higher renewable energy penetration.

# Chapter 2

# Background

As this research deals with methods for the control of microgrids, the goal of this section is to provide some context for this problem. This section defines microgrids and their relevance to modern power systems. In addition microgrid control will be reviewed, starting with what it means for a power system to be stable. This section concludes with a review of control methods in microgrids, particularly as they have motivated the presented research.

## 2.1 Microgrids and Associated Challenges

As society advances, renewable energy continues to advance and become more economically feasible. The increased penetration of renewable energy has been coupled with the growth of distributed generation [1], which refers to locally-situated power generation from a variety of sources that include micro-turbines, photovoltaic arrays, wind turbines, and fuel cells. This contrasts with centralized generation plants, such as coal and natural gas plants, which are often remotely located [2]. Distributed energy resources (DERS) can be used for power support at substations and onsite generation, and combined with their lower emissions and costs can offset the advantages usually associated with economies of scale [2].

Unfortunately this growth has been coupled with challenges for power networks.

While the redundancy and locality of distributed generation improves the robustness and efficiency of power networks, at the same time the increased number of power sources is challenging from a control perspective. Coordinating a large, growing number of power sources poses an extraordinary control challenge for utility operators that have been designed to handle a fairly fixed number of power supplies.

In addition to the sheer number of controlled power sources, the growth of distributed generation challenges the conventional control architecture in power systems. Power grids traditionally have a hierarchical structure, where the most complex control systems with the greatest automation are used at the high voltage levels [3]. This system has been effective for centralized generation, when the overwhelming bulk of power generation has taken place at this voltage level. However, more DERs at the low and medium voltage levels now demand this same level of control complexity, and so grids are unequipped to handle the associated control tasks. Without appropriate control, modern power systems will be otherwise forced to limit the growth of renewable and distributed power.

To address these issues, the idea of a microgrid has been explored. A microgrid is a small-scale interconnection of distributed energy resources (DERs) and loads with distribution voltages ranging from 1 kV up to 69 kV [1]. Microgrids can operate in two main modes: grid-connected mode, or islanded mode. When a microgrid functions as an island, it disconnects from the main power grid and operates as an autonomous unit.

While the unique aspects of a microgrid are more prominently featured during islanded operation, grid-connected operation is an essential feature of these systems that can facilitate higher renewable energy penetration. As previously mentioned, as the proportion of DERs increases, the centralized control task becomes more heavily burdened. To mitigate

this control challenge, a microgrid operator can aggregate its local DERs and loads and then respond to signals from the main grid [4]. In this scenario, the main grid can send and receive high-level signals about power imbalances to and from the microgrid, while the microgrid controllers can then supervise the local energy generation and demand [2]. From the perspective of the main grid, it is notably easier to deal with this hierarchical form of control rather than having to individually handle these local sources and sinks.

Islanded operation, on the other hand, is featured whenever the microgrid disconnects from the main grid and functions autonomously. Islanded operation may occur in order to avoid faults from the main grid, or to allow for planned maintenance [4, 2]. In this scenario, the microgrid is entirely responsible for managing its local power balances; without the main grid to serve as a power reservoir, this control problem is nontrivial.

Islanded control is challenging primarily due to a combination of the scale of the microgrid as well as the nature of its power sources. Compared to a large-scale grid, a microgrid is more sensitive to any given power disturbance or fault due to its small system inertia. In a conventional power system, much of the power is provided by synchronous generators which have heavy, spinning rotors. This introduces a significant amount of physical rotational inertia into the system. When these networks experience disturbances, whether they may be from load changes, supply variations, or grid faults, the angular momentum in these rotors dampens the overall system response [5]. This inertial response adds robustness to the system in that it prevents rapid swings in the network frequency [6]; this is a highly desirable feature in a network whose stability relies upon synchronized operation at a set frequency. A microgrid, on the other hand, has a higher proportion of its power provided by electrically-interfaced sources. Solar panels, for example, provide power without any mov-

ing parts and thus lack the same degree of physical inertia. Similarly, wind turbine rotors are typically physically decoupled from the power network and provide power without any inertial support. With a lower proportion of synchronous generation, microgrids have less inertia, and thus experience more pronounced power quality deviations.

These problems are exaggerated by the scale of microgrids as well as the inherent intermittency of renewable generation. With fewer overall components in the microgrid, individual faults and disturbances are less dampened and proportionally more disruptive. The intermittency of renewable generation adds to this issue, as it can complicate the problem of power scheduling; if a significant portion of power is supplied by renewable sources, then more robust control may be necessary in order to accommodate this intermittency. To exemplify the challenge associated with renewable sources in microgrids and the need for more robust control, [7] has identified that minimum amounts of synchronous generation may fundamentally be necessary in such power systems to maintain grid stability.

Despite these issues, the islanded feature of microgrids offers significant advantages towards robustness and efficiency in power networks. Microgrids may intentionally be islanded, to allow for planned maintenance [8]; they may also be islanded due to unplanned faults. During natural disasters microgrids can offer self-sufficiency in times when grid blackouts may otherwise lead to cascading failures, and can significantly expedite the recovery process. For example, during Hurricane Sandy in 2014, Princeton university was able to stay powered due to its 15 MW microgrid, even as neighboring communities lost power [9, 10]. This advantage is particularly important for rural or isolated communities, where disaster recovery is often slow; an experimental 5 MW microgrid in Borrego Springs, California, was able to restore power within hours, following the destruction of a transmission line by a

lightning strike [9].

With this in mind, microgrids simplify the control of DERs and accommodate the projected growth of renewable technologies, while simultaneously adding robustness to power networks. However they come at a cost; controlling microgrids is challenging, particularly due to the high penetration of electrically interfaced power sources, renewable or otherwise. We discuss methods and results for the islanded control of microgrids, where the lack of inertia makes power stability a conspicuous issue.

## 2.2 3-Phase Power System Overview

Before going into the control of power networks, we first clearly outline what exactly needs to be controlled. Voltages and currents in AC systems are periodic, with a characteristic frequency, $\omega$; in the United States, this is set at 60 Hz, while the European standard is 50 Hz. AC power can be broken down into active, reactive, and apparent power. This can be formally represented by:

$$\begin{aligned} I(t) &= I_{max}(\sin\omega(t) + \phi_I) \\ V(t) &= V_{max}(\sin\omega(t) + \phi_V) \end{aligned} \tag{2.1}$$

where power is represented as

$$\begin{aligned} \text{Apparent: } S &= I_{RMS}V_{RMS} \\ \text{Active: } P &= S\cos\phi \\ \text{Reactive: } Q &= S\cos\phi \end{aligned} \tag{2.2}$$

In the above equation note that RMS refers to the root-mean-squared value of the sinusoidal quantity, while $\phi$ refers to the phase difference between current and voltage.

Power quality in AC power systems refers to the ability of the grid to maintain a consistent and smooth voltage waveform which alternates at the desired nominal frequency. The goal is to deliver power that has a steady frequency at its nominal value, with a consistently sinusoidal waveform [5].

Losses in power quality occur during power imbalances or routine usage. Generators inject power at a given voltage magnitude, and this voltage level drops as consumption increases further along the associated power lines. Similarly, frequency deteriorates with power imbalances; when active power consumption exceeds supply, frequency drops and when active power supply exceeds demand, frequency increases. To maintain high power quality standards, controllers tend to focus on some combination of this voltage problem and the frequency/power-sharing problem.

The power systems and models discussed in this work, as well as those referenced in the majority of the cited research, focus on 3-phase AC networks. AC signals are sinusoidally time-varying, which can make these 3-phase models challenging for use in control. Naturally, it is more challenging to deal with quantities that oscillate in time, so to simplify these calculations, the direct-quadrature-zero (DQ0) transformation is frequently used in the following discussions. This transformation will be briefly explained to avoid confusion when referencing later models.

The intention is to transform the stationary reference frame of these sinusoidal signals to a rotating reference frame; in this rotating reference frame, the signals appear as DC signals, which in turn simplifies analyses [5, 11]. This process is referred to as the DQ0 transform, and a visualization is shown in figure 2.1.

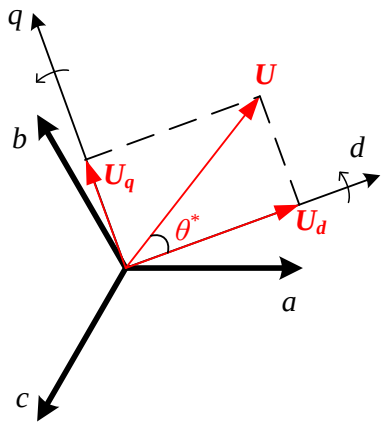


Figure 2.1: A geometric interpretation of the $abc$ to $dq0$ transformation, where the $dq0$ frame rotates at the frequency $\omega$ instead of remaining stationary.

By convention, 3-phase AC circuits are described on the $abc$ coordinate system; a 3-phase signal $u$ is comprised of components $u_a, u_b, u_c$. The dq0 transform, to shift to the $DQ0$ reference frame, is given by [12]

$$\begin{bmatrix} u_d \\ u_q \\ u_0 \end{bmatrix} = \begin{bmatrix} \cos(\theta) & \cos(\theta - \frac{2\pi}{3}) & \cos(\theta + \frac{2\pi}{3}) \\ -\sin(\theta) & -\sin(\theta - \frac{2\pi}{3}) & -\sin(\theta + \frac{2\pi}{3}) \\ \frac{1}{2} & \frac{1}{2} & \frac{1}{2} \end{bmatrix} \begin{bmatrix} u_a \\ u_b \\ u_c \end{bmatrix} \tag{2.3}$$

In this transformation, the $d$ and $q$ axes rotate about the 0-axis, which remains stationary. This can be visualized in figure

The advantage of this transformation is that it simplifies calculations, which in turn simplifies the ensuing control design. Power, for example, can be computed in a manner that is reminiscent of single-phase DC systems. For a current $I$, across a voltage drop $V$, the active and reactive powers are given as

$$\begin{aligned} P =& V_d I_d + V_q I_q \\ Q =& V_q I_d - V_d I_q. \end{aligned} \tag{2.4}$$

This reduces the challenge of having to deal with a time-varying sinusoidal component.

## 2.3 Stability and Control in Power Systems

Power systems have well-defined notions of stability, along with different types of control to address various aspects of grid stability. The two main types of stability are *steady-state* and *dynamic*.

Steady-state stability refers to the system's ability to supply all loads in the network with power, while maintaining synchronism among all connected components. Alternatively, dynamic stability, or transient stability, refers to how the system responds to disturbances; a system that can return to an equilibrium following a disturbance is considered to be dynamically stable. From the perspective of dynamic systems and controls in mechanical engineering, dynamic stability in power systems is analogous to the traditional ideas of stability, where stability can be investigated via eigenvalue analysis.

To illustrate this idea of dynamic stability, consider a traditional power source with a turbine and a rotor. An increase in the load results in a slowed generator and thus a lowered frequency; to maintain a constant frequency, the active power output can be raised by increasing the torque on the rotor. However in an interconnected network comprised of multiple such sources, like a microgrid, the action by any individual generator affects the other connected power sources. Synchronous generators in an AC system ideally rotate at the same frequency, in phase with each other. For small perturbations, generators that rotate faster experience a greater load, while generators that rotate slower experience a smaller load; therefore there is a restoring force to maintain stability. However, this only holds to a point; if the rotor speeds up excessively, this energy cannot be readily dissipated and the

generator cannot return to its equilibrium. This exemplifies the idea that a goal of frequency control is for frequency disturbances to be as small as possible, to maintain stability in these power systems.

Related to these ideas of stability, control in power systems is generally divided into three main timescales: primary, secondary, and tertiary control. Primary and secondary control are concerned with dynamic stability, while tertiary control deals with steady-state stability.

Primary control seeks to stabilize the network immediately following a disturbance. The goal here is typically to ensure that the system can maintain dynamic stability, and so these controllers are concerned with the first 20-30 seconds following a perturbation.

Primary control action usually results in some amount of steady-state error. For example, an unexpected variation in load can result in an unscheduled imbalance between supply and demand. After the primary controllers have stabilized the dynamics of the power system, the goal of secondary control is then to determine how to best restore the network to specified setpoints. This typically takes between 5 to 10 minutes. In microgrids, secondary controllers may also focus on stabilization following islanding from, or reconnection to, the main grid.

Tertiary control is focused on power scheduling and planning, and trying to predict how much generation will be required to meet upcoming demands. The projected windows can be anywhere from hours to days.

This research is focused on the dynamic stability of microgrids, and as a result the timescales of interest will generally center on primary control in these networks.

## 2.4 Primary Control in Microgrids

A significant challenge at the primary control timescale in microgrids is focused on how to best handle inverter-connected power sources. Unlike conventional power sources, inverter-connected DERs lack physical inertia, which in turn exacerbates the frequency regulation problem in power systems. As a result these networks can lack the same robustness expected from traditional power systems.

In typical grids, the majority of power is supplied via synchronous generation which converts mechanical power to electrical power with a specified frequency. In this scheme, mechanical power is exerted to physically turn a rotor in a magnetic field; this in turn delivers power [5]. Steam turbines, gas turbines, and hydroelectric plants are typical examples of synchronous generators that are used to deliver usable electric power for an AC power system. As mentioned earlier, these sources add inertia to the network due to their physically spinning components; the frequency at which the rotor spins is proportional to the frequency of the output power.

On the other hand, inverter-connected sources are electrically-interfaced generators that do not have a physical coupling between their power generation and the associated frequency of their injected power. Instead, these generators rely on an inverter to set the desired waveform of their output power so that it can be used in an AC power system. Wind turbines, batteries, and PV arrays are common examples of inverter-connected sources; unlike turbine-driven systems, they intrinsically lack moving parts.

A significant challenge in microgrids at the primary timescale is how to deal with the control of inverter-connected sources, and how these sources affect the stability of the

network. The physical dynamics of synchronous generators intrinsically result in a degree of damping and feedback control at the primary timescale [5]. While inverter-connected DERs can supply power, they fail to contribute rotational inertia to the system. Therefore when synchronous generators make up a smaller proportion of overall power generation, a greater responsibility is placed on the remaining 'physical' power sources to maintain frequency stability during unplanned disturbances. Primary control in microgrids therefore tends to be focused on how we can more intelligently control inverter-connected sources so that the overall system can be better stabilized even without physical inertia to dampen these disturbances.

A necessary theme in this design process is modularity. A higher penetration of distributed generation means that there are more points of generation, which in turn means that components are expected to be frequently connected to or disconnected from the network. As microgrids are intended to be robust, these components should be able to be easily added and removed [4, 2, 1].

As a result, centralized controllers are not well suited for microgrid operation. Centralized controllers rely on information about the full state of the microgrid, and assume that individual controllers will operate with this knowledge. In many control schemes, this is a common and reasonable assumption; a vehicle control system, for example, should operate using data from its brakes, speedometer, accelerometer, temperatures, etc. However this type of control is limited for microgrid applications, as the system has numerous generation sources and it may be infeasible to rely upon real time communication between all generators all the time [13]. To return to the vehicle example, it would be analogous to expecting a car to know the state of every other vehicle on the road- a high bar.

Instead, decentralized controllers operate based on local information. In the context of a microgrid, this means that individual generators can operate without knowing the state of every other generator and load. This is much more tractable in terms of sensor and bandwidth constraints in microgrids. That said, there is a tradeoff in that with less available data, decentralized controllers may perform suboptimally relative to the centralized case. Moreover, care must be taken during the interconnection of these controllers; a decentralized controller may be individually stable on the local level, but may result in an unstable overall system [14].

With these constraints, the standard for primary control of inverter-connected sources in microgrids is droop control [11]. This method is both simple and decentralized, and allows droop-controlled sources to be easily added/removed to the grid in a "plug and play" fashion [4]. Droop controllers use local measurements of active and reactive power to adjust the output voltage and frequency of the controlled inverter. In the most common implementation [11], active and reactive power are decoupled in terms of their effects on frequency and voltage:

$$\begin{aligned} \omega &= \omega_0 + m(P - P_0) \\ V_d &= V_{d,0} + n(Q - Q_0), \end{aligned} \tag{2.5}$$

where $P$ and $Q$ refer to active and reactive power, while $P_0$ and $Q_0$ refer to their respective nominal setpoints. In actual implementation, this fundamental controller is coupled with additional voltage and current controllers, as illustrated in figure 2.2. These controllers are meant to ensure that the commanded reference values are tracked, and to damp the oscillatory harmonics from the resulting power injections.

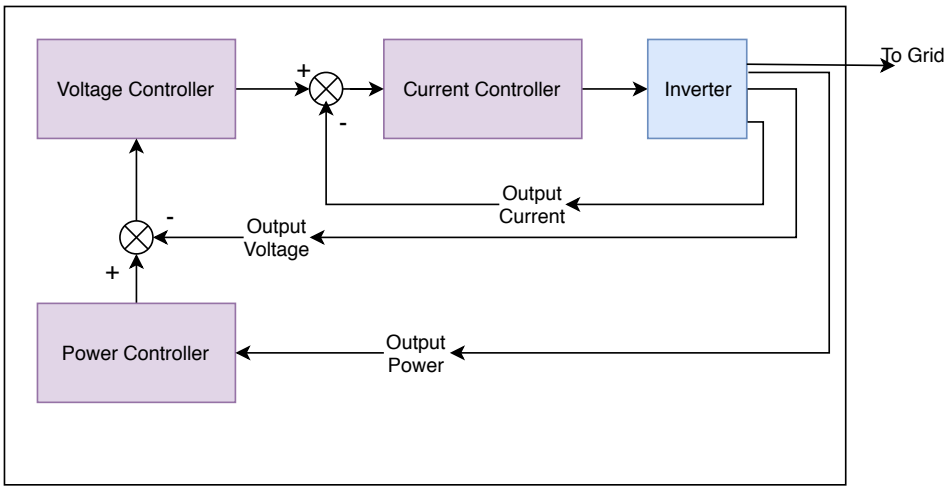


Figure 2.2: Block diagram representing feedback structure in a droop-controlled inverter.

Droop control is the most common type of control for inverter-connected sources because it is both simple and streamlined. The control is decentralized and requires minimal sensor data; fundamentally only two power measurements are required. In addition droop control can be used to enforce proportional power sharing between inverter-connected sources, in the sense that the power demands of the system can be proportionally distributed depending on the rating of the individual power sources. Tuning the droop gains, $m$ and $n$, results in steady-state power sharing that is proportional to the gain.

However droop control is not without its faults. Ultimately the controller is a simple proportional controller, and so persistent disturbances or load changes result in steady-state error. In addition, this control methodology is designed for steady-state power sharing, and so tends to lack robustness and presents poor transient behavior such as excessive ringing [13, 15].

There have been proposals to improve the transient performance in droop-controlled

microgrids, as in [16, 17, 18]. The general idea in these designs is to adjust the linear droop law by adding terms proportional to the derivative of the active power or reactive power, to better address transient characteristics. In this way, the added terms decay to zero at equilibrium, ensuring that the steady-state behavior of the original droop controller is unchanged. However these methods are limited in how these droop adjustments are computed and incorporated. The new terms are only proportional to $\frac{dP}{dt}$ and $\frac{dQ}{dt}$, and therefore there is less modulation available for control. In addition, the control gains are determined (1) entirely by considering the individual inverter, irrespective of microgrid topology; (2) by pole placement techniques and experimental tuning. These methods are effective in isolation, but face challenges in terms of being reproducible in various microgrid topologies and configurations, particularly in terms of being optimal.

Alternative decentralized control techniques in microgrids have been considered, but the focus in those works is often on controlling microgrids with a single DER, or on applying local control laws on a generator-by-generator basis [19, 20, 21]. As will be later outlined, a number of H-infinity controllers applied for microgrids also fall into this category. A significant challenge associated with these lines of research is that it can be difficult to predict performance, robustness, or stability when more than one DER is connected to the microgrid, as this scenario was not included in the original design. This may not be an issue for conventional synchronous generators which operate on slower timescales, but for microgrids with inverter-interfaced DERs, grid dynamics should not be ignored [11]. The dynamics associated with grid interconnections, i.e. resulting from line inductance, may be ignored with slower generators, but inverter-interfaced sources operate on similar timescales to these grid dynamics, and thus the grid should be considered during stability analysis and

design.

Master-slave controllers have been proposed as distributed methods for microgrids, where a 'master' voltage-controlled inverter sends signals to other current controlled 'slave' inverters within the system [22, 23]. This approach can result in fast control, but has a fault with respect to robustness: the master control mechanism represents a single point of failure, which is unappealing in a system that demands robustness and modularity.

There is a need to improve the transient response for microgrid controllers, especially for microgrids with several generating units operating in parallel [19]. To address this problem, we present decentralized control methods in microgrids as well as control schemes to allow wind turbines to participate in microgrid control.

### 2.4.1 H-Infinity Control in Microgrids

This section provides some context for what is meant by H-infinity control, as well as relevant applications in microgrid research. The goal is not only to outline the utility of H-infinity methods in microgrid control, but also to identify some of the gaps in this past research to illustrate the motivation for the work later described in this dissertation.

H-infinity controllers represent a branch of optimal control, where the goal is to control the system of interest while simultaneously minimizing some quantity. In the H-infinity problem, the challenge is to minimize the effects of unwanted disturbances on our system. For microgrids, these methods can be used to minimize the impact that physical disturbances and parameter uncertainty may have on power quality and grid performance.

To frame this more concretely, suppose this system is linear and time-invariant. Generally the inputs can be considered as either controlled inputs $u$, or disturbances/exogenous

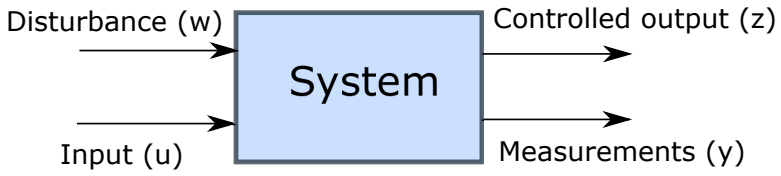


Figure 2.3: Representation of a plant with controlled and exogenous inputs, as well as controlled and measured outputs

.

inputs $w$; the outputs are measurements made available for control, $y$ as well as a set of 'controlled outputs' $z$. This general structure is shown in figure The goal of the H-infinity problem is to minimize the effect of $w$ on $z$, which is represented by minimizing the infinity norm of the transfer function from $w$ to $z$.

Intuitively, the infinity norm can be interpreted as the peak gain of the response. Formally the infinity-norm of a stable LTI system $G(s)$ can be found as the largest singular value over all frequencies:

$$\|G\|_\infty = \sup_\omega \bar{\sigma}(G(i\omega)) \tag{2.6}$$

This can be understood more intuitively by considering the analogous signal norm. For a given signal, $u(t)$, the 2-norm is commonly used in optimization problems where it appears in cost functions. The 2-norm of $u(t)$ is given as the integral of its absolute value.

$$\|u(t)\|_2^2 = \int_{-\infty}^{\infty} u(t)^2 dt. \tag{2.7}$$

If $u(t)$ represented the velocity of a particle, for example, then the 2-norm would be proportional to the integral of this particle's kinetic energy over time. Alternatively, the $\infty$-norm of the signal $u(t)$ is given as the least upper bound on $|u(t)|$:

$$\|u(t)\|_\infty = \sup_t |u(t)|. \tag{2.8}$$

In the velocity example, this infinity norm would simply reflect the greatest speed reached by the particle.

In this framework, the infinity norm of a system can be more easily interpreted. For a system $\hat{G}(s)$ the infinity norm is given by

$$\|\hat{G}(s)\|_\infty = \sup_\omega |\hat{G}(s)| \tag{2.9}$$

With this context, we can better understand the use of H-infinity control in microgrid applications. These controllers have been used to control power devices and power systems in the past. H-infinity methods have been attractive for microgrid control due to their tendency to result in more robustly controlled systems. Using H-infinity and $\mu$-synthesis techniques, authors in [24] found that these controllers contributed to a more robust microgrid compared to more traditional, optimal proportional-integral (PI) controllers.

The focus in [25] was on designing a voltage controller for a power resource connected to a microgrid based on H-infinity and repetitive control techniques. The paper was successful in that the proposed controller resulted in a rejection of harmonic disturbances and effectively handled nonlinear loads; the H-infinity techniques in particular allowed the controller to be robust to a range of load impedance That said, the focus was somewhat narrow in that it neglected the power or frequency control problems and focused only on handling voltage distortions in a microgrid. Moreover, the controller was designed for a single power converter, without considering the interaction with the remainder of the network.

A similar task was investigated in [26], which used H-infinity techniques to modify the closed-loop voltage dynamics of controlled inverters. Using these methods they were able to design a dual-loop controller that reduced voltage distortion while being robust to

load variations. However as before, this was also singularly focused on the voltage control problem and only on the behavior of a single inverter, rather than the dynamics associated with multiple devices operating in tandem as would be expected in a microgrid.

The aforementioned researchers were concerned with using H-infinity methods for the control of individual devices. However control in microgrids often involves coordination between various power sources. Therefore other works have followed that have continued to consider how to use H-infinity techniques to better coordinate the outputs from multiple power sources.

In [27], H-infinity control was used to coordinate the power outputs from a battery and a diesel generator, along with a nominally uncontrollable wind turbine, in order to better control frequency in the microgrid. It was found that compared to traditional PI controllers, the H-infinity methods resulted in a better suppression of frequency deviations. While this paper did consider various power sources operating alongside each other, there was only a single frequency-setting device and the interconnections between power sources were largely ignored. Similarly, [28] explored H-infinity methods as a means to coordinate a diesel generator with controllable loads in the form of electric water heaters, to mitigate frequency deviations in the microgrid. The resulting centralized controller did not result in a net decrease in power consumption, but the controlled system did show a significant reduction in frequency variability. Researchers in [29] used H-infinity and genetic algorithmic methods to coordinate the power outputs in a much larger microgrid, comprised of a variety of sources including wind turbines, diesel generators, fuel cells, and energy storage units.

Even in these examples, where multiple sources were considered, the microgrids were either assumed to be small and thus the controllers were centralized, or the models neglected

to account for the dynamics associated with DER interconnections. As noted in [14], ignoring the dynamics associated with interconnections may result in an a scenario where the overall system is unstable, even if the individual subsystems are stable on a local closed-loop level. These concerns are particularly relevant due to the increased sensitivity of microgrids, due to their lack of inertia. This idea was highlighted in [11], where the individual inverters were modeled alongside the interconnecting line dynamics, in order to evaluate the closed-loop stability and sensitivity of the full microgrid. The authors emphasized that neglecting the dynamics of interconnecting lines may be a reasonable simplification when dealing with more conventional and slower power sources, but that the fast dynamics associated with inverter controls meant that the microgrid interconnections have a significant impact on the overall network stability.

Despite this absence in the literature, the potential for the improved application H-infinity control remains. The contributions outlined later in this document will generally focus on two main aspects. First, the full dynamics and interconnections of the microgrid are considered during the modeling and control design process; the significance of this has been previously emphasized. Second, the microgrid is considered to have more than a single frequency-setting unit. Notably, many of the previous examples used a microgrid model in which a single power source was responsible for setting the frequency of the microgrid; the remaining power sources would then be responsible for supplying power as needed to result in a more optimal system. This type of system is somewhat easier to model and control compared to one in which there are multiple frequency-setting units. Synchronizing the operation between independent frequency-setting units can be challenging, particularly when power injections from controlled DERS affect these units asymmetrically due to microgrid

topology. That said, this sort of microgrid composition is a common and realistic case; with only one frequency-setting unit, the microgrid would suffer a catastrophic failure if it went offline for some reason. As a result, this configuration is considered for this research.

### 2.4.2 Wind Turbine Control for Power System Applications

A fundamental challenge associated with wind turbines and power quality is that wind turbines add variance and intermittency to the grid. Past research has focused on how to address this problem, to see if wind turbines can be effectively controlled to mitigate those intermittencies, or if wind turbines can be used to actively improve power quality.

Unlike synchronous generators whose frequencies are tied to that of the network, wind turbines are physically decoupled from the grid's frequency. In the most common implementation, wind turbines are connected to a power system via a doubly-fed induction generator (DFIG) that allows for variable-speed operation [30]. As a result, the rotor speed of the wind turbine is not tied to the frequency of the grid.

Moreover wind turbines, and renewable sources in general, tend to be controlled to provide maximum power depending on available conditions. When the penetration of renewable sources is low then this can be an effective strategy to best utilize these resources; low penetration would limit meaningful control strategies. However as renewable penetration increases, then this maximum power point tracking strategy can result in grid instabilities and more extreme vulnerabilities to intrinsic intermittencies [31, 32]; when this class of DERs contributes a greater proportion of power to the system, then its effect on grid stability and power quality is non-negligible [7].

The recognition of these problems has gained traction in various power regulatory

committees. In some cases, this has been implemented into policy, where renewable DERs are now required to have some amount of control over their power output, to help counter frequency disturbances [33]. In Ireland, for instance, wind farms are mandated to have curtailment capabilities on their active power output, and individual wind turbines must possess a minimum response rate for these controllable functions [34]. Similarly in Denmark, another country with a high penetration of wind power, wind turbines are required to maintain an active power reservoir in order to track reference power setpoints [35]. Even in Canada, where wind energy is not as commonplace as Denmark or Ireland, grid operators recognize the challenges associated with large influxes of wind power. In Quebec, large wind farms rated above 10 MW are required to be able to control their active power output for at least 10 seconds following grid frequency errors exceeding 0.5 Hz [36].

Following suit, research has focused on how to address these issues to allow wind turbines to be more effectively integrated into power systems. Although renewable DERs typically do not contribute to the inertia of a power system, wind turbines possess a significant amount of inertia due to their rotating rotors and blades. While this inertia is typically 'hidden' from the grid because modern variable-speed wind turbines are physically decoupled from the grid frequency, this feature has been investigated to better control the power output from wind turbines.

Early investigation in [37] identified that the rotational inertia stored in a wind turbine could be theoretically used to inject power into the grid for primary frequency control efforts. The authors readily acknowledged a significant limitation, in that the rotational inertia of the wind turbine was finite and could not be used for extended frequency control efforts. To offset this drawback, they proposed a hybrid controller in conjunction with a fuel cell in

[38]. The challenge posed by fuel cells is that they can possess a slow response time when hydrogen has to be obtained from fuels like natural gas. The proposition in [38] was to use the inertial power injection from wind turbines during these slow transient periods of the fuel cell; in this way, the primary frequency control from the wind turbine would not be relied upon for extended times, and the slow response from the fuel cell would be compensated for.

Unfortunately this research was limited by the models used, and ignored the stability of the wind turbine. While the authors presented a novel approach for inertial emulation and frequency control, the limitation was that actual aerodynamic features of the wind turbine were ignored. Instead, the wind turbine was treated as a black-box that traded off between output power and rotor frequency. This approach is effective for theoretical estimates, but these models ignore the real issues associated with wind turbine operation and stability. Overspeeding and underspeeding are both issues that need to be considered during safe operation of a wind turbine. For example, when rotational inertia is drawn from a wind turbine to increase its output power, its rotor speed will decrease. When the rotor speed decreases, the efficiency of the wind turbine may also decrease; to maintain the same overall power output in this scenario, even more rotational inertia would need to be drawn. This can result in a critical slowdown, where the wind turbine falls below its cutoff speed and needs to be shut down and/or disconnected from the grid until it can return to its nominal operating point. If these issues are neglected during the controller design process, the resulting control methodology will not be robust to variable operating conditions. With this in mind, similar problems can be identified in related research.

Other methods attempt to minimize stability issues by operating the wind turbine in a deloaded way, as in [39, 40] and [41]. In this approach, the wind turbine outputs such that

a designated power reservoir is available. During conventional operation the wind turbine outputs less power than what is available; the remainder power serves as a controllable reservoir, which the wind turbine may use for grid support. This offers a means for stable wind turbine operation because the wind turbine only uses its designated 'power reservoir' for control, but can drastically affect system efficiency. Deloaded operation means that the turbine generally only outputs a fraction of what is actually possible; without sufficient storage, the remainder energy typically goes unused.

In some cases, authors have considered using energy storage in conjunction with wind turbines in order to effectively utilize wind power for controllable power [42, 43, 44, 45]. This approach would have energy storage systems, such as batteries or supercapacitors, operating in tandem with wind turbines for efficient operation; excess energy from the wind turbine could be stored and later used for control or as desired. Unfortunately these methods are prohibitively expensive given the current state of energy storage technology, and the reserve capacity that would be required for such applications [46].

In conclusion, wind turbines present a promising potential source of controllable power. However past methods have been plagued with issues ranging from lack of stability, to loss of efficiency, to infeasible costs.

## 2.5 State Estimation in Microgrids

In this section we provide some context for state estimation in microgrids. We review fundamental state estimation concepts that are later applied to the microgrid control problem. We also discuss the role of state estimation in present microgrid research, and the extent to which it is used for control purposes. As will be discussed, control-oriented state

estimation is not typically encountered in microgrid applications.

In this document we frequently refer to the state space of a system, in which the modeled variables are treated as a set of first-order differential equations. The system of interest is modeled as a dynamic 'state,' $x = x(t)$, with associated control inputs $u$ and disturbances $w$. In this sense, the dynamics governing all time-varying components of our model are modeled as differential equations that are functions of the state itself, $x$, and the inputs $u = u(t)$ and $w = w(t)$:

$$\dot{x} = f(x(t), u(t), w, t)(t), \tag{2.10}$$

where the dot notation is used to represent time derivatives. For linear models, this can be represented as

$$\dot{x} = A(t)x + B(t)u + G(t)w, \tag{2.11}$$

where $A(t)$, $B(t)$, and $G(t)$ are linear matrices determined by the linearization of $f$. For the applications in the following research, the model $f$ is generally time-invariant in the sense that the model is not an explicit function of time

$$f(x(t), u(t), w(t), t) = f(x(t), u(t), w(t)). \tag{2.12}$$

As a result, the linearized matrices are also invariant with respect to time; $A(t) = A$, $B(t) = B$, $C(t) = C$.

Outputs from this system, such as the measured signals $y(t)$, can also be written as functions of this state and input, as well as potential measurement noise or error $h$:

$$y(t) = g(x(t), u(t), h(t)), \tag{2.13}$$

or after linearization:

$$y(t) = Cx(t) + Du(t) + h(t). \tag{2.14}$$

There are often elements of the state which are relevant to our interests, yet are not or cannot be reliably measured. In such situations, *state estimation* techniques are implemented. When we refer to state estimation or filtering, we mean the ability to obtain an approximation or estimate of a state, based on past measurements [47]. For some cases, state estimation may be necessary in order to understand the propagation of an unmeasured state variable; in other cases, a state variable may be directly measurable, but the measurements may be unreliable or noisy, and thus need to be 'filtered' to better match the actual state.

In designing an estimate of the state, $\hat{x}$, a key idea is that the system model can be used in conjunction with a set of measurements, $y$, in order to reconstruct a meaningful approximation The dynamics of the filtered estimate, or the observer, can be modeled as

$$\begin{aligned} \dot{\hat{x}} &= A\hat{x} + Bu + L(y - \hat{y}) \\ \hat{y} &= C\hat{x} + Du, \end{aligned} \tag{2.15}$$

where $L$ is an observer gain matrix designed to weight the measurements against the known model dynamics. If the sensor readings are known to be particularly unreliable, for instance, it may be more useful to rely upon the modeled dynamics rather than the raw measured data; this insight can be incorporated into $L$ depending on the design procedure.

So as to provide usable information, we require that the state estimator is stable in the sense that the estimator error remains bounded. A stable estimator is only possible if the system is at least detectable; the unstable modes of the system must be measurable in some sense [48]. If the system is detectable, then an estimator can be found such that the

error propagates as

$$\begin{aligned} e &= x - \hat{x} \\ \dot{e} &= (A - LC)e + Gw - Lh. \end{aligned} \tag{2.16}$$

The challenge is then choosing $L$ such that $A - LC$ is Hurwitz, so that the estimator error converges to 0. Various methods exist for the selection of $L$, either through explicit pole placement techniques or via optimization to minimize uncertainty as in the case of the Kalman filter [49].

For the problems outlined later, we refer heavily to a specific type of state estimation technique known as the Kalman filter. If the estimated system is linear, and the system disturbances $w$ and measurement noise $h$ are zero-mean and Gaussian, i.e. white noise, then the Kalman filter provides optimal state estimation [49]. While it is not the intention or role of this section to outline the derivation and proofs of the Kalman filter, we will briefly describe the 'tuning' and design aspects associated with this estimator, as these play an integral role in our methodology.

The Kalman filter can be interpreted as the optimal estimator in the sense that it minimizes the mean square error, $P(t)$, associated with the estimated $\hat{x}(t)$:

$$P(t) := E[(x(t) - \hat{x}(t))(x(t) - \hat{x}(t))^T], \tag{2.17}$$

where $E[\gamma(t)]$ refers to the expectation value of $\gamma(t)$. For the sake of exposition, we will assume that the aforementioned disturbances $w(t)$ and $h(t)$ represent zero-mean random variables. As such, $w$ and $h$ are associated with covariance matrices $Q(t)$ and $R(t)$:

$$\begin{aligned} Q(t)\delta(t - t^*) &= E[w(t)w^T(t^*)] \\ R(t)\delta(t - t^*) &= E[h(t)h^T(t^*)]. \end{aligned} \tag{2.18}$$

The optimal estimator in this case can be proven to have the form of a linear observer [50]:

$$\frac{d}{dt}(\hat{x}) = A\hat{x} + Bu + L(y - C\hat{x}), \tag{2.19}$$

where the observer gain $L(t)$, can be obtained as

$$L(t) = P(t)C^T R^{-1}. \tag{2.20}$$

The estimation covariance, $P(t)$, propagates as

$$\frac{d}{dt}(P(t)) = AP + PA^T - PC^T R^{-1}(t)CP + GQ(t)G^T, \tag{2.21}$$

and so if the disturbances are stationary noise where $Q(t) = Q$ and $R(t) = R$, then the observer gain can be obtained by solving for $P$ implicitly defined in the algebraic Riccati equation:

$$0 = AP + PA^T - PC^T R^{-1}CP + GQG^T. \tag{2.22}$$

In the later applications of this filter it will be seen that the encountered disturbances are not Gaussian. Nevertheless, the Kalman filter is still the optimal linear filter in such cases [49, 47].

To more intuitively understand the role that these covariance matrices play in the state estimate, the Kalman filter can also be interpreted as minimizing the estimation error in the form of a quadratic cost function [48]:

$$J := \int_{-\infty}^{\infty} (\hat{y}(t) - y(t))^T Q(\hat{y}(t) - y(t)) + h^T(t)Rh(t)dt. \tag{2.23}$$

If the eigenvalues of $R$ dominate those of $Q$, it means that we assume more uncertainty is associated with the sensor measurements and thus the optimal filter will not track the

erroneous measurements as rapidly; alternatively if the eigenvalues of $Q$ dominate those of $R$, it means that we assume more uncertainty is associated with the plant disturbances and the measurements are more reliable, and so the estimated state will more rapidly track the measured states. The estimator performance therefore is dependent on *a priori* data regarding the status of the system and available measurements.

State estimators can be used for control in the sense that feedback control, where $u = f(x)$, can be carried out using the state estimate $u = f(\hat{x})$. This is the basic principle in the classic linear-quadratic-Gaussian control problem, in which the linear-quadratic-regulator (LQR) controller is applied to the state reconstructed by the linear-quadratic-estimator (LQE). However this is not a typical application in power systems or microgrids, despite the prevalence of state estimation in such systems.

Instead, state estimation tends to be used more for static state applications, where it is used mostly at the transmission level. In this context, the state estimator can be interpreted as a data processing technique for converting redundant data, such as meter readings, into an improved approximation of the state [51]; note that here 'static' means that the time-varying dynamics of the system are not estimated. This is especially useful for centralized grid operators, where these techniques are applied for better energy management, pricing, and trading [52, 53]. In these applications, measurements are taken at regular intervals, and then a state estimate is constructed to better understand grid conditions and potential network congestion. The obvious limitation is that these methods are limited to updates every few minutes, which limits the potential of real-time estimation [54].

While less popular, dynamic state estimators have been applied for forecasting in smart grids, so that grid operators can make better decisions regarding economic dispatch and

security assessments [55]. In [55], Kalman filters and linear exponential smoothing techniques were applied to better update and forecast the network estimate. In this centralized process, data management poses a challenge for real-time computation; the volume of incoming data can make it computationally infeasible for dynamic estimation which may need to be done rapidly. To address this concern, authors in [56] presented methods to more efficiently process this data, to make the centralized estimation problem more feasible.

However in these cases the estimators are centralized in that they assume grid-wide data is sent to a single hub [54, 57]. As a result, these methods are not applicable for control at the distribution level, and are thus unsuited for decentralized control in microgrids; especially with the growing number of DERs, real-time communication between a DER and a centralized grid operator is heavily limited. The concept of a 'smart' grid includes the idea of increased communication, and so some authors have presented ideas which include 5G data transmission which can in turn facilitate real-time centralized estimation [58]. These communication protocols can be costly, and so while they present a useful hypothetical, they do not answer the question of how decentralized estimation can be performed using the hardware presently installed.

Real-time control is not yet a typical application for microgrid state estimation as it would need to be both dynamic and decentralized. Nevertheless, the growth of smart grids is coupled with an exponential increase in measurable data [52] that in turn disrupts long-standing beliefs about the role of state estimation in these networks. With the challenges that smart grids and distributed energy pose to traditional control architectures, we propose that it is worth reconsidering traditional stances towards both decentralized estimation and control in microgrids.

# Chapter 3

# H-Infinity Voltage and Frequency Control in Microgrids

The earlier literature review gave an overview of H-infinity control research particularly as it applied to microgrids. This section describes the past, current, and proposed work related to H-infinity control in microgrids, as well as the contribution of each[1].

As described in the earlier background, droop control is simple and easy, but limited. While droop controlled inverters ensure steady-state stability, their transient performance is generally not optimized. This is particularly relevant as inverter dynamics are fast, and thus the interconnections between droop-controlled inverters can often result in undesirable harmonics and ringing behavior.

The goal of this work was to design a controller for a distributed generator that would result in superior or optimized system performance. We have explored multiple extensions and iterations of this idea.

[1]Results in this section have been published in the following [59], [60]:
(1) M. Chu Cheong, P. Du, and D. Chen, "Decentralized H-Infinity Control to Mitigate Renewable Intermittency," in *ASME Dynamic Systems and Control Conference*, (Minneapolis, MN), Oct. 2016.
(2) M. Chu Cheong, H. Qian, J. Conger, D. Chen, and P. Du, "Distributed H-Infinity Frequency Control for Inverter Connected Microgrids," in *ASME Dynamic Systems and Control Conference*, (Tyson's Corner, Virginia, USA), ASME, Oct. 2017.
In (1), M. Chu Cheong was responsible for the entirety of the work. In (2), M. Chu Cheong was responsible for the majority of the work, with modeling assistance from H. Qian and J. Conger. P. Du and D. Chen provided advisory input in both cases.

The first results of our research addressed the voltage control problem. Following the example of [26, 25, 61], the frequency was assumed to be held constant at the desired setpoint, and controlled by a separate controller. The resulting controllers then focused on minimizing voltage deviations at local voltage buses, as shown in [FIGURE]. The robustness of this controller was explored relative to parameter and structural perturbations; the controller performance highlighted its performance despite intermittent wind turbine power injections.

A later investigation modeled and controlled both frequency and voltage in a microgrid using this decentralized H-infinity control method. In this case, the frequency of the microgrid was modeled by considering the dynamics of a phase-locked-loop (PLL) coupled to each inverter. This PLL is a controller which keeps all inverters in phase, to allow for coordinated power injection in the network. This expanded upon the previous iteration by considering the frequency dynamics, which is a crucial component of power quality analysis.

The drawback of this approach is that the frequency model was limited. In this case, frequency did not vary in response to real power injections as is typical in power systems, but instead varied in response to a PI-gain relative to error in the q-phase of the bus voltage. In that scenario, all inverters could be kept in phase with each other provided that they followed this control rule as well. However, this limited the applicability of the control method to general power systems and microgrids; if the controlled inverter cannot be kept in phase with the remainder of the system, the control law cannot be used.

This motivates my current research into the area, which models the frequency in the grid in a way that adheres to conventional standards.

## 3.1 Voltage Control Using Decentralized H-Infinity Methods in a Microgrid

For this research, the question of decentralized voltage control in a microgrid was considered. Both voltage and frequency are important aspects of power quality, and in this case the frequency was assumed to be independently controlled following [61]. Frequency was assumed to be set by a local oscillator; [61] assumed that the synchronization of these signals would be done via GPS coordination.

The question of voltage control is significant, yet less challenging than controlling both frequency and voltage. Unlike frequency, inverters do not have to be synchronized to the same voltage; signals operating at different frequencies in a power system can lead to network instability and failures as the superposed signals are irregular and inconsistent. The goal of this work was to identify how effectively H-infinity and H-2 control methods could be implemented in a microgrid, and whether the subsystems were too closely coupled for these decentralized control methods to be effective. The resulting success of this exploration showed potential for later research into the frequency control aspect of the problem.

### 3.1.1 Model

For this analysis, the microgrid was interpreted as an interconnection of $n$ subsystems. Each subsystem was comprised of an inverter-interfaced distributed generator treated as a voltage source inverter (VSI), and an $RLC$ load. The network was also modeled; these systems were coupled via distribution lines that connected various subsystems. In this work, we investigated the case for $n = 4$, where subsystem $i$ was connected to subsystem $i + 1$. These parameters were selected to make it possible to explore the dynamics due to the

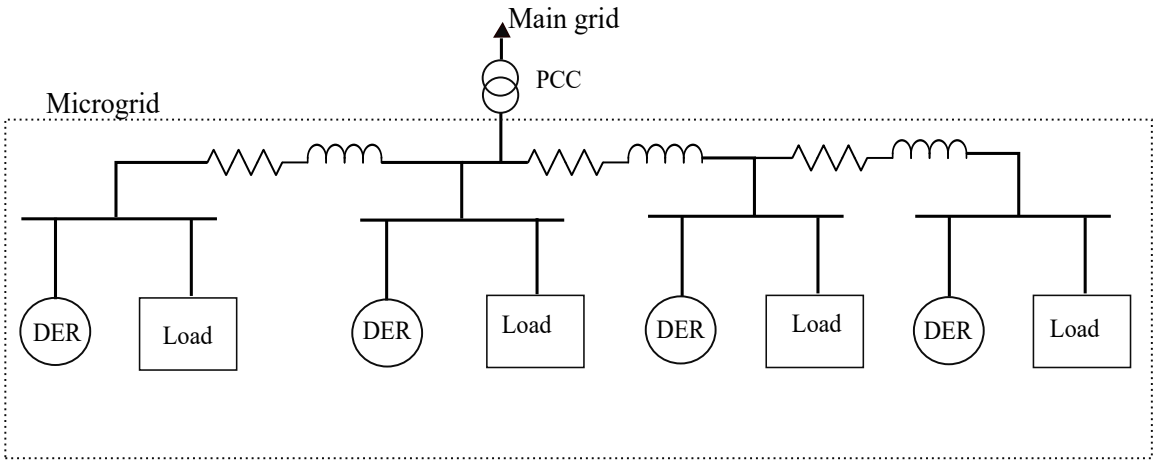


Figure 3.1: A representative microgrid: a series of interconnected DERs and loads, joined to the main power grid at its point of common connection (PCC).

couplings and interconnections between these controlled inverters, while also facilitating a clear understanding of the behavior of each subsystem. This overall structure can be seen in figure 3.1, with a more detailed illustration of each subsystem in figure 3.2.

The state-space was modeled in the dq0 reference frame; as all inverters were considered to be in phase, at the same reference frequency $\omega$, there was no need for additional reference frame transformations. For this structure, the state variables associated with each subsystem were the bus voltages, $v_{b,dq}$, the line currents connecting the VSI to the bus voltage, $I_{f,dq}$, and the currents associated with the static RLC load, $I_{l,dq}$. In addition to these subsystem variables, network dynamics were also modeled; the currents along the lines connecting voltage buses, $I_{t,dq}$, were modeled as part of the state. To avoid cumbersome indexing, the line current connecting subsystem $i$ to subsystem $i+1$ was considered to be $I_{ti,dq}$.

The dynamic load current, $I_{w,dq}$, was treated as a disturbance variable. The inclusion

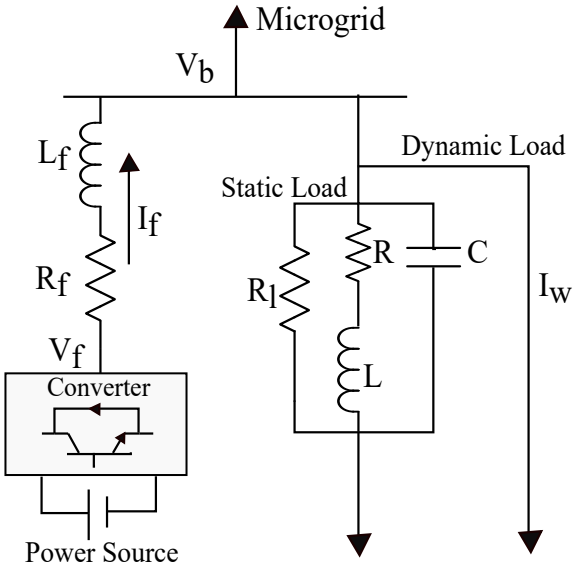


Figure 3.2: The details of a representative subsystem connected to the remainder of the network via distribution lines.

of this disturbance variable made it possible to simulate the system's performance in response to time-varying loads.

The control inputs to this system were the voltages associated with the VSI, $V_{f,dq}$. This represented a controllable power injection into the system; the goal was then to see if the dynamic performance of the system could be effectively controlled by decentralized actuation of these voltages.

As a representative example for this microgrid model, consider some arbitrary subsystem in the microgrid, subsystem $j$. In this scenario, the network topology had been chosen such that subsystem $j$ was connected to subsystems $j-1$ and $j+1$. These dynamics can

be modeled as:

$$\begin{aligned}
\dot{V}_{bj,d} =& \frac{1}{C_j}(I_{fj,d} - I_{lj,d} + I_{t(j-1),d} - I_{tj,d} - I_{wj,d} - \frac{V_{j,d}}{R_j}) + \omega v_{j,q} \\
\dot{V}_{bj,q} =& \frac{1}{C_j}(I_{fj,q} - I_{lj,q} + I_{t(j-1),q} - I_{tj,q} - I_{wj,q} - \frac{V_{j,q}}{R_j}) - \omega V_{j,d} \\
\dot{I}_{fj,d} =& \frac{1}{L_{fj}}(V_{fj,d} - R_{fj} I_{fj,d} - V_{bj,d}) + \omega I_{fj,q} \\
\dot{I}_{fj,q} =& \frac{1}{L_{fj}}(V_{fj,q} - R_{fj} I_{fj,q} - V_{bj,q}) - \omega I_{fj,d} \\
\dot{I}_{Lj,d} =& \frac{1}{L}(V_{bj,d} - R_{lj} I_{lj,d}) + \omega i_{Lj,q} \\
\dot{I}_{Lj,q} =& \frac{1}{L}(V_{bj,q} - R_{lj} I_{lj,q}) - \omega i_{Lj,d} \\
\dot{I}_{tj,d} =& \frac{1}{L_{tj}}(V_{bj,d} - R_{tj} I_{tj,d}) - V_{b(j+1),d} + \omega I_{tj,q} \\
\dot{I}_{tj,q} =& \frac{1}{L_{tj}}(V_{bj,q} - R_{tj} I_{tj,q}) - V_{b(j+1),q} + \omega I_{tj,d}.
\end{aligned} \tag{3.1}$$

These parameters are given in the per-unit basis in table 3.1, and are consistent with microgrid parameters used in [61, 11]. As described earlier, the line connecting subsystems $j$ and $j+1$ is associated with parameters $R_{t,j}$ and $X_{t,j}$.

Table 3.1: Load, line parameters for microgrid, given in p.u.

| | Node 1 | Node 2 | Node 3 | Node 4 |
|---|---|---|---|---|
| $R_j$ | 2.94 | 3.15 | 3.36 | 2.94 |
| $X_{L,j}$ | 0.35 | 0.32 | 0.38 | 0.35 |
| $X_{C,j}$ | 0.37 | 0.34 | 0.41 | 0.37 |
| $R_{l,j}$ | 0.02 | 0.02 | 0.02 | 0.02 |
| $R_{t,j}$ | .015 | .029 | .029 | |
| $X_{t,j}$ | .013 | .026 | .026 | |

Individual subsystems were coupled via $I_{t,dq}$. The overall system dynamics can be

expressed as

$$\dot{x} = Ax + B_u u + B_w w, \tag{3.2}$$

with $x$ representing the various state variables, $u$ representing the designated control inputs, and $w$ representing the system disturbances. In this case, the coupling of the system, specifically between the bus voltages and distribution line currents, implied that the state-matrix $A$ had the following general structure:

$$A = \begin{bmatrix}
* & * & * & & & & & & & & & \\
* & * & * & & & & & & & & & \\
* & * & * & * & & & & & & & & \\
 & & * & * & * & * & & & & & & \\
 & & & * & * & * & & & & & & \\
 & & & * & * & * & * & & & & & \\
 & & & & & * & * & * & * & & & \\
 & & & & & & * & * & * & & & \\
 & & & & & & * & * & * & * & & \\
 & & & & & & & & * & * & * & * \\
 & & & & & & & & & * & * & * \\
 & & & & & & & & & * & * & *
\end{bmatrix}. \tag{3.3}$$

While this is not precisely block-diagonal, it can be seen that individual subsystems are coupled to the remainder of the system insofar as they are affected by adjacent subsystems. This suggested that decentralized multivariable control methods could be well suited for this system [14].

### 3.1.2 Control Methodology

The intention of this research was to identify not only how well H-2 and H-infinity methods could be implemented in microgrids, but to what extent the decentralization of these

controllers would reasonably perform. The control methods that will be outlined provide a quantifiable degree of optimality which allow them to be assessed for practical applicability.

**H-Infinity Norm**

In the context of H-2 and H-Infinity control, 'optimal' has a strict definition. Consider the state-space system that was previously described, now augmented with a set of measured variables, $z$:

$$\begin{aligned} \dot{x} &= Ax + B_u u + B_w w \\ z &= C_z x + D_{uz} u. \end{aligned} \tag{3.4}$$

Here $z$ was the controlled output- the set of variables that we wished to minimize. In the context of this application, $z$ could be some combination of currents and voltages that should be kept small. $\mathcal{H}_\infty$ optimal controllers seek to stabilize the system dynamics while minimizing the $\mathcal{H}_\infty$ norm of $T_{wz}$, the transfer function from the exogenous input $w$ to the controlled output $z$ [62].

The $H_\infty$ norm is conveniently described in terms of singular values,

$$\|G\|_\infty = \sup_\omega \sigma \left\{ G(i\omega) \right\}. \tag{3.5}$$

This norm represents a measure of 'energy' of the response. $\mathcal{H}_\infty$ optimal controllers seek to minimize the effects of the 'worst-case' disturbance.

**Integral Control for Voltage Tracking**

For this application, the goal was to minimize voltage tracking error and control effort. To implement reference tracking, integral states were added:

$$\dot{e} = y_r - r, \tag{3.6}$$

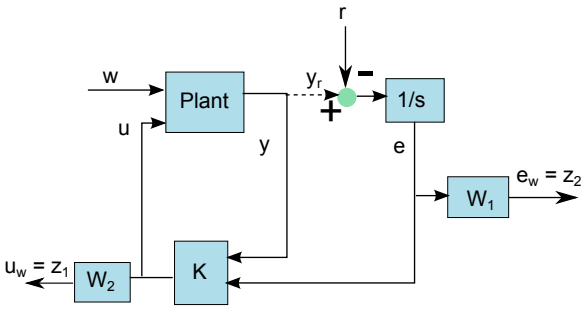


Figure 3.3: Block diagram illustrating the output and feedback interconnections of the system

where $y_r$ was the quantity that was designed to track the reference value, $r$; if the controlled system reaches a steady-state, then the tracking error is 0 as $y_r = r$ in that equilibrium. In this project, reference values for $V_{b,d}$ and $V_{b,q}$ were tracked.

The intention of the controller was to minimize tracking error with respect to input disturbances, while also minimizing the control effort expended by the DERs. This cost function was formally incorporated into the system by adjusting the controlled output, $z$. For each node, consider the local $z$ variables:

$$z_j = \begin{bmatrix} W_1 e_j \\ W_2 u_j \end{bmatrix}. \tag{3.7}$$

In this formalization, $W_1$ refers to the weight placed on minimizing the tracking error, and $W_2$ refers to the weight placed on minimizing the control effort.

This general structure for local $z$ measurements can be seen in figure 3.3.

**H-Infinity Controller Synthesis**

A strong goal is to find a controller that stabilizes the system while simultaneously minimizing the $\mathcal{H}_\infty$ norm of the closed-loop system, $T_{wz}$. For numerical tractability, instead of explicitly minimizing the norm, it is more common to address the problem of suboptimal

control: for a given $\gamma$, the goal is to ensure closed-loop stability while ensuring that the norm of the closed-loop system is bounded by $\gamma$.

With $y$ representing measurement variables available for control, we formally sought a controller of the form

$$u = Ky = KC_y x, \tag{3.8}$$

such that that the system was stabilized and the norm of the transfer function from $w$ to $z$ satisfied $\|T_{wz}\|_\infty < \gamma$. Minimizing $\gamma$ then resulted in a controller that was more 'optimal.' It should be noted that this is a supremum and not an explicit minimum for the $\mathcal{H}_\infty$ norm.

To efficiently solve this problem, we can state the problem in a convex form; the problem must be rewritten as the minimization of a convex function over convex sets.

Consider the closed loop system under static output feedback:

$$\begin{aligned} \dot{x} &= A_{cl}x + B_{cl}w \\ z &= C_{cl}x, \end{aligned} \tag{3.9}$$

where

$$\begin{aligned} A_{cl} &= A + B_u K C_y \\ B_{cl} &= B_w \\ C_{cl} &= C_z + D_{uz} K C_y. \end{aligned} \tag{3.10}$$

.

Following [63, 64, 65], the bounded-real-lemma can be manipulated to bound the $\mathcal{H}_\infty$ norm of this closed-loop system. Written as a convex program, this yields

$$\begin{aligned} &\underset{X,Y}{\text{maximize}}\ \eta \\ &\text{subject to } X_q \succ 0,\ X_r \succ 0,\ \eta > 0, \\ &\qquad \begin{bmatrix} \Psi(X,Y) + \eta B_w B_w^T & XC_z^T + Y^T D_{uz}^T \\ C_z X + D_{uz} Y & -I \end{bmatrix} \prec 0. \end{aligned} \tag{3.11}$$

where we define

$$\begin{aligned} X &:= QX_qQ^T + RX_rR^T; \\ Y &:= Y_rR^T; \\ R &:= C_y^+ + QL; \\ \Psi(X,Y) &:= AX + XA^T + B_uY + Y^TB_u^T. \end{aligned} \tag{3.12}$$

Here $Q \in \mathbb{R}^{n\times(n-p)}$ is a matrix whose columns are a basis of $\mathrm{Ker}(C_y)$, $C_y^+$ is the Moore-Penrose pseudoinverse of $C_y$, and $L \in \mathbb{R}^{(n-p)\times p}$ is a constant matrix chosen during the design process. The notation $\succ 0$ and $\prec 0$ are used to signify that the matrices are positive definite and negative definite, respectively.

If a solution exists, with the optimal set $(\tilde{\eta}, \tilde{X}_q, \tilde{X}_r, \tilde{Y}_r)$, then the stabilizing output gain matrix is given as

$$\tilde{K} = \tilde{Y}_r{\tilde{X}_r}^{-1}, \tag{3.13}$$

with an associated $\mathcal{H}_\infty$-norm $\gamma_{\tilde{K}}$ such that

$$\gamma_{\tilde{K},\infty} \leq (\tilde{\eta})^{-2}.$$

**Controller Decentralization**

Decentralized control, a specific case of structured control, refers to the case where each controller only has access to local variables. For the modeled microgrid, this yields the constraint that the input to the $i^{th}$ subsystem, the generator voltage $u_i$, is some linear combination of local state variables, $x_i$:

$$u_i = V_{fi} = K_ix_i. \tag{3.14}$$

For the full system, we can define the control law

$$u = Kx, \tag{3.15}$$

where

$$u = [u_1 \dots u_n]^T \tag{3.16}$$

$$x = [x_1 \dots x_n]^T. \tag{3.17}$$

This necessitates the constraint that $K$ must be block diagonal,

$$\begin{bmatrix} K_1 & 0 & \dots & 0 \\ 0 & K_2 & & \\ \vdots & & \ddots & \\ 0 & & & K_n \end{bmatrix}, \tag{3.18}$$

yielding the corresponding inputs:

$$u = \begin{bmatrix} K_1 x_1 & K_2 x_2 & \dots & K_n x_n \end{bmatrix}^T. \tag{3.19}$$

The structured feedback matrix, $K$, is synthesized by implementing the desired structural constraints on $X_r, Y_r$ [64, 66]. For the case where $K$ is constrained to be block diagonal, this can be achieved with a block diagonal structure in $X_r$ and $Y_r$. In general, any arbitrary structure can be implemented in the convex constraints by enforcing the desired structure in $X_r$ and a block diagonal or diagonal structure in $Y_r$ [66].

### 3.1.3 Results

The proposed decentralized control scheme was able to effectively track a reference voltage despite an abrupt power injection, followed by intermittent power changes. Moreover

the proposed decentralized design resulted in comparable performance to the fully centralized case, demonstrating that the decentralized communication constraint did not significantly limit the H-infinity methods. The controller was shown to be robust to model uncertainty and grid topology changes, demonstrating value for common issues faced by microgrids.

To test the control design, we simulated the system response to an abruptly-connected wind turbine. The turbine was simulated to be operating in its partial-load mode, and so injected a variable amount of power over the course of 100 seconds. The goal was to see how well the controlled system would be able to track the voltage references despite this intermittent power addition.

The wind turbine was abruptly connected to the system at $t = 0.05$. Relative to the total power demand at subsystem 4, this is associated with a step in real power supply of approximately 81%. A reference setpoint of $V_d = 0.6$ kV and $V_q = 0$ kV, corresponding to 1 and 0 in the p.u. basis, is designated. The wind turbine is operating in its partial-load mode, where the output is determined as in [30].

The controlled response is given in figures 3.4 and 3.5, which show the tracked voltage behavior. Figure 3.4 illustrates the steady-state reference tracking at each node, along with the associated control type (centralized or decentralized) at each DER. The response is extended until $t = 100$, to show controller performance relative to changes in wind turbine power, as seen in figure 3.5.

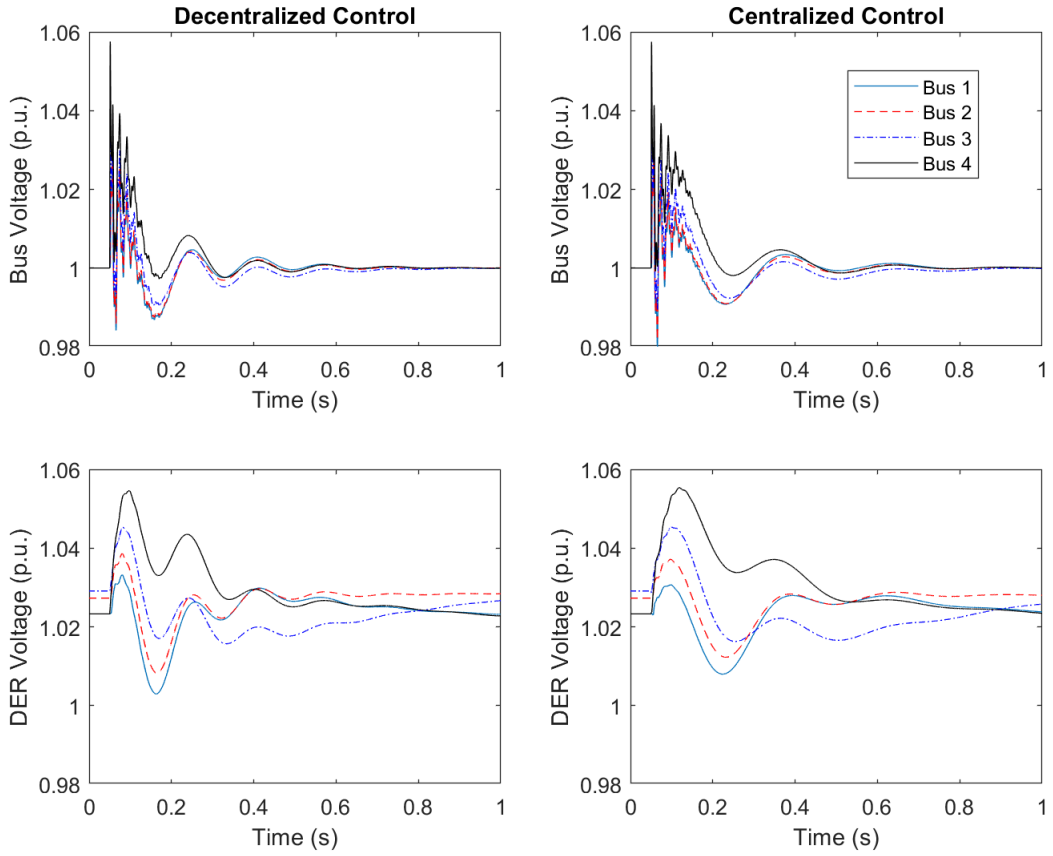


Figure 3.4: Microgrid voltage response to the connected wind turbine.

Table 3.2: $\mathcal{H}_\infty$ norms for the closed-loop system

| | Decentralized | Centralized |
|---|---|---|
| $\|T_{wz}\|_\infty$ | 8.72 | 5.82 |

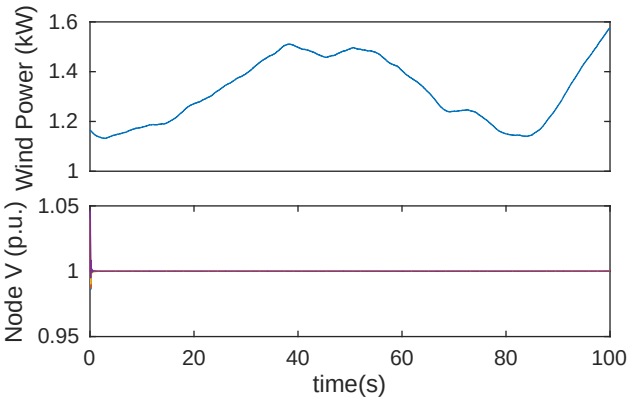


Figure 3.5: Wind turbine power output and normalized reference tracking over a longer timescale.

We observed that decentralization of the control design process resulted in a moderate increase of the measured H-Infinity norm of the overall system response. That said, the microgrid performance did not notably suffer in terms of its physical performance; while the decentralized controllers produced a less damped response than the centralized controllers, in neither scenario did the system demonstrate highly oscillatory or underdamped behavior. The specific norms associated with the decentralized and centralized controllers are shown in table 3.2.

Similarly, it was evident that the timescales at which both controllers were able to respond was much faster than the timescales at which the wind turbine power output changed. While this is nominally a function of the physical limits of the control actuator,

it is important to note that controlled response did not result in significant undesirable harmonics despite the comparatively rapid control action. In this simulated scenario, the most conspicuous system response was a result of the abrupt turbine connection at $t = 0.05$, upon which the controllers essentially respond to a step disturbance. Here both controllers resulted in settling times of less than 1 second, after which they were both able to easily track the reference voltage in spite of the variable power injection from the wind turbine.

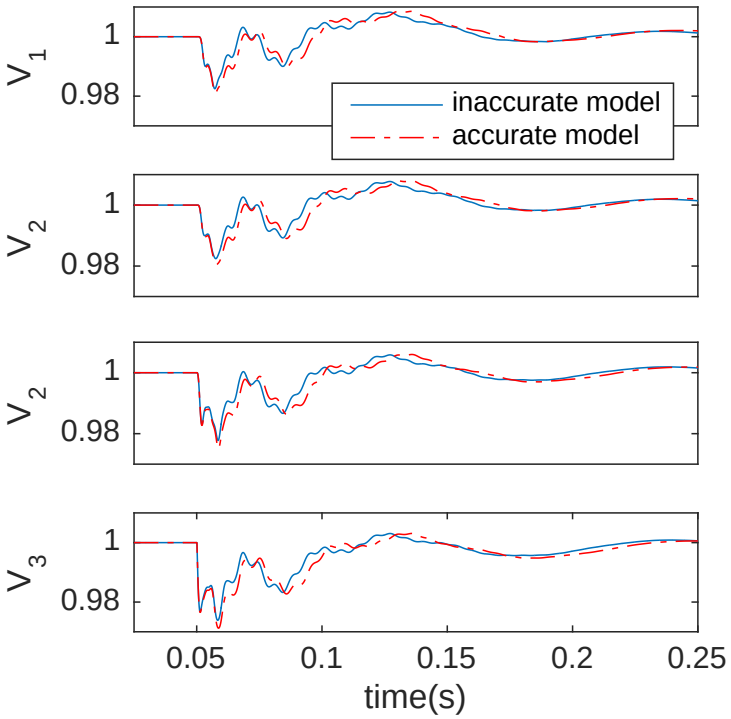


Figure 3.6: Comparing the controlled system response when the controllers are supplied with perturbed model parameters.

To demonstrate robustness, the system was tested against model uncertainty and sudden changes in grid topology. The first case represents the situation where there is a

mismatch between modeled parameters and actual parameters. As this controller design depended upon the full system model, it would be reasonable to assume that an inexact model may result in significant deterioration in controller performance. To examine the controller performance relative to model uncertainty, the controllers were designed based on the presumed model while all the system parameters were set to 120% of their modeled values. The performance of the decentralized H-infinity controllers with respect to this parameter uncertainty is shown in figure 3.6. It can be seen that even when the controller was supplied with inexact model information, the difference in the controlled system response was negligible; the controllers were robust to parameter uncertainty.

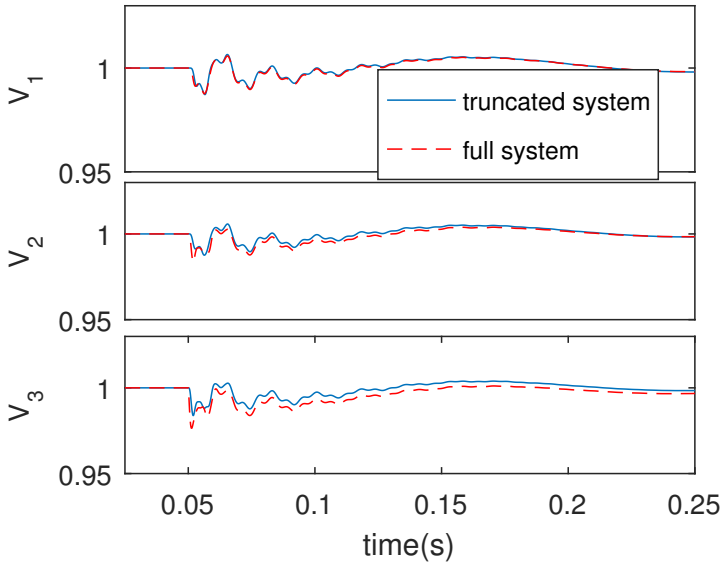


Figure 3.7: Decentralized H-infinity performance when a node is disconnected from the microgrid; compared to performance with all nodes connected.

The second robustness analysis considered a situation to exemplify the modularity of a microgrid. The controllers in this simulation were designed for a microgrid with 4 voltage

buses, with an interconnected structure that is assumed to be known *a priori*. Even though the controllers used only local data, the optimal control design involved the full grid structure. Therefore if a node were to be suddenly disconnected from the microgrid, as might be the case if a power line failed or a generator was taken offline for maintenance, it may be expected that the controller would suffer serious losses in performance. The performance of the decentralized H-infinity controllers with respect to this structural uncertainty is given in figure 3.7, where controllers which were designed for 4 nodes were simulated when only 3 nodes were available. In this case the controlled system was significantly robust to this structured uncertainty; comparing the tracked voltage response, the maximal difference between the perturbed and unperturbed cases was on the order of 0.05%.

### 3.1.4 Discussion

This work provided helpful insights from the mathematical aspect of the control problem. These results provided evidence that decentralized $H_\infty$ control could be effectively applied at the fast timescales required for primary control in microgrids. Moreover, it could be seen that decentralization of these controllers using this method resulted in only small performance losses compared to the centralized case.

Practically, these results showed that this control methodology could mitigate disturbances that may be expected from intermittent renewable generation, at times when this generation is treated as a positive load rather than a controlled source. The robustness of the resulting controller was evident in terms of parameter, model, and topology disturbances.

## 3.2 Distributed Frequency Control for Inverter-Connected Microgrids

In this extension, the question of decentralized frequency control was considered in microgrids. The previous section addressed voltage control, assuming that frequency was handled elsewhere. As discussed, this investigation had its merits, but left significant questions unanswered.

Frequency control in microgrids is particularly relevant from a power quality perspective. As described earlier, without much inertia, microgrids are conspicuously vulnerable to sharp frequency deviations.

Meanwhile from the control perspective, the frequency control problem presents unique challenges. Each power source in an AC microgrid provides power at some voltage level, with some frequency. Unlike voltage, these frequencies must be synchronized; if the power is asynchronous, the resulting superposition of signals results in grid failures. This resulted in a decentralized control problem where the decentralized control actuators must coordinate on the same objective.

Decentralized H-infinity controllers were designed and implemented to explore their effectiveness for this problem.

### 3.2.1 Model

The model for this work is largely similar to that of the previous section. However, this extension modeled frequency dynamics, and thus frequency was its own state variable.

It is important to note that while we have the concept of a single network frequency,

there is not a single 'frequency' variable in most power system networks. Each power source in a network provides power at some frequency; the coupling and control between these power sources results in frequency synchronism.

As each generator or inverter operates at its own frequency at its own phase, this presents challenges for the d-q transformation. Recall that the d-q reference frame transformation essentially shifts a stationary reference frame to become a rotating reference frame; if there are multiple frequencies and phases in play, then this reference frame transformation needs to be adjusted accordingly [11].

As each inverter has its own frequency and phase, each inverter is associated with its own local reference frame. A global or common reference frame is then designated, to allow for interconnections between these local reference frames. To denote the difference between a variable in a local reference frame compared to its equivalent in the common reference frame, we adopt the notation of $x_d$ to signify a local instance, and $x_D$ to signify its global translation.

For a given inverter, the local dynamics express the behavior of the subsystem, i.e. the network bus voltage $V_b$, the inverter output current $I_f$, the load currents $I_l$ and $I_w$, and the inverter frequency, $\omega$. Note that the only difference compared to the previous section is that now $\omega$ is modeled as a state variable.

To model these frequency dynamics, a phase-locked-loop (PLL) was implemented to set the frequency for each inverter. This PLL is used to keep the local frequency in phase with the global frequency. In this case, $V_{b,q}$ was used for this comparison. $V_{b,q}$ was controlled to be kept at 0; if it was greater than 0, the inverter was considered to be lagging the grid,

and if it was less than 0 the inverter was considered to be ahead of the grid. The function of the PLL was therefore to keep the inverter in phase by measuring $V_{b,q}$. A PI controller was used for this purpose.

These local dynamics are presented here:

$$\begin{aligned}
\dot{V}_{bj,d} =& \frac{1}{C_j}(I_{fj,d} - I_{lj,d} + I_{t(j-1),d} - I_{tj,d} - I_{wj,d} - \frac{V_{j,d}}{R_j}) + \omega v_{j,q} \\
\dot{V}_{bj,q} =& \frac{1}{C_j}(I_{fj,q} - I_{lj,q} + I_{t(j-1),q} - I_{tj,q} - I_{wj,q} - \frac{V_{j,q}}{R_j}) - \omega V_{j,d} \\
\dot{I}_{fj,d} =& \frac{1}{L_{fj}}(V_{fj,d} - R_{fj} I_{fj,d} - V_{bj,d}) + \omega I_{fj,q} \\
\dot{I}_{fj,q} =& \frac{1}{L_{fj}}(V_{fj,q} - R_{fj} I_{fj,q} - V_{bj,q}) - \omega I_{fj,d} \\
\dot{I}_{Lj,d} =& \frac{1}{L}(V_{bj,d} - R_{lj} I_{lj,d}) + \omega i_{Lj,q} \\
\dot{I}_{Lj,q} =& \frac{1}{L}(V_{bj,q} - R_{lj} I_{lj,q}) - \omega i_{Lj,d} \\
\dot{\delta}_j =& \omega_j \\
\dot{\omega}_j =& K_{PLL} \frac{dV_{bj,q}}{dt} + \frac{K_{PLL}}{T_{PLL}} V_{bj,q}.
\end{aligned} \tag{3.20}$$

$K_{PLL}$ and $T_{PLL}$ are PI controller gains for the phase locked loop.

In addition to local subsystem dynamics, network dynamics due to line interconnections also needed to be modeled. To keep this formalism as simple as possible, we designated these line dynamics to be in the common reference frame; the alternative would be to model these line dynamics in the reference frame of multiple inverters, but this would not change the accuracy of the model and would needlessly complicate the representation. These network

dynamics were modeled as:

$$\begin{aligned}\dot{I}_{tj,D} =& \frac{1}{L_{tj}}(V_{bj,D} - R_{tj}I_{tj,D}) - V_{b(j+1),D} + \omega I_{tj,Q} \\ \dot{I}_{tj,Q} =& \frac{1}{L_{tj}}(V_{bj,Q} - R_{tj}I_{tj,Q}) - V_{b(j+1),Q} + \omega I_{tj,D}.\end{aligned} \tag{3.21}$$

### 3.2.2 Control Methodology

Our objective was to track voltage and frequency to desired setpoints. This involves augmenting the system with corresponding error states in the form:

$$\dot{e} = y_r - r, \tag{3.22}$$

where $y_r$ is the variable that should track the reference $r$. For the case of the microgrid, various error states are included in order to track the voltage of each bus, $V_{bi}$, as well as the frequency of the common reference frame, $\omega_1$. As these frequencies are all linked, they cannot be separately tracked.

In the stabilized case, we arrive at a steady-state where the error will be driven to 0. This implies that if if we can control the augmented system dynamics, then the reference value will be tracked in the steady state. The objective is to design a controller such that the tracking error is minimized with respect to input disturbances.

The robustness and performance of the controlled system are dependent on the design of the state variable, $z$. Unlike the variables $x$ and $y$, which were physically constrained by the system model and available measurements, the controlled output $z$ was chosen to best suit design requirements. For this problem, the objective was to minimize errors in both frequency and voltage, which would result from load fluctuations or grid disturbances.

To this end, we designated z to be a linear combination of the integral states introduced for error tracking, $e_i$, as well as the control inputs, $u_i$. The resulting controller minimized the effect of power disturbances on system deviation and inverter effort. This was achieved in a straightforward way by choosing:

$$\begin{aligned} z_i &= \alpha_i e_i, \\ z_j &= \beta_j V_{f,j}, \end{aligned} \tag{3.23}$$

for $i = 1, \ldots, n_b + 1$ and $j = 1, \ldots, 2n_g$, where $n_b$ and $n_g$ denote the number of voltage buses and generators in the system, respectively. Note that the common frequency for the microgrid is controlled in addition to the $d$-phase bus voltages, as well as both the $d$ and $q$ phases of the inverter output voltage. Here $\alpha$ and $\beta$ can be tuned to meet desired performance features; increasing $\alpha_i$ will bias the controller towards minimizing the system error in voltage or frequency, while increasing $\beta_i$ will bias towards slower inverter responses.

For this scenario, $\alpha_i = 1$ and $\beta_j = 0.01$ for all $i, j$. These choices produced an acceptable level of performance, but specific features could be favored by increasing the associated weight.

The H-infinity control synthesis follows from the previous section. As before, this problem was a structured control problem, where the goal was to design the controllers such that they operate using only local state feedback. This represents the real constraint that distributed power sources generally do not communicate with each other, and must rely only on local measurements.

However unlike the voltage control problem, this research also sought to control frequency. Due to the action of the PLL, the inverters are kept in phase by controlling the

q-phase of the bus voltage, $V_{b,q}$ to its reference point. This reduces or constrains the voltage control problem, as only $V_{b,d}$ can be controlled by inverter actuation.

The frequency control problem is similarly affected by the PLL, which couples all inverter frequencies. Despite this coupling, the individual frequency variables associated with each inverter were included in the cost function. Even though these frequencies were all synchronized by the PLL, damping in the system means that individual frequencies are unequally affected by control actuation. This was done to ensure effective and robust control throughout the microgrid, and avoid a situation where individual frequency variables demonstrated poor transient performance.

### 3.2.3 Results

This research showed the extent to which inverter-connected power sources in a microgrid could be controlled via decentralized H-infinity control techniques. Separate generators operating in parallel were successfully controlled to operate synchronously despite grid disturbances. The controller was demonstrated to be robust to model/parameter uncertainty.

To test the controller, the same microgrid testbed was used as in the previous section; a 4-node microgrid whose parameters are given in 3.1. The magnitudes of these parameters were consistent with a low-voltage power system. Each DER had a voltage rating of 0.6 kV, and power ratings of 1.6 MW.

The controllers were tested in response to multiple step load changes. The magnitude of the disturbances were kept constant, corresponding to an abrupt 301.7 kW change. This value was chosen to represent approximately 50% of the total real power supplied by node 1 at its initial steady-state. A reference setpoint of $V_d = 600$ V and $V_q = 0$ kV, corresponding

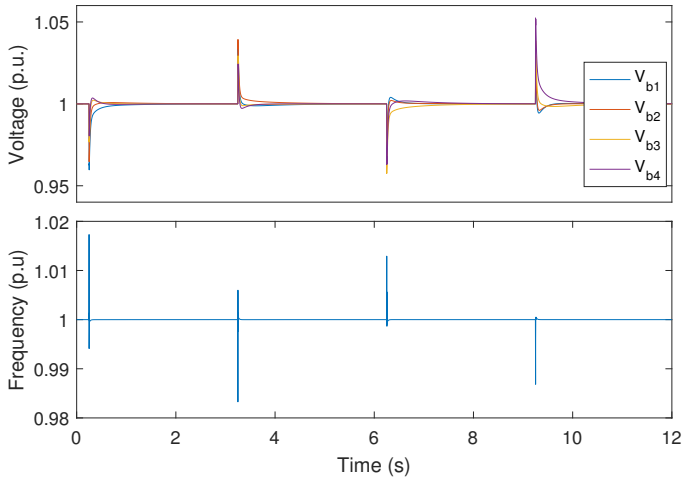


Figure 3.8: Controlled voltage and frequency responses to multiple load step changes.

to 1 and 0 in the p.u. basis, was designated; the goal of the controller was to track these values.

The first disturbance was a load increase at subsystem 1, at time $t = 0.25$; the second was a load decrease at subsystem 2, at time $t = 3.25$; the third was a load increase at subsystem 3, at time $t = 6.25$; the fourth and final disturbance was a load decrease at subsystem 4, at time $t = 9.25$.

In terms of reference following, the objective was to control each bus voltage to $V_{b,d} = 0.6$ kV, and $V_{b,q} = 0$. Frequency was controlled to 60 Hz as is the standard in North America, and all generators were controlled to be in phase with each other.

The controlled results can be seen in figures 3.8 and 3.9. In figure 3.8, voltage and frequency responses are shown on the same time axes in order to illustrate the contrast

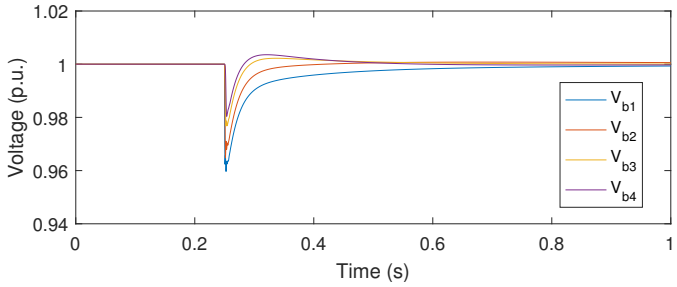


(a) Bus voltages in response to an abrupt load increase at subsystem 1.

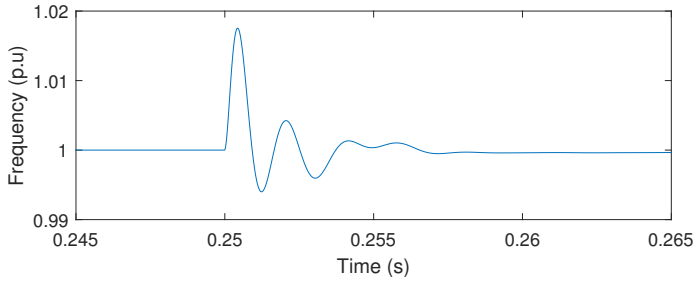


(b) Transient frequency behavior in response to an abrupt load increase at subsystem 1

Figure 3.9: Controlled voltage and frequency in response to the disturbance at node 1. Time axes have been appropriately scaled in order to illustrate transient dynamics.

between the relevant timescales. To better illustrate the transient behavior of voltage and frequency profiles, figure 3.9 shows these results at different timescales.

It was evident that the frequency dynamics in the microgrid are much faster than those dynamics responsible for the controlled voltage responses. This is expected for an inverter based system; without synchronous generators, the system lacked sufficient inertia to dampen the effects that external disturbances can have on grid frequency.

Nevertheless we see that despite this lack of inertia, the rapid response of the system did not result in excessive harmonics. After an approximate 4% change in voltage due to the abrupt disturbance, voltages are restored to their prescribed values in less than 1

second. Frequency is a much more sensitive value, but the controlled profile shows that the disturbance does not cause more than a 2% variation from the nominal value, with restoration within 0.01 seconds. This rapid response was due to the fast characteristics of the modeled inverter; slower dynamics will be present with more inertial generators, but this inertialess case presented a challenging scenario for frequency control.

To illustrate the robustness of the controller to parameter uncertainty, the system was controlled with two separate controllers in figure 3.10. In the 'unperturbed' case, the controller was designed with exact and correct knowledge of the model parameters, while in the 'perturbed' case, the controller was designed for a model whose parameters had been uniformly increased by 20%. These controllers were then used to control the same 'unperturbed' model in response to the aforementioned load changes. As can be seen, the overall performance was largely unchanged but there were some differences, as the perturbed controller was less optimized for disturbance attenuation. The initial step response was of slightly higher magnitude with the perturbed controller, which was especially notable for the voltage; similarly, the ringing is more pronounced as the frequency is regulated to its settling point.

A concern for actual implementation is the robustness of the controller; a controller may perform well in a situation when all parameters are precisely known and the model is correct, but a perfectly accurate model is often a luxury. Here we see that the proposed method was robust to parameter uncertainty by considering the performance of a controller designed for a moderately distinct system. Figure 3.10 illustrates that even when optimized for a model whose parameters differ by 20% from those of the actual system, the controller performed nearly as well as it would if all parameters were precisely known. The slight

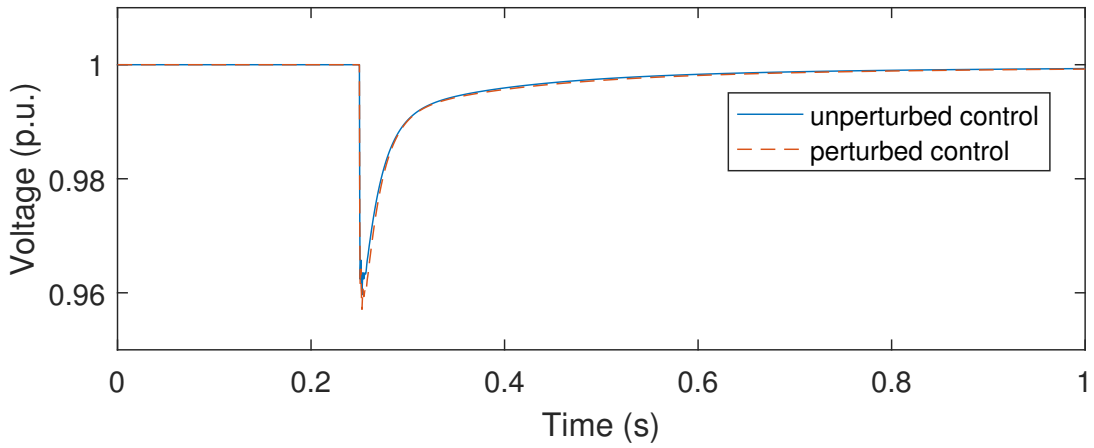


(a) Controlled voltage comparison for perturbed controller

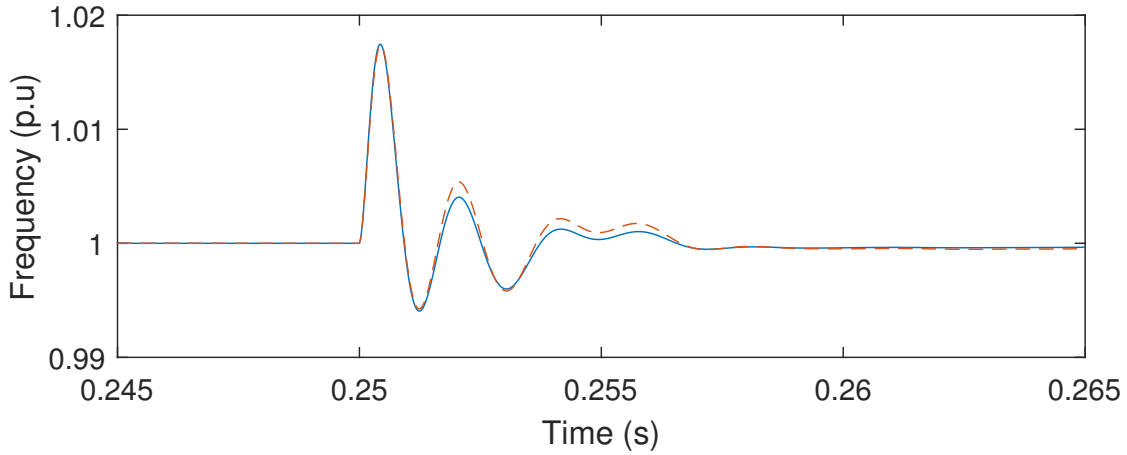


(b) Controlled frequency comparison for perturbed controller

Figure 3.10: Controlled voltage and frequency in response to the disturbance at node 1. Comparison shows that performance is robust to parameter selection.

performance deviation is to be expected, with longer ringing and greater overshoot in the disturbance response, because the disturbance rejection is not optimized for the system. However considering the overall similarity of the responses in figure 3.10, the robustness of this control design was evident.

### 3.2.4 Discussion

In this extension, the question of decentralized frequency control was considered in microgrids. The results of this research showed that both frequency and voltage could be robustly controlled with these decentralized methods. Moreover, the controllers showed robust disturbance rejection despite intermittent renewable power injection; the controlled microgrid was simulated with a wind turbine operating in its maximum power point tracking mode in variable wind speed conditions. The presented controllers were able to effectively reject the intermittency from the turbine and track their reference setpoints.

Notably, the decentralized methods were effective despite the fact that each inverter was independently setting its own frequency. Without appropriate control, this scenario may result in asynchronous operation, where individual inverters operate out of phase with each other. In this case, the PLL associated with each inverter kept them in phase with each other, and the H-infinity controllers minimized the ensuing frequency disturbances.

This demonstrated that this methodology had potential applications for realistic microgrid conditions, which would typically be subject to renewable intermittency.

# Chapter 4

# The Role of Microgrid Topology for Decentralized Control

## 4.1 Overview

In this section we present an analysis of the role of controller and grid topology in achieving decentralized improvements for microgrid performance. Specifically, we explore the role played by the location of microgrid controllers relative to both grid disturbances and grid topology. The previous chapter demonstrated how decentralized methods could improve power quality when applied to all connected sources. We now demonstrate how controlled power injection from even a single source can be tailored to improve grid-wide performance [1].

We present a form of decentralized control in this chapter. In a network of droop-controlled inverters, individual inverters are instead selected to be alternatively controlled; instead of varying frequency and voltage proportionally to active and reactive power loads, a linear controller for voltage is designed for proportional state feedback while the frequency tracks that of the grid average. In this way, power is injected into the grid with the intention

[1] Results in this section have been accepted for publication in:
M. Chu Cheong, P. Du, and D. Chen, "Understanding the Role of Microgrid Topology for Decentralized Model-Based Control," in *ASME Dynamic Systems and Control Conference*, (Park City, UT), Oct. 2019.
M. Chu Cheong was responsible for the entirety of this work, while P. Du and D. Chen provided advisory input.

of minimizing undesirable transient behavior. Steady-state power sharing is maintained by controller tuning.

The following results show that the network topology can have a significant effect on transient performance deterioration. Notably, the presence of a lower rated power source can negatively impact the stability of a microgrid; if even a single such weaker source is 'near' or adjacent to a grid disturbance, then the microgrid may experience severe harmonic disturbances. In addition, if these weaker sources are controlled with a decentralized optimal controller, rather than a typical droop mechanism, then the overall microgrid performance can be significantly improved. We show that the most effective disturbance rejection is observed with controllers that are as close as possible to the disturbance. Additionally, we show that proximity alone is not the deciding factor in controller effectiveness; controllers that are connected to multiple nodes show less transient improvement than those which are connected to only a single node.

That said, the goal of this section is to focus on the role of grid topology and controller location as it affects grid performance. The proposed controller, while it offers benefits, may present challenges with respect to robustness and modularity. The concepts developed in this section, as well as the drawbacks of this controller, are used to motivate later sections where an improved model-based controller is developed for microgrid applications.

## 4.2 Model

We consider an inverter-connected microgrid in which the majority are synchronized via a P-V droop, while some are controlled independently. These can be classified as either *grid-supporting* or *grid-feeding* inverters; the distinction is relevant to the ensuing discussion.

The following descriptions refer to system dynamics in the *dq0* reference frame, as described in [12] due to the convenience when working with power system modeling and control.

Grid-supporting inverters are controlled to mimic the behavior of synchronous generators; to this end they inject power and contribute to the frequency/voltage regulation capabilities of the grid [12]. These inverters are equipped with a droop mechanism, where the output frequency and voltages are linearly related to the active and reactive power outputs, $P$ and $Q$:

$$\begin{aligned} \omega &:= \omega_0 - m_p(P - P_0) \\ V_d &:= V_{d0} - n_q(Q - Q_0) \\ V_q &:= 0, \end{aligned} \tag{4.1}$$

where $m_p$ and $n_q$ are droop-gains that vary depending on the rating of the inverter-connected power source. Droop control results in steady-state power sharing proportional to the designated droop gain; this is analogous to the behavior and power-sharing associated with synchronous generators [5].

Unlike grid-supporting inverters, grid-feeding inverters cannot independently set a variable frequency or voltage in response to changes in power output. Instead, these inverters are designed to mainly deliver power, while the frequency is determined by the interaction of the inverter with the grid. Grid-feeding inverters can operate in parallel with other grid-supporting or grid-feeding units, but cannot stably operate in isolation as they lack the ability to set the voltage magnitude and frequency for the system [12].

In this modeled microgrid, there are $N$ inverters, of which $n_s$ are grid-supporting and $n_f$ are grid-feeding, where $n_f + n_s = N$. The grid-supporting inverters are equipped

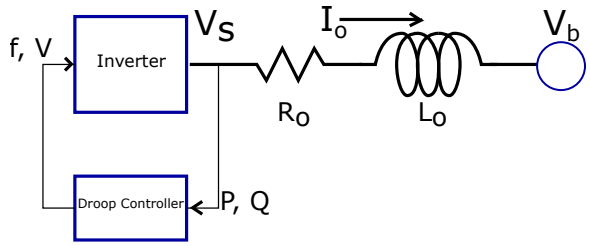


Figure 4.1: Overview of droop-controlled inverter setting the output frequency $f$ and voltage $V_S$ of the power source, connected to a network bus, $V_b$.

with a droop mechanism, and as such they have a prescribed response to variations in load. Meanwhile the grid-feeding inverters are controlled independently; to interact synchronously with the remainder of the power system, the controlled inverters can be set to follow the frequency measured from the microgrid. The hypothesis we propose is that even if frequency is not independently set, intelligent power injection by voltage actuation can result in an improved transient response.

To model this system, we must describe models of inverter-connected power sources as well as that of the interconnecting network. Both (droop-controlled) grid-supporting inverters, as well as grid-feeding inverters, are included in this analysis.

### 4.2.1 Grid-Supporting Inverters

Grid-supporting inverters are equipped with a droop mechanism,in which the output frequency and voltages are linearly related to the active and reactive power outputs, $P$ and $Q$ as shown in figure 4.1:

$$\begin{aligned} \omega &:= \omega_0 - m_p(P - P_0) \\ V_d &:= V_{d0} - n_q(Q - Q_0) \\ V_q &:= 0, \end{aligned} \tag{4.2}$$

In practice, droop controllers are commonly equipped with low-pass filters in order to avoid highly oscillatory behavior. These filters can be interpreted as a first-order lag transfer function. Therefore a grid-supporting subsystem can be modeled as:

$$
\begin{aligned}
V_{j,gd} &:= V^0_{j,gd} - n_q(Q - Q^0) \\
V_{j,gq} &:= 0 \\
\omega_j &:= \omega^0_j - m_p(P - P^0) \\
\dot{\delta}_j &= \omega_j \\
\dot{P}_j &= \tau(V_{j,gd}I_{j,od} + V_{j,gq}I_{j,oq} - P_j) \\
\dot{Q}_j &= \tau(V_{j,gq}I_{j,od} - V_{j,gd}I_{j,oq} - Q_j) \\
\dot{I_{oj,d}} &= \frac{1}{L_{oj}}(V_{gj,d} - R_{oj}I_{oj,d} - V_{bj,d}) + \omega I_{oj,q} \\
\dot{I_{oj,q}} &= \frac{1}{L_{oj}}(V_{gj,q} - R_{oj}I_{oj,q} - V_{bj,q}) - \omega I_{oj,d}.
\end{aligned}
\tag{4.3}
$$

We can identify the dynamic state associated with the grid-supporting subsystem as

$$x_{s,j} = [\omega_j, \delta_j, P_j, Q_j, I_{oj,d}, I_{oj,q}]^T, \tag{4.4}$$

where $\omega$ is the frequency of the inverter, $\delta$ is its phase, $P$ and $Q$ are the filtered measurements of active and reactive power respectively, and $I_o$ is the output current from the inverter to the node voltage bus. The nonlinear model can be linearized about the steady-state, $x^0_{s,j}$,

such that the new dynamic variables are designated $\Delta x_{s,j} = x_{s,j} - x^0_{s,j}$, as follows

$$
\begin{aligned}
&\Delta V_{j,gd} := -n_q(\Delta Q) \\
&\Delta V_{j,gq} := 0 \\
&\Delta \omega_j := -m_p(\Delta P) \\
&\Delta \dot{\delta}_j = \Delta \omega_j \\
&\Delta \dot{P}_j = \tau(\Delta V_{j,gd} I^0_{oj,d} + V^0_{j,gd} \Delta I_{oj,d} + \Delta V_{j,gq} I^0_{oj,q} + V^0_{j,gq} \Delta I_{oj,q} - \Delta P_j) \\
&\Delta \dot{Q}_j = \tau(\Delta V_{j,gq} I^0_{oj,d} + V^0_{j,gq} \Delta I_{oj,d} - \Delta V_{j,gd} I^0_{oj,q} - V^0_{j,gd} \Delta I_{oj,q} - \Delta Q_j) \\
&\Delta \dot{I}_{oj,d} = \frac{1}{L_{oj}}(\Delta V_{gj,d} - R_{oj} \Delta I_{oj,d} - \Delta V_{bj,d}) + \omega^0 \Delta I_{oj,q} + \Delta \omega I^0_{oj,q} \\
&\Delta \dot{I}_{oj,q} = \frac{1}{L_{oj}}(V_{gj,q} - R_{oj} I_{oj,q} - V_{bj,q}) - \omega^0 \Delta I_{oj,d} - \Delta \omega I^0_{oj,d}.
\end{aligned}
\tag{4.5}
$$

### 4.2.2 Grid-Feeding Inverters

In this design, the control actuators to the microgrid are grid-feeding inverters. To this end, the voltage of the grid-feeding inverter is controlled freely in order to modulate the amount of power added to the system; the frequency is set to follow the microgrid average frequency. This is distinct from the grid-supporting case where the inverter sets a frequency proportional to its load. The specific control input signal to the inverter is described in the following section.

The dynamics for a grid-feeding subsystem can be described as:

$$
\begin{aligned}
&\omega_j := \omega_{grid} \\
&\dot{I}_{oj,d} = \frac{1}{L_{oj}}(V_{fj,d} - R_{oj} I_{oj,d} - V_{bj,d}) + \omega I_{oj,q} \\
&\dot{I}_{oj,q} = \frac{1}{L_{oj}}(V_{fj,q} - R_{oj} I_{oj,q} - V_{bj,q}) - \omega I_{oj,d},
\end{aligned}
\tag{4.6}
$$

where the controllable variables are $V_{fj,d}, V_{fj,q}$. The grid-feeding inverter cannot independently set a frequency that would allow for parallel operation with the remainder of the grid; as such, the frequency of the grid-feeding inverter is set to track that of the microgrid.

We can identify the dynamic state associated with the grid-feeding subsystem as

$$x_{f,j} = [I_{oj,d}, I_{oj,q}]^T. \tag{4.7}$$

This can be linearized as

$$\begin{aligned} \Delta\omega_j &:= \Delta\omega_{grid} \\ \dot{\Delta I}_{oj,d} &= \frac{1}{L_{oj}}(\Delta V_{fj,d} - R_{oj}\Delta I_{oj,d} - \Delta V_{bj,d}) + \omega^0 \Delta I_{oj,q} + \Delta\omega I^0_{oj,q} \\ \dot{\Delta I}_{oj,q} &= \frac{1}{L_{oj}}(V_{fj,q} - R_{oj} I_{oj,q} - V_{bj,q}) - \omega^0 \Delta I_{oj,d} - \Delta\omega I^0_{oj,d}. \end{aligned} \tag{4.8}$$

The control actuator in this configuration is given by the voltage of the grid feeding DER; this can be adjusted to vary the power provided to the microgrid. We can therefore label

$$u_{f,j} = [V_{fj,d}, V_{fj,q}]^T. \tag{4.9}$$

### 4.2.3 Network

Individual power sources, whether they are grid-feeding or grid-supporting, are connected by individual distribution lines in the microgrid. To model these interconnections, it is necessary to transform distinct *dq0* reference frames. As described earlier, the *dq0* transformation involves a shift from a stationary reference frame to a rotating one, where the *dq0* reference frame at node $j$ rotates at the frequency associated with the local inverter, $\omega_j$. During transient periods, $\omega_j \neq \omega_k$ for $j \neq k$, and so another reference frame transformation

is necessary in order to correctly model the interactions between different subsystems. In other words, the local reference frames must be mapped to a shared reference frame, or vice versa, for a cohesive model [11, 12]. Following [11], this is

These reference frame shifts follow from the derivation of the *dq0* transformation. For two reference frames with angles $\delta_1$ and $\delta_2$, variables can be transformed as

$$x_1 = \begin{bmatrix} \cos(\delta_2 - \delta_1) & -\sin(\delta_2 - \delta_1) \\ \sin(\delta_2 - \delta_1) & \cos(\delta_2 - \delta_1) \end{bmatrix} x_2. \tag{4.10}$$

For small phase differences, this transformation can be linearized as

$$\Delta x_1 = \begin{bmatrix} \cos(\delta^0) & -\sin(\delta^0) \\ \sin(\delta^0) & \cos(\delta^0) \end{bmatrix} \Delta x_2 + \begin{bmatrix} -\sin(\delta^0) & -\cos(\delta^0) \\ \cos(\delta^0) & -\sin(\delta^0) \end{bmatrix} \begin{bmatrix} x^0_{2,d} \\ x^0_{2,q} \end{bmatrix} \Delta\delta, \tag{4.11}$$

where we have simplified notation by writing $\delta^0 := \delta^0_2 - \delta^0_1$, and $\delta := \delta_2 - \delta_1$ .

This process can be simplified by understanding which variables in particular need to be transformed. To model the dynamics of the interconnecting distribution lines, the output inverter currents of individual subsystems $I_o$ need to be transformed to a global reference frame. Oppositely, the interconnecting distribution lines need to be transformed to a local reference frame to correctly model their interactions with individual subsystems. For clarity, variables in the global reference frame are designated as $X_{DQ}$, while variables in a local frame are designated as $X_{dq}$.

The dynamics associated with the distribution line connecting nodes $i$ and $j$ can then be modeled as:

$$\begin{aligned} \dot{I}_{l,ij,D} &= \frac{1}{L_{l,ij}}(V_{bi,D} - R_{l,ij} I_{l,ij,D} - V_{bj,D}) + \omega I_{l,ij,Q} \\ \dot{I}_{l,ij,Q} &= \frac{1}{L_{l,ij}}(V_{bi,Q} - R_{l,ij} I_{l,ij,Q} - V_{bj,Q}) - \omega I_{l,ij,D}, \end{aligned} \tag{4.12}$$

which can be linearized around its steady state as:

$$\begin{aligned}\Delta\dot{I}_{l,ij,D} &= \frac{1}{L_{l,ij}}(\Delta V_{bi,D} - R_{l,ij}\Delta I_{l,ij,D} - \Delta V_{bj,D}) + \omega^0 \Delta I_{l,ij,Q} + \Delta\omega I^0_{l,ij,Q} \\ \Delta\dot{I}_{l,ij,Q} &= \frac{1}{L_{l,ij}}(\Delta V_{bi,Q} - R_{l,ij}\Delta I_{l,ij,Q} - \Delta V_{bj,Q}) - \omega^0 \Delta I_{l,ij,D} + \Delta\omega I^0_{l,ij,D},\end{aligned} \tag{4.13}$$

with associated state variables

$$x_{net,ij} = [I_{l,ij,D}, I_{l,ij,Q}]. \tag{4.14}$$

Note that here we have distinguished between $V_{b,DQ}$ and $V_{b,dq}$. As each voltage bus is connected to a resistive load, the respective voltages can be expressed in the global reference frame as:

$$\begin{aligned}V_{bj,D} &= R_j(I_{oj,D} - I_{wj,D} + \sum_i H(i,j) I_{l,ij,D}) \\ V_{bj,Q} &= R_j(I_{oj,Q} - I_{wj,Q} + \sum_i H(i,j) I_{l,ij,Q}),\end{aligned} \tag{4.15}$$

where $H$ is a matrix that describes the interconnections such that $H(i,j) = 0$ if nodes $i$ and $j$ are not connected, $H(i,j) = 1$ if the nominal direction of current flow is from $i$ to $j$, and $H(i,j) = -1$ if the nominal direction of current flow is from $j$ to $i$. $I_{oj,D}$ and $I_{oj,Q}$ refer to the current flowing from the local inverter to the voltage bus, while $I_{wj,D}$ and $I_{wj,Q}$ refer to the current drawn by the dynamic load, expressed in the global reference frame.

Similarly, the bus voltages can be expressed in the local reference frame as:

$$\begin{aligned}V_{bj,D} &= R_j(I_{oj,d} - I_{wj,d} + \sum_i H(i,j) I_{l,ij,d}) \\ V_{bj,Q} &= R_j(I_{oj,d} - I_{wj,q} + \sum_i H(i,j) I_{l,ij,q}),\end{aligned} \tag{4.16}$$

where $I_{l,ij,d}$ and $I_{l,ij,q}$ refer to the line currents expressed in the reference frame of subsystem $j$.

The overall microgrid topology can be seen in 4.2.

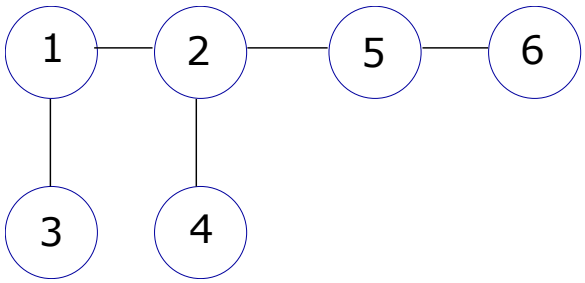


Figure 4.2: Overview of general microgrid structure.

### 4.2.4 Overall System Model

As shown in equations 4.8, 4.5, and 4.13, the state variables associated with the individual inverter-connected DERs as well as those of the network are therefore interconnected. To express the full system dynamics, we denote the set of state variables $X$ as the collection of all state variables associated with each DER as given in equations 5.2 and 4.7, and the state variables associated with the network interconnections given in 4.14:

$$X = [x_{s,1}, \ldots, x_{s,n_s}, x_{f,1}, \ldots, x_{f,n_f}, x_{net}]^T. \tag{4.17}$$

Similarly, we express the set of control inputs $U$ to the microgrid as the collection of grid-feeding voltages as given in equation 4.9:

$$U = [u_{f,1}, \ldots, u_{f,n_f}]^T, \tag{4.18}$$

while the set of disturbance inputs $W$ to the microgrid is the collection of dynamic currents given in 4.15:

$$W = [I_{w1,D}, \ldots, I_{wn,D}, I_{w1,Q}, \ldots, I_{wn,Q}]. \tag{4.19}$$

In general, these relationships can be summarized to express the LTI dynamics of the

microgrid state:

$$\dot{X} = AX + BU + GW. \tag{4.20}$$

## 4.3 Control Design

Generally the bulk of inverter-connected power sources will be grid-supporting/droop-controlled, which results in desirable power-sharing characteristics. However the power output from a droop-controlled inverter cannot be independently modulated in order to improve transient microgrid performance. If the grid as a whole is seen as a controlled dynamic system, then the grid-feeding inverters represent the control actuators to this system. The goal of this control task is to modulate the power from these grid-feeding inverters to improve the transient characteristics of the microgrid.

In a given microgrid, we assume that there are a fixed number of inverter-connected sources, which may either be treated as grid-supporting or grid-feeding. In master-follower control schemes, it may be sufficient to designate a single frequency-setting (grid-supporting) power source, while the remainder of the power sources are grid-feeding. However such configurations may detract from the redundancy and robustness of the microgrid, because grid-feeding inverters cannot independently set a frequency, and the loss of the single frequency-setting unit in such cases may be catastrophic for grid stability. Therefore a secondary goal of the control problem is to identify the extent to which grid-wide improvements may be had from as few of these grid-feeding "controllers" as possible. To this end, we explore grid topologies in which a single controlled source can result in grid-wide improvements, as well as configurations in which a single controlled source is ineffective.

In the 'uncontrolled' case, all inverters are equipped with a droop mechanism, which

is a decentralized controller that only requires local power measurements. This is denoted as uncontrolled to denote the idea that in this scenario we cannot independently modulate the state of individual source; the voltages and frequencies are coupled to the active and reactive loads as in equation 4.1. Alternatively, in the 'controlled' case, one or more inverters are designated to be grid-feeding and are fitted with decentralized H-infinity controllers whose design will now be explained; such methods have been applied to microgrids in [59, 67]. These controlled grid-feeding inverters are tuned such that the overall steady-state power sharing is unchanged relative to the droop-controlled variation.

### 4.3.1 Decentralized Controller Design

The goal for controller synthesis in this problem is to be both (1) optimal and (2) decentralized. These two goals are achievable via decentralized H-infinity controllers. The control methods used in this paper are outlined in this section. The algorithms used for controller synthesis are not the contribution of this work, but are simply stated here for clarity and completeness. The control-based contribution of this research is instead in designing a suitable cost function that can result in transient improvements, as well as identifying topologies in which this decentralized control mechanism may be useful for microgrid applications.

To obtain optimal performance in the microgrid, the objective is to minimize the effects that grid disturbances have on power quality, without excessive control action. For example, if the demand suddenly spikes, as might be expected with a large load suddenly being switched on, we would like our controller to inject a moderate amount of power into the system such that the microgrid frequency does not drastically drop or oscillate. The

formal objective of this H-infinity controller is to minimize the infinity-norm associated with the transfer function from the disturbance to the set of variables we would like to minimize. In our case, the 'disturbance,' $W$, is the dynamic load:

$$W = [I_{w1,d}, I_{w1,q}, \ldots, I_{wn,d}, I_{wn,q}]^T, \tag{4.21}$$

while the 'set of variables we would like to minimize,' $z$, is the weighted vector of frequencies and power supplied by the grid-feeding inverter:

$$Z = [\omega_1, \omega_2, \ldots, \omega_n, \alpha_1 P_f, \alpha_2 Q_f]^T. \tag{4.22}$$

Note that we have weighted the power supplied by the grid-feeding inverter in order to tune the controller performance.

We can express this dynamic system as

$$\begin{aligned} \dot{X} &= AX + BU + GW \\ Z &= C_z X + D_z U. \end{aligned} \tag{4.23}$$

For linear state feedback of the form $u = -KX$ we can impose a decentralized constraint on our control via a structured matrix $K$. In this problem we do not consider the challenge of noise-polluted output feedback of the form $u = -K(CX + v)$; the goal is instead to identify the limits of decentralized control. A controller that is a function of only local information, i.e. local state variables at the given grid-feeding DER, can be expressed as

$$u_i = K_i x_{f,i}. \tag{4.24}$$

Over the full microgrid,this can be interpreted as a structured constraints on the feedback

matrix $K$:

$$K = \begin{bmatrix} K_1 & 0 & \dots & 0 & 0 \\ 0 & K_2 & & & 0 \\ \vdots & & \ddots & & \vdots \\ 0 & & & K_n & 0 \end{bmatrix}. \tag{4.25}$$

The associated closed loop system can then described by

$$\begin{aligned} \dot{X} &= A_{cl}X + GW \\ Z &= C_z X + D_z U, \end{aligned} \tag{4.26}$$

where

$$A_{cl} = A - B_u K, \tag{4.27}$$

with an associated transfer function from $W$ to $Z$, $T_{wz,cl}$.

Following [63], an upper bound of the infinity norm of this closed-loop system can be found by manipulating the bounded real lemma; this methodology has been outlined in previous sections but will be briefly restated here for completeness. As described in [64, 65, 66, 68] a controller can be found to minimize this supremum by casting the problem as a semidefinite program:

$$\begin{aligned} &\underset{X,Y}{\text{maximize}}\ \eta \\ &\text{subject to } X_q \succ 0,\ X_r \succ 0,\ \eta > 0, \\ &\qquad \begin{bmatrix} \Psi(X,Y) + \eta G G^T & * \\ C_z X + D_{uz} Y & -I \end{bmatrix} \prec 0. \end{aligned} \tag{4.28}$$

where we define

$$\Psi(X,Y) := AX + XA^T + BY + Y^T B^T. \tag{4.29}$$

Here $X$ and $Y$ are optimization variables of appropriate dimension. Note that since the matrix is constrained to be negative definite, and thus symmetric, the $*$ is simply used as a placeholder to denote the appropriately transposed entries.

Table 4.1: Load, line parameters for microgrid, given in p.u.

| $R_{l,ij}$ | $X_{l,ij}$ | $R_{o,j}$ | $X_{o,j}$ | $R_j$ |
|---|---|---|---|---|
| 0.0125 | 0.0125 | 0.0042 | 0.0208 | 0.4155 |

The resultant controller is optimized in the sense that the infinity norm is bounded by $\eta$:

$$\|T_{wz,cl}\|_\infty \leq \eta. \tag{4.30}$$

As outlined in [68, 65], this controller can be constrained to be decentralized by implementing a block-diagonal structure on $X$ and the desired zero-nonzero structure on $Y$. This convex problem can be efficiently solved using solvers described in [69, 70].

## 4.4 Results

### 4.4.1 Simulation Parameters

The modeled microgrid is a 6-node microgrid whose structure is illustrated in 4.2. The microgrid parameters are adopted from [61], and are shown in table 4.1. Note that $X_l, X_o$ are simply the reactance associated with $L_l, L_o$, the distribution line inductance and the inverter output filter inductance, respectively. All filters and distribution lines are modeled identically. Similarly, the droop gains are given (in p.u.) as $m_p = 5.64$ and $n_q = 0.0205$.

We simulate a disturbance at node 1 via a 5% step load increase, relative to the steady-state power consumption at node 1. In the following simulations, the location and controller-type are varied, and the results are compared.

In the 'uncontrolled' scenario, all DERs are controlled via a droop mechanism. We then consider three 'controlled' scenarios in order to demonstrate the role of microgrid topol-

ogy on the controlled mitigation of this disturbance. In all examples, the disturbance is at node 1 as described previously.

We consider the situation in which not all of the DERs are of equal rating; we designate a node $f$ such that the DER at node $f$ has half the power capacity as the other identical DERs. This characteristic can be reflected in the grid-supporting case by modifying the droop gain at node $f$; as the droop gain actuates the steady-state power sharing, we adjust the droop gain $m_p$ such that

$$m_{p,f} = 2m_{p,j}, \qquad j \neq f. \tag{4.31}$$

In the controlled case, DER $f$ is instead modulated via the decentralized H-infinity controller. To achieve proportional steady-state power sharing that matches the droop-controlled case, the controller gains are experimentally tuned.

### 4.4.2 Topology 1: Adjacent Controller Connected to Only 1 Node

In this configuration, the controlled grid-feeding DER is at node 3 ($f = 3$). This topology is shown in figure 4.3, where it can be seen that node 3 is located immediately adjacent to the disturbance at node 1; in addition, the controller is connected to no other microgrid nodes. The controller at node 3 only measures its own state variables as listed in 4.7, as well as the frequency of the adjacent node 1.

The microgrid frequency dynamics following the perturbing load change can be seen in figure 4.4. It is evident that when each inverter-connected DER is fitted with a droop, the microgrid frequencies experience a much longer transient than the case in which the controller at DER 3 is switched from droop to the decentralized H-infinity case. The settling time is

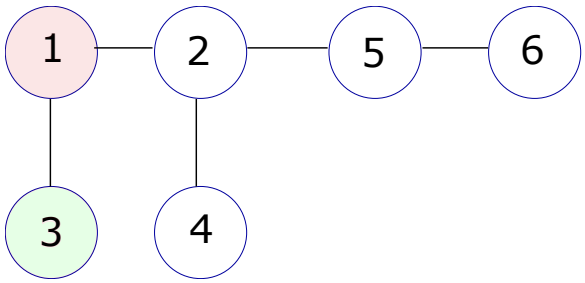


Figure 4.3: Controlled grid-feeding DER located at node 3, with a disturbance at node 1.

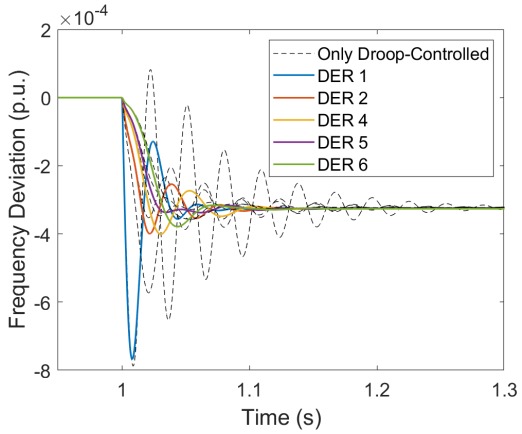


Figure 4.4: Comparing the 'uncontrolled' (only droop-controlled) microgrid frequencies to the 'controlled' microgrid frequencies, in which a controlled grid-feeding DER is located at node 3. Individual DER frequencies are labeled for the 'controlled' case.

reduced from approximately 0.30 seconds to 0.12 seconds, a 60% reduction. In addition, the total power consumption is approximately consistent between both cases, as shown in figure 4.5; no excessive power spikes are required to mitigate this transient behavior.

### 4.4.3 Topology 2: Adjacent Controller Connected to Multiple Nodes

In the second configuration we explore the role of controller connectivity with respect to microgrid stability. The controlled grid-feeding DER is now located at node 2; this

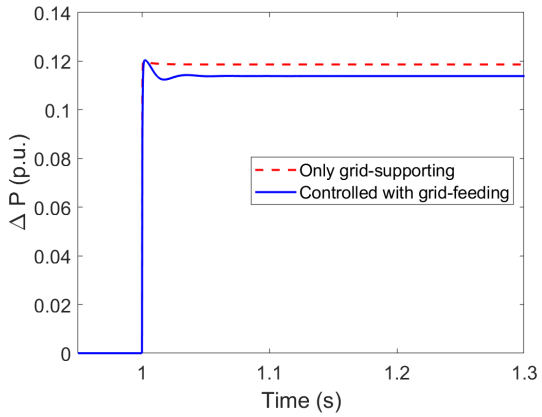


Figure 4.5: Comparing the total power consumption between the 'uncontrolled' and 'controlled' cases.

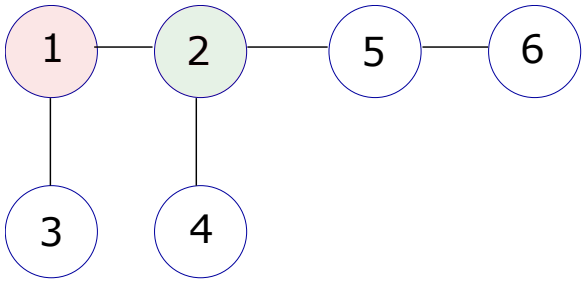


Figure 4.6: Controlled grid-feeding DER located at node 2, with a disturbance at node 1.

topology is illustrated in figure 4.6. This topology differs from the previous case because of the multiple connections at node 2; the controller is now connected to both nodes 1, 4, and 5. The controller at node 3 only measures its own state variables as listed in 4.7, as well as the averaged frequency of the adjacent nodes 1, 4, and 5.

The grid frequency dynamics following the perturbing load change can be seen in figure 4.7. The overshoot and qualitative transient behavior, in both the 'controlled' and 'uncontrolled' cases differ from the previous scenario; this can be attributed to the different effect that a smaller source at node 2 has on the overall network dynamics. As before, when

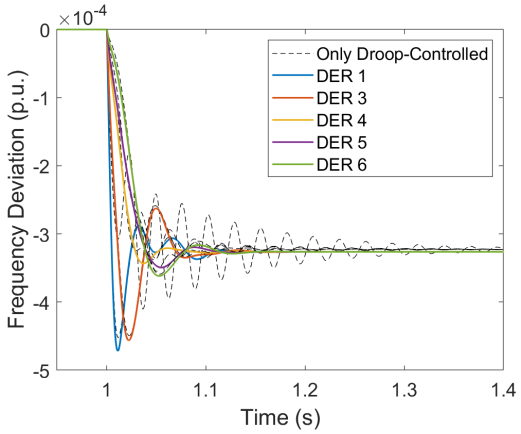


Figure 4.7: Comparing the 'uncontrolled' (only droop-controlled) microgrid frequencies to the 'controlled' microgrid frequencies, in which a controlled grid-feeding DER is located at node 2. Individual DER frequencies are labeled for the 'controlled' case.

inverter-connected DER is fitted with a droop, the microgrid frequencies experience a much longer transient than the case in which the controller at DER 2 is switched from droop to the decentralized H-infinity case. In this case, although the peak frequency undershoot was not as prominent, the settling time in the uncontrolled case extended to approximately 0.4 seconds. The controlled configuration showed a settling time of approximately 0.12 seconds- a 70% reduction.

In the previous case, the controller at node 3 had some estimate of the disturbance as it made use of the frequency measurement at node 1. However in this case, there is no exact measurement of the disturbance available; the controller at node 2 only has access to the *averaged* frequency of its adjacent nodes 1, 4, and 5. This provides some evidence that it is the proximity or location of the controller, rather than the measured variable, which can result in improved grid-wide performance.

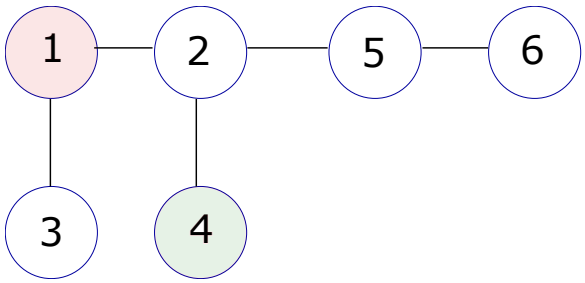


Figure 4.8: Controlled grid-feeding DER located at node 4, with a disturbance at node 1.

### 4.4.4 Topology 3: Nonadjacent Controller Connected to Only 1 Node

In the third configuration we explore the role of controller proximity with respect to microgrid stability. In this case, the controlled grid-feeding DER is at node 4; this topology is illustrated in figure 4.8. As before, the controller at node 4 only measures its own state variables as listed in 4.7, as well as the frequency of the adjacent node 2.

As with the previous examples, the DER at node 4 is now assumed to have a smaller power capacity:

$$m_{p,4} = 0.2m_{p,j}, \qquad j \neq 4. \tag{4.32}$$

The associated frequency dynamics following the disturbance can be seen in figure 4.9. In this case, we observe that the grid demonstrates no notable harmonic ringing, as in the previous two cases; the smaller DER at 4 has a marginal destabilizing effect on the grid as a whole. As a result we observe approximately no reduction in frequency harmonics; the controller is unable to effectively improve the transient microgrid dynamics.

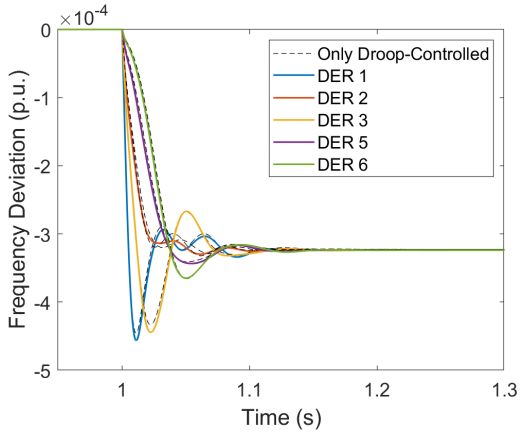


Figure 4.9: Comparing the 'uncontrolled' frequencies to the 'controlled', in which a controlled grid-feeding DER is located at node 4. Individual DER frequencies are labeled for the 'controlled' case.

## 4.5 Conclusion

We present these results to develop the idea that the microgrid topology can have an important role in the resultant power quality of the grid. The results have shown that microgrid stability can suffer depending on the location of individual power sources. Even if the same total power is supplied, the network between DERs can significantly affect the resultant power quality harmonics. As was presented in topologies 1 and 2, the presence of the weaker power source immediately adjacent to the disturbance resulted in grid-wide ringing; alternatively, this harmonic behavior was not observed in topology 3, when the weaker power source was no longer directly connected to the disturbed node.

These results also show that the differences are not simply a function of the number of nodes connected to the weaker power source. In both topology 1 and topology 3, the weak DER was connected to only one other node, and yet the transient microgrid frequencies were drastically different.

Moreover, we have showed that in such cases, replacing the grid-supporting inverter at the weak DER with a grid-feeding inverter equipped with a decentralized H-infinity controller results in significantly improved transient behavior without requiring additional sensor data. This proposed design improves microgrid performance without the need for additional sensor data which may be costly or technically infeasible.

# Chapter 5

# Optimal Model-Based Improvements for Decentralized Control

## 5.1 Overview

The contribution of this work is in modifying the droop characteristic in order to improve transient microgrid performance in the primary control timescale. We have augmented the V/F droop with a controlled variable so as to mitigate undesirable features of the microgrid power quality, such as excessive overshoot or harmonics in the grid frequency. This controlled augmentation is constrained to be zero in the steady-state, thus preserving the desirable steady-state load sharing intrinsic to conventional droop controllers.

The controller is designed to be optimal in the H-infinity sense, to make the closed-loop system more robust to model and parameter uncertainty. In addition, the proposed controller requires only decentralized data in real-time, and only a limited model (i.e. a model of its neighboring nodes) in order to be synthesized. The resulting control shows superior transient performance to conventional droop control, at comparatively little cost.

## 5.2 Model

For this work, all inverters are treated as grid-supporting. This has been explained in the previous chapter, but for clarity the model of the grid-supporting inverter is briefly

restated here:

$$
\begin{aligned}
V_{j,gd} &:= V^0_{j,gd} - n_q(Q - Q^0) \\
V_{j,gq} &:= 0 \\
\omega_j &:= \omega^0_j - m_p(P - P^0) \\
\dot{\delta}_j &= \omega_j \\
\dot{P}_j &= \tau(V_{j,gd}I_{j,od} + V_{j,gq}I_{j,oq} - P_j) \\
\dot{Q}_j &= \tau(V_{j,gq}I_{j,od} - V_{j,gd}I_{j,oq} - Q_j) \\
\dot{I_{oj,d}} &= \frac{1}{L_{oj}}(V_{gj,d} - R_{oj}I_{oj,d} - V_{bj,d}) + \omega I_{oj,q} \\
\dot{I_{oj,q}} &= \frac{1}{L_{oj}}(V_{gj,q} - R_{oj}I_{oj,q} - V_{bj,q}) - \omega I_{oj,d}.
\end{aligned}
\tag{5.1}
$$

We can identify the dynamic state associated with the grid-supporting subsystem as

$$x_j = [\omega_j, \delta_j, P_j, Q_j, I_{oj,d}, I_{oj,q}]^T, \tag{5.2}$$

where $\omega$ is the frequency of the inverter, $\delta$ is its phase, $P$ and $Q$ are the filtered measurements of active and reactive power respectively, and $I_o$ is the output current from the inverter to the node voltage bus. The nonlinear model can be linearized about the steady-state, $x^0_j$,

such that the new dynamic variables are designated $\Delta x_j = x_j - x_j^0$, as follows

$$\begin{aligned}
\Delta V_{j,gd} &:= -n_q(\Delta Q) \\
\Delta V_{j,gq} &:= 0 \\
\Delta \omega_j &:= -m_p(\Delta P) \\
\Delta \dot{\delta}_j &= \Delta \omega_j \\
\Delta \dot{P}_j &= \tau(\Delta V_{j,gd} I^0_{oj,d} + V^0_{j,gd} \Delta I_{oj,d} + \Delta V_{j,gq} I^0_{oj,q} + V^0_{j,gq} \Delta I_{oj,q} - \Delta P_j) \\
\Delta \dot{Q}_j &= \tau(\Delta V_{j,gq} I^0_{oj,d} + V^0_{j,gq} \Delta I_{oj,d} - \Delta V_{j,gd} I^0_{oj,q} - V^0_{j,gd} \Delta I_{oj,q} - \Delta Q_j) \\
\Delta \dot{I}_{oj,d} &= \frac{1}{L_{oj}}(\Delta V_{gj,d} - R_{oj} \Delta I_{oj,d} - \Delta V_{bj,d}) + \omega^0 \Delta I_{oj,q} + \Delta \omega I^0_{oj,q} \\
\Delta \dot{I}_{oj,q} &= \frac{1}{L_{oj}}(V_{gj,q} - R_{oj} I_{oj,q} - V_{bj,q}) - \omega^0 \Delta I_{oj,d} - \Delta \omega I^0_{oj,d}.
\end{aligned} \tag{5.3}$$

## 5.3 Controller Design

The general droop characteristic for a voltage-source inverter can be expressed as:

$$\begin{aligned}
\omega &:= \omega_0 - m_p(P - P_0) \\
V_d &:= V_{d0} - n_q(Q - Q_0) \\
V_q &:= 0.
\end{aligned} \tag{5.4}$$

Therefore if the inverter sees an increased real power load of $\Delta P$, the inverter will lower its frequency by $m_p \Delta P$. This relatively simple control is effective in that it allows for desirable steady-state power sharing, in that a network of $n$ droop-controlled inverters in parallel will proportionally share the load relative to their droop gain:

$$m_1 \Delta P_{1,ss} = m_2 \Delta P_{2,ss} = \cdots = m_n \Delta P_{n,ss}. \tag{5.5}$$

In the proposed design, the controller retains this steady-state sharing while tuning the transient behavior.

Instead of seeing the power load, $P$ and $Q$, the controller instead reads

$$\begin{aligned} \hat{P} &= P - P_v \\ \hat{Q} &= Q - Q_v, \end{aligned} \tag{5.6}$$

such that frequency and voltage are controlled as

$$\begin{aligned} \omega &:= \omega_0 - m_p(\hat{P} - P_0) \\ V_d &:= V_{d0} - n_q(\hat{Q} - Q_0) \\ V_q &:= 0, \end{aligned} \tag{5.7}$$

where $P_v$ and $Q_v$ are 'virtual' power injections. By this we mean that no actual power is added to the system, but the inverter is controlled as though the load were actually $\hat{P}, \hat{Q}$, rather than $P, Q$.

The intention of this controller is only to improve the transient droop behavior; the steady-state load sharing should be unchanged:

$$\begin{aligned} \hat{P}_{ss} &= P_{ss} \\ \hat{Q}_{ss} &= Q_{ss}. \end{aligned} \tag{5.8}$$

This is accomplished via integral control; we augment the state vector to create the variables $U_P, U_Q$, such that

$$\begin{aligned} \dot{U}_P &= P_v \\ \dot{U}_Q &= Q_v. \end{aligned} \tag{5.9}$$

In this way, if the system can be controlled to a steady state where time derivatives are zero, then $P_{v,ss} = Q_{v,ss} = 0$. The goal of the controller is therefore to determine $P_v$ and $Q_v$ in such a way that the microgrid dynamics demonstrate improved performance.

It is important to note that in this design, no additional power is required on behalf of the inverter. While the droop-controlled update responds as though the active and reactive power loads were adjusted by $P_v, Q_v$, these are simply signals computed by the controller that are then used to adjust the voltage and frequency update commands. Instead of modifying the output power and keeping the droop characteristic fixed, we are modifying the droop characteristic and keeping the output power fixed.

## 5.4 Model Reduction for Controller Synthesis

A numerical challenge was observed during the controller synthesis; namely the dynamics of the microgrid presented timescales at significantly different orders of magnitude. To address this issue, the controller synthesis involved reducing the model to focus on the slower timescales, which dominated the power quality dynamics. The controller was then generated in this reduced space, and then expanded to operate in the full space.

This issue is visualized in figure 5.1, which illustrates the eigenvalues of the sample 6-node microgrid on the complex plane. In this figure, it is clear that there are several eigenvalues of relatively exceptional magnitude. These suggest that there are some dynamic modes in this system that are considerably 'fast,' in the sense that dynamic perturbations along these modes are attenuated considerably faster compared to similar disturbances on the 'slower' modes.

This behavior can be understood intuitively. We cannot in general associate specific states with specific eigenvalues, but we can consider the physical attributes of the modeled states and draw conclusions about what may be reduced. In this case there are several characteristic timescales that are intrinsic features of the model: those along the R-L circuits

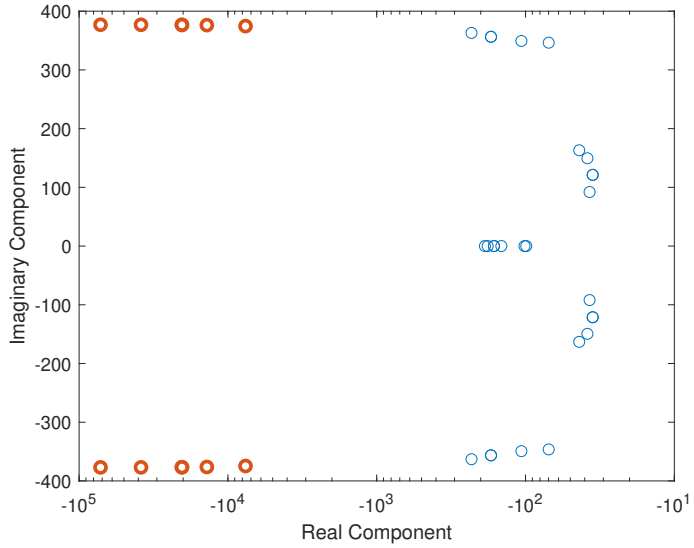


Figure 5.1: Eigenvalues of linearized 6-node microgrid model. Eigenvalues of significantly greater magnitude have been shown in red.

in $I_o$ and $I_l$, and those of the low-pass filters of the droop controller that are used to measure $P$ and $Q$. These filtered measurements are then used to compute inverter frequency, inverter voltage, and inverter phase, so we would not expect the timescale of these dynamics to be significantly faster than the characteristic timescale associated with $P$ and $Q$. The characteristic timescale associated with the RL circuits,

$$\tau_{RL} = \frac{L}{R} \approx 10^{-4} \tag{5.10}$$

is much faster than the characteristic timescales associated with the low-pass filters

$$\tau_f \approx 10^{-2}. \tag{5.11}$$

. This made for poor numerical conditioning, which in turn made it difficult for the convex solvers to converge on an optimal controller.

As we are concerned with controlling the transient power quality, i.e. the voltage and frequency of the microgrid, the focus of this research coincides with these slower timescales. Since the RL dynamics are much faster than the remainder of the microgrid, we treat these fast dynamics as quasi steady-state; instead of being modeled as differential equations, these variables are modeled algebraically.

This model reduction can be formalized as follows. We denote the set of 'fast' variables as $x_f$ and the set of 'slow' variables as $x_s$, so that the microgrid dynamics can then be rewritten as

$$\frac{d}{dt}\begin{bmatrix} x_s \\ x_f \end{bmatrix} = \begin{bmatrix} A_s & A_{sf} \\ A_{fs} & A_f \end{bmatrix}\begin{bmatrix} x_s \\ x_f \end{bmatrix} + \begin{bmatrix} B_s \\ B_f \end{bmatrix} u + \begin{bmatrix} G_s \\ G_f \end{bmatrix} w. \tag{5.12}$$

The quasi-steady-state assumption means we take $\frac{dx_f}{dt} = 0$, so that

$$\begin{bmatrix} \frac{dx_s}{dt} \\ 0 \end{bmatrix} = \begin{bmatrix} A_s & A_{sf} \\ A_{fs} & A_f \end{bmatrix}\begin{bmatrix} x_s \\ x_f \end{bmatrix} + \begin{bmatrix} B_s \\ B_f \end{bmatrix} u + \begin{bmatrix} G_s \\ G_f \end{bmatrix} w. \tag{5.13}$$

This in turn yields a linear relationship for $x_f$ as a function of $x_s, u, w$:

$$A_f x_f = -A_{fs} x_s - B_f u - G_f w. \tag{5.14}$$

For the case of the microgrid, the fast variables are all linearly independent of each other; this is physically intuitive, as these dynamics are associated with distinct circuit lines. As a result, $A_f$ is invertible, and so

$$\begin{aligned} x_f &= A_f^{-1}(-A_{fs} x_s - B_f u - G_f w) \\ &= \tilde{A}_f x_s + \tilde{B}_f u + \tilde{G}_f w, \end{aligned} \tag{5.15}$$

where $\tilde{A}_f := -A_f^{-1} A_{fs}$, $\tilde{B}_f := -A_f^{-1} B_f$, and $\tilde{G}_f := -A_f^{-1} G_f$. Therefore we can rewrite the reduced microgrid dynamics as:

$$\begin{aligned} \frac{dx_s}{dt} &= (A_s + A_{sf}\tilde{A}_f)x_s + (B_s + A_{sf}\tilde{B}_f)u + (G_s + A_{sf}\tilde{G}_f)w \\ &= A_r x_s + B_r u + G_r w, \end{aligned} \tag{5.16}$$

The state measurements can also be reduced in a similar fashion. Consider the controlled variables, $z$:

$$z = C_z + D_z u. \tag{5.17}$$

These can be rewritten as

$$\begin{aligned} z &= \begin{bmatrix} C_{z,s} & C_{z,f} \end{bmatrix} \begin{bmatrix} x_s \\ x_f \end{bmatrix} + D_z u \\ &= C_{z,s} x_s + C_{z,f}(\tilde{A}_f x_s + \tilde{B}_f u + \tilde{G}_f w) \\ &= (C_{z,s} + C_{z,f}\tilde{A}_f) x_s + (D_z + \tilde{B}_f) u + \tilde{G}_f w \\ &= C_{z,r} x_s + D_{z,r} u + G_{z,r} w, \end{aligned} \tag{5.18}$$

where $C_{z,r} := C_{z,s} + C_{z,f}\tilde{A}_f$, $D_{z,r} := D_z + \tilde{B}_f$ and $G_{z,r} := \tilde{G}_f$.

The measurement matrices can also be rewritten as

$$y = \begin{bmatrix} C_s & C_f \end{bmatrix} \begin{bmatrix} x_s \\ x_f \end{bmatrix} + Du + Hw. \tag{5.19}$$

However this step is not taken for this design. Instead, it was simply taken that all local variables in the 'slow' space were available for decentralized control. Therefore the measurements were instead taken as

$$\begin{aligned} y_r &= \begin{bmatrix} I_1 & 0 & \dots & 0 \\ 0 & I_2 & \dots & 0 \\ \vdots & & \ddots & \vdots \\ 0 & \dots & & I_n \end{bmatrix} \begin{bmatrix} x_{s,1} \\ x_{s,2} \\ \vdots \\ x_{s,n} \end{bmatrix} + v \\ &= C_{y,r} x_s + v. \end{aligned} \tag{5.20}$$

where $I_j$ are identity matrices sized appropriately for the state at node $j$, and $x_{s,j}$ refers to the reduced state at node $j$, and $v$ refers to noise along the measurement channels.

Following this procedure, we are left with a reduced model for the state propagation of $x_s$, along with measurement matrices $y_r$ and a set of controlled variables $z$:

$$\begin{aligned} \frac{dx_s}{dt} &= A_r x_s + B_r u + G_r w \\ y &= C_{y,r} x_s + v \\ z &= C_{z,r} x_s + D_{z,r} u + G_{z,r} w. \end{aligned} \tag{5.21}$$

This makes it possible to proceed with robust control synthesis via H-infinity methods.

Upon generating the feedback control matrix in the reduced space, $K_r$, it is then necessary to augment this control matrix in order to operate in the full space. The matrix is therefore augmented with appropriately sized zero matrices:

$$u = [K_r, 0_f] \begin{bmatrix} x_s \\ x_f \end{bmatrix}. \tag{5.22}$$

## 5.5 Robust Control Synthesis

The methods used to synthesize the controller follow the decentralized H-infinity controller synthesis procedures outlined in chapters 3 and 5; sections 3.1.2 and 5.3.1 provide more detail. In this case, the only variation is in the choice of matrices for the minimized variables, $z$.

Inverters equipped with the proposed control design were associated with two new sets of variables: (1) the control variables, $P_v$ and $Q_v$, as well as (2) the integral of these variables, $U_P$ and $U_Q$. These were not physical quantities, i.e. power is not explicitly injected under this approach.

The set of $z$ variables associated with node $j$ were constructed as

$$z_j = [\omega_j, \alpha_P P_{v,j}, \alpha_Q Q_{v,j}, \beta_P U_{P,j}, \beta_Q U_{Q,j}]^T. \tag{5.23}$$

If the inverter was not equipped with the proposed control design, then $z_j = \omega_j$. These are linear functions of the state variable, in the case of $\omega_j, U_P, U_Q$, or linear functions of the control variable, in the case of $P_v$ and $Q_v$, and so this can easily be added to the infinity-norm cost function. Different weights on these quantities resulted in different dynamic responses, which can be loosely intuited. For example, varying $\beta$, the weights on $U_P$ and $U_Q$, affected the dampening of the response, while varying $\alpha$, the weights on the control actuation, affected the magnitude of the control.

In the standard case, the 'full' model was used for controller synthesis. That is to say, the state space matrices defined by equation 5.3, which describe the dynamics of the full microgrid, are used during the semidefinite programming problem. In this sense, the resulting controller is designed such that its actions are intended to minimize a grid-wide cost.

### 5.5.1 Regional Model

Instead of synthesizing the decentralized controller with knowledge of the full microgrid model, the controller in the 'regional' case was developed using a limited model. Specifically, the regional model only included nodes and lines that were directly connected to the controller in question.

Figure 5.2 shows an example regional model, taken for the potential controller synthesis at node 3. Here it is shown that only neighboring nodes 2, 5, and 6, along with the associated connecting lines and node 3 itself, are included in this truncated model.

The purpose of this alternative model was to identify the extent to which the full microgrid model was necessary to develop a superior controller. An underlying microgrid

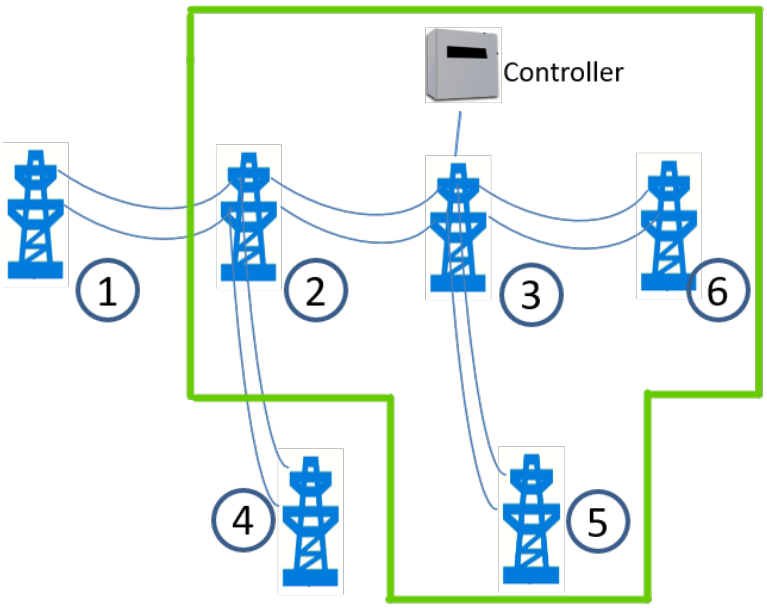


Figure 5.2: Example of truncated model for the 'regional' case; shown for potential controller synthesis at node 3. Only states that directly neighbor node 3 are included, as shown in green.

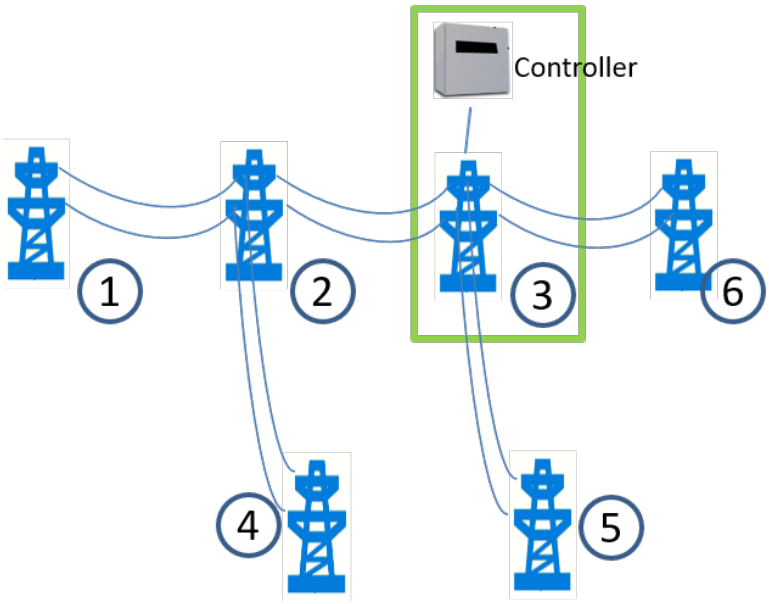


Figure 5.3: Example of truncated model for the 'solitary' case; shown for potential controller synthesis at node 3. Only the model of node 3 is included in this version.

theme is to be modular and robust to topology changes. Even though the full microgrid model would only be used during controller synthesis and not during actual operation, there is still a cost associated with having to know and access this full model; particularly in larger microgrids, this may be an unwelcome barrier to entry. A controller that only required a limited, smaller model would be significantly more tractable in such cases.

### 5.5.2 Solitary Model

Unlike the previous two cases, the controller in the 'solitary' case was developed using an extremely limited model that included only states at its local node. Like the regional case, the purpose of this variation was to identify the extent to which the microgrid model was necessary for the controller to improve grid-wide performance.

| $R_{l,ij}$ | $X_{l,ij}$ | $R_{o,j}$ | $X_{o,j}$ | $R_j$ | $m_j$ | $n_j$ |
|---|---|---|---|---|---|---|
| 0.0125 | 0.0125 | 0.0042 | 0.0208 | 0.4155 | 5.640 | 0.021 |

Table 5.1: Load, line parameters for microgrid, given in p.u.

This represented the least amount of model-based information. An example of the solitary model is shown in figure 5.3. The topology-free synthesis should be the most modular, and robust to topology changes, but suffers from the lack of model-based information to guide its control action.

## 5.6 Results

We simulate conditions to explore microgrid performance along 3 axes. (1) We have considered the grid performance as droop gain is varied, and how the microgrid may be stabilized in response. (2) We have also considered different levels of model fidelity, and how this relates to controller performance. (3) We have finally shown how microgrid power quality can be improved with a varying number of controllers. In this way we hope to identify methods to offer significant improvement to microgrid performance, at minimal additional cost; fewer controllers, which require simpler models, are easier to implement.

Microgrid parameters are given in the per-unit basis in table 5.1, and are consistent with microgrid parameters used in [61, 11]. Aside from the droop gain, which will be discussed, all other quantities are kept identical across the microgrid, to avoid confounding variables. $R_l$ and $X_l$ describe the resistance and reactance on lines connecting nodes to each other. $R_o$ and $X_o$ describe the resistance and reactance within the node, on the line connecting the inverter to the node bus. $R$ describes the resistance of the static load at the node. $m$ and $n$ describe the droop gains for the P-F droop and Q-V droop, respectively.

For the following simulations, we consider three microgrid scenarios in order to illustrate the challenges faced by a droop-controlled network. In these individual cases, the droop gain on a single inverter is modified to show how the inclusion of a single power source may destabilize a conventionally controlled microgrid. These scenarios also illustrate how the proposed control design can add significant robustness to the grid.

While some test situations may involve identical power sources, a more realistic condition is the case in which not all generators are identically rated, in the sense that the individual power sources may have different capacities. A wind farm may not have the same rating as a storage bank, for example. To simulate this case, we can vary the droop gain on the inverter. Along the P-F channel, a smaller droop gain implies that the associated power source is larger, and thus a unit change in active power has a weaker effect on the output frequency; a larger droop gain implies that the associated power source is smaller, where a unit change in active power has a stronger proportional effect on the output frequency. Such scenarios have been considered problematic for microgrids, as described in the earlier literature review.

We have simulated a microgrid response to a disturbance at node 2; the associated microgrid configuration is shown in figure. The disturbance is taken to be a 20 percent step increase in active power load relative to the equilibrium load at node 1; this represented a 3.34% active power increase relative to the equilibrium load on the microgrid as a whole. This was taken to simulate a sudden demand increase, as might be the case with electrical machinery that is suddenly switched on.

In this scenario, we vary the rating of generator 3, while keeping the remainder of the generators identically rated. The following simulations show the response of the

conventionally droop-controlled microgrid alongside the response of the microgrid with the proposed adjustments to the droop controller. We show the frequency response, as well as power output from each node, to confirm that the transient power sharing between generators is improved, with the same steady state power sharing.

As a first test scenario, all generators are identical. For the second test condition, we set the rating of generator 3 to be 67% that of the other generators. In the second test condition, we set the rating of generator 3 to be 50% that of the other generators.

These simulations are repeated for varying degrees of control. We show how the microgrid responds with "full model", "regional", and "solitary" controllers as described in 5.5; as previously mentioned, the motivation for these variations is to identify the degree of modularity that these model-based controllers require to actuate improved power quality. To continue this theme, we also show how the microgrid responds with a varying proportion of controllers. In addition to the cases where all droop controllers are 'conventional,' and when all droop controllers are 'adjusted,' we also show the case where varying proportions of controllers are 'adjusted,' so as to identify the degree to which additional control is needed for grid-wide improvement.

### 5.6.1 Metrics

The results are quantified across a variety of metrics. Robustness is measured by considering the H-infinity norm of the system. Overall dynamic performance is compared by evaluating changes in peak undershoot and settling time with respect to inverter frequencies, as these represent standard markers for the response of a dynamic system. Undershoot is taken as the maximum difference between the frequency signal and its final settling time.

Settling time is taken to be the time required for the signal to decay to within 5% of its final steady-state value. For the microgrid, the largest of these values across all inverter output frequencies was recorded. The goal is for the droop control adjustment to result in a shorter settling time with minimal undershoot.

We also consider the 'synchronism' of the microgrid, i.e. how out of phase the individual inverters are with each other. To quantify this, we look at the time-varying variance sampled across all frequencies; when all inverters are in phase with each other, this variance is 0. We present both the peak reduction in variance, as well as the change in variance integrated over time to provide a measure of the overall change in variance.

### 5.6.2 Summarized Results

The results across all simulations are shown in Tables 5.2, 5.3 and 5.4, where the change in various quantities is shown for the controlled vs. uncontrolled cases. 'Model' refers to the type of grid model used during controller synthesis, while 'controller' describes which nodes were equipped with adjusted droop controllers. $\|T(s)\|_\infty$ is the infinity norm of the system, with $z$ matrices as described in the controller synthesis section. $M_p$ is the percent undershoot, $\tau_s$ is the settling time, and $\sigma^2$ is the variance taken across inverter frequencies. Figures associated with all cases can be found in the appendices.

We have omitted results associated with the 'solitary' model, aside from the case where all inverters were equipped with an adjusted droop controller. In this case, no noteworthy improvements were observed even when all inverters included an adjusted droop controller, and thus there was no value to be found from further reducing the level of control. This reasoning matched observations, and as such these results are not included. For

a similar reason, we have not included the 'solitary' or 'regional' simulations where only a single controller is equipped with an adjusted droop controller. Even when the controller was designed using the full model, the microgrid performance showed no real improvements; further controller reduction by minimizing the model resulted in insignificant changes.

There are three major results worth highlighting at this juncture. First, by comparing results across model-type, it can be seen that more detailed models are helpful in terms of allowing the resultant controller to better stabilize the microgrid. However, the depth of the model offers a decreasing return; the losses observed with the 'solitary' model are obvious, but there was little change between the 'full' and 'regional' models.

Second, as the droop gain at node 3 is lowered, the microgrid becomes less stable to disturbances. However the proposed control design allows for comparatively stable operation despite this sensitivity.

Third, controller location is relevant to the controlled response of the microgrid. Configurations in which only one of the possible inverters was equipped with the proposed control design resulted in significantly inferior performance compared to the cases where two or more inverters were thus controlled. However there was little gain to be found from having all inverters controlled, compared to the judicious selection of some inverters to be controlled, as evidenced by the comparison between 'all' and '2, 3' controller configurations.

| Model | Controller | $\Delta\|T(s)\|_\infty$ | $\Delta M_p$ | $\Delta\tau_s$ | $\Delta\sigma^2_{peak}$ | $\Delta\int\sigma^2 dt$ |
|---|---|---|---|---|---|---|
| Full | All | 12.5% | 41.2% | 33.2% | 30.5% | 48.8% |
| Full | 2, 3 | 12.5% | 43.3% | 24.2% | 32.5% | 30.8% |
| Full | 3 | −0.6% | 0.7% | 5.0% | −0.6% | 0.3% |
| Regional | All | 12.5% | 53.8% | 17.4% | 32.3% | 31.7% |
| Regional | 2, 3 | 8.3% | 45.1% | 22.8% | 32.3% | 26.3% |
| Solitary | All | 4.5% | 7.7% | 23.6% | 5.0% | 6.9% |

Table 5.2: A summary of the results across all simulations when the rated power at all nodes is identical. Metrics are shown as the percentage decrease in the respective quantity in the controlled case, relative to the uncontrolled case (i.e. positive values represent a decrease, negative values represent an increase).

| Model | Controller | $\Delta\|T(s)\|_\infty$ | $\Delta M_p$ | $\Delta\tau_s$ | $\Delta\sigma^2_{peak}$ | $\Delta\int\sigma^2 dt$ |
|---|---|---|---|---|---|---|
| Full | All | 7.8% | 60.1% | 25.8% | 34.6% | 54.5% |
| Full | 2, 3 | 7.8% | 52.3% | 23.3% | 38.4% | 36.5% |
| Full | 3 | −1.3% | 1.2% | 1.6% | −0.3% | 1.4% |
| Regional | All | 7.8% | 66.3% | 16.1% | 35.5% | 34.2% |
| Regional | 2, 3 | 7.8% | 52.4% | 22.8% | 34.9% | 29.3% |
| Solitary | All | 4.5% | 8.8% | 1.6% | 5.13% | 7.4% |

Table 5.3: A summary of the results across all simulations when the rated power at node 3 is lowered to 2/3 of the other power sources. Metrics are shown as the percentage decrease in the respective quantity in the controlled case, relative to the uncontrolled case.

| Model | Controller | $\Delta\|T(s)\|_\infty$ | $\Delta M_p$ | $\Delta\tau_s$ | $\Delta\sigma^2_{peak}$ | $\Delta\int\sigma^2 dt$ |
|---|---|---|---|---|---|---|
| Full | All | 79.6% | 73.7% | 87.7% | 38.7% | 71.8% |
| Full | 2, 3 | 79.6% | 58.4% | 88.0% | 42.9% | 59.7% |
| Full | 3 | 78.0% | 3.0% | 88.5% | 3.0% | 35.1% |
| Regional | All | 79.6% | 72.6% | 86.8% | 39.4% | 57.1% |
| Regional | 2, 3 | 79.6% | 57.9% | 88.1% | 39.2% | 54.2% |
| Solitary | All | 79.5% | 9.5% | 85.4% | 6.6% | 35.4% |

Table 5.4: A summary of the results across all simulations when the rated power at node 3 is lowered to 1/2 that of the other power sources. Metrics are shown as the percentage decrease in the respective quantity in the controlled case, relative to the uncontrolled case.

### 5.6.3 Highlighted Results

After summarizing the results observed from various simulations, it is clarifying to present some specific cases in order to discuss salient features in more detail.

#### 5.6.3.1 Controller Performance vs. Model Complexity

As can be seen in tables 5.2, 5.3 and 5.4, as the model complexity is reduced from 'full' to 'regional' to 'solitary', the controller performance deteriorates. Notably these losses are trivial for controllers synthesized using the 'regional' models, in which the neighboring nodes are modeled. However, further model reduction to the 'solitary' case, where even these neighboring interconnections are not modeled, leads to significant controller losses.

In this section we show the controlled microgrid performance as the model complexity is reduced. As there are three simulated configurations depending on the power capacity of source 3, in order to minimize variable obfuscation we will only be showing configuration 1 in which all sources are identically rated. Similarly, as the goal here is just to show the role of model complexity, we only present the results in which all inverters are controlled with the proposed design.

Figure 5.4 shows the inverter frequencies as they respond to the aforementioned disturbance, for the case where controllers are synthesized with the 'full' model. Figure 5.4 also illustrates the synchronism of the frequency response by mapping the time-varying variance calculated across all inverter frequencies at each timestep. In figure 5.5, these individual frequencies can be seen more clearly.

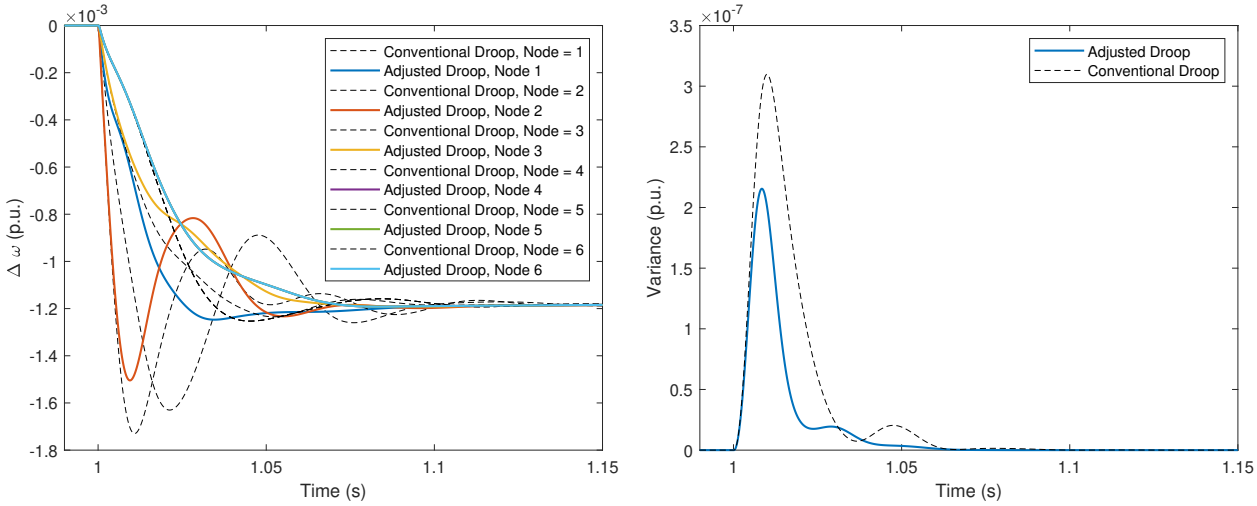


(a) Inverter output frequencies.

(b) Associated variance for inverter frequencies.

Figure 5.4: Inverter output frequencies and associated variance for the full-model control synthesis; all generators are controlled.

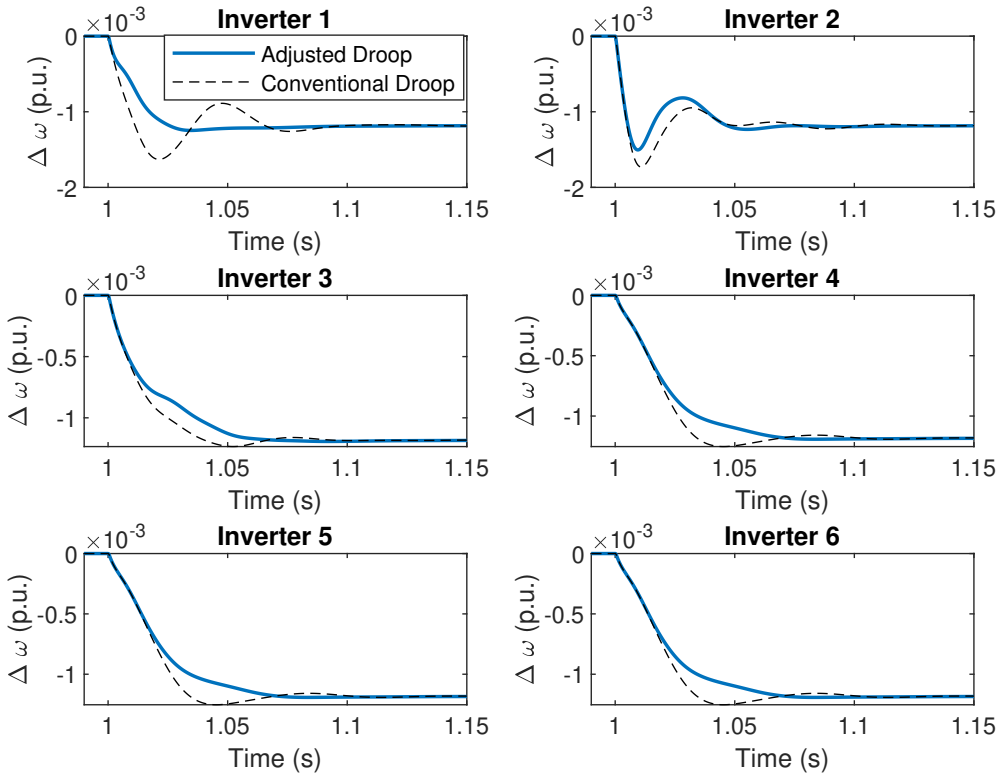


Figure 5.5: Inverter frequency comparisons at each individual node, with and without droop adjustments. Results are for the full-model control synthesis; all generators are controlled

As we first reduce the model complexity to the 'regional' case, we notice that the losses compared to the 'full' controllers are not particularly conspicuous. This response can be seen in figure 5.6. While the settling time is not as reduced, and the overall frequencies are less synchronized, the overall response is comparable. Additionally, the reduction in the infinity-norm is almost unchanged, implying that the reduced model has not significantly changed the robustness of the control.

Taking this a step further, we show the controller performance when the controllers are synthesized with an entirely local model; the controller at node $j$ only knows how its actions affect node $j$, and has no knowledge of other grid components. Unlike the previous case where losses were minimal, here the performance deterioration is significant. The reduction in the infinity norm is more than halved; similarly the undershoot and variance reductions have significantly suffered. This response is shown in figure 5.7.

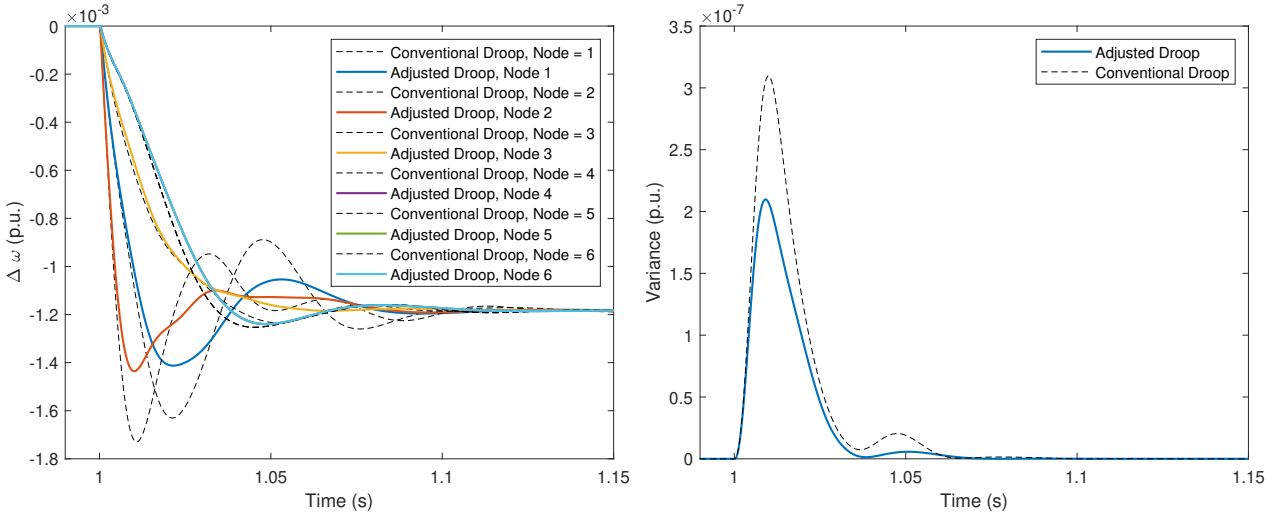


(a) Inverter output frequencies.

(b) Associated variance for inverter frequencies.

Figure 5.6: Inverter output frequencies and associated variance for the regional-model control synthesis; all generators are controlled.

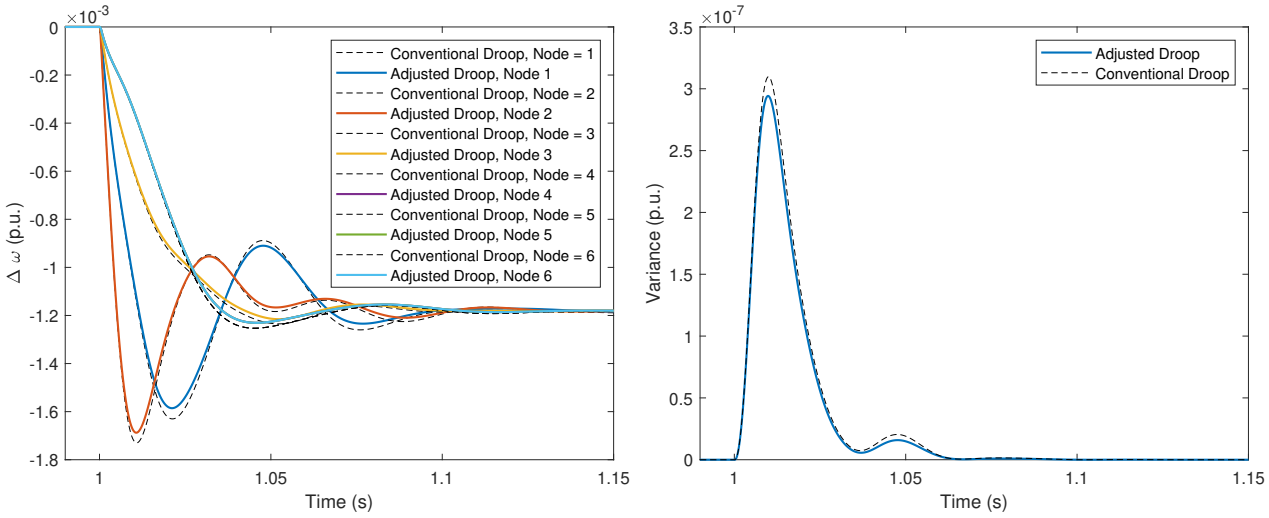


(a) Inverter output frequencies.

(b) Associated variance for inverter frequencies.

Figure 5.7: Inverter output frequencies and associated variance for the solitary-model control synthesis; all generators are controlled.

#### 5.6.3.2 Controller Performance vs. Controller Layout

In this section we show the controlled microgrid performance as the number of controllers is reduced. As there are three simulated configurations depending on the power capacity of source 3, in order to minimize variable obfuscation we will only be showing configuration 1 in which all sources are identically rated. Similarly, as the goal here is just to show the role of controller layout, we only present the results in which the controllers have been synthesized with the 'full' model, and neglect the 'solitary' or 'regional' cases.

As can be seen in tables 5.2, 5.3 and 5.4, the performance appears to be correlated with the controller placement. When the number of controllers is reduced from every inverter being equipped with the proposed controller, to the case where only 2 of the controllers are equipped, to the case where only 1 is equipped, the controlled response suffers.

As with the model complexity, the losses between these configurations are not linear. The best controller performance in all cases is attained when all inverters are controlled; this is intuitive. These plots have already been shown, in figure 5.4.

The losses are insignificant when only inverters 2 and 3 are controlled with the proposed design. This response is shown in figure 5.9, where it can be seen that the overall response is comparable to the case where all inverters were controlled. The infinity norm is unchanged, and the peak variance and peak undershoot are approximately unchanged. The undershoot reduction and the overall synchronism show moderate losses.

Finally when only inverter 3 is controlled with the proposed design, we see significant performance losses. In this case all metrics either show trivial improvements, or even losses compared to the uncontrolled case. This response is shown in figure

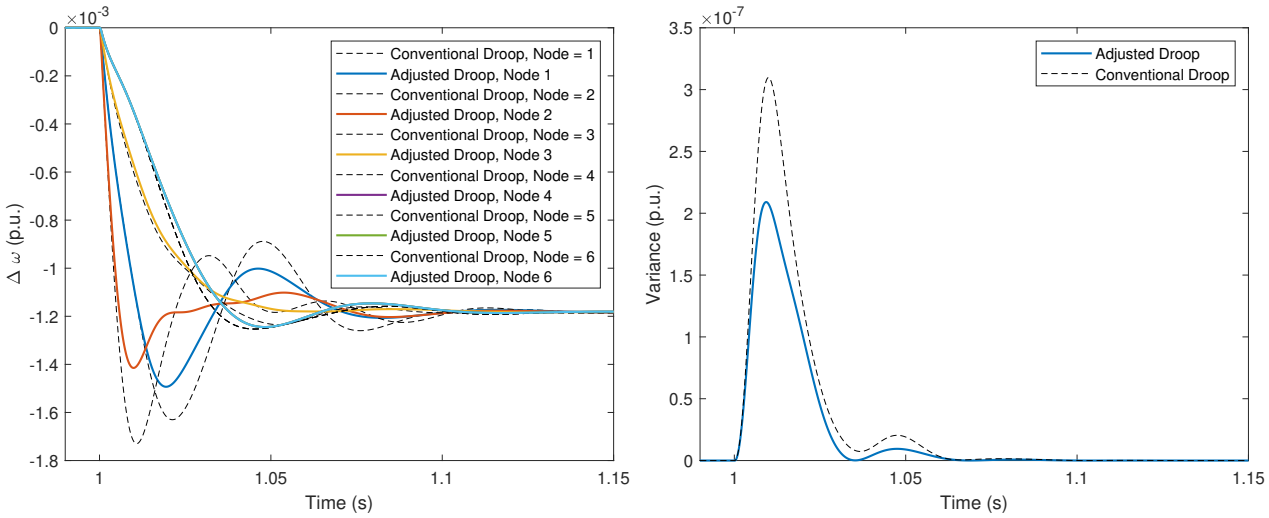


(a) Inverter output frequencies.

(b) Associated variance for inverter frequencies.

Figure 5.8: Inverter output frequencies and associated variance for the full-model control synthesis; only inverters 2 and 3 are controlled.

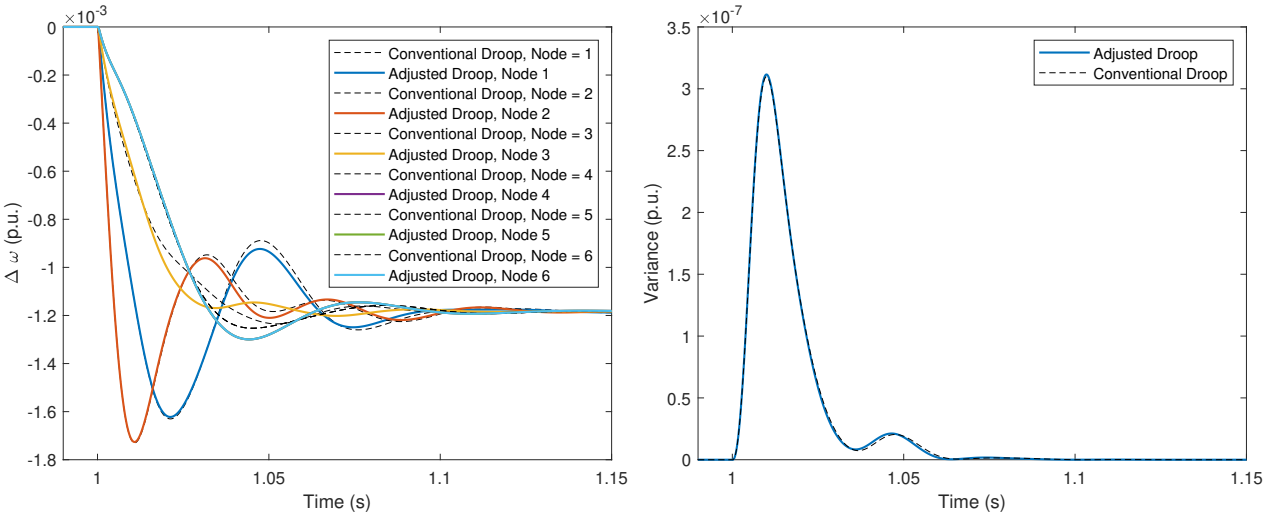


(a) Inverter output frequencies.

(b) Associated variance for inverter frequencies.

Figure 5.9: Inverter output frequencies and associated variance for the full-model control synthesis; only inverter 3 is controlled.

#### 5.6.3.3 Microgrid Stability vs. Droop Gain

In this section we demonstrate that the proposed controller can significantly contribute to the stability of the microgrid, by minimizing the destabilizing effects incurred by the inclusion of a lower-rated power source. To minimize variable obfuscation, we only consider the cases where all inverters are controlled with the proposed design, using the 'full' model for controller synthesis.

As can be seen in tables 5.2, 5.3 and 5.4, as the droop gain at node 3 increases, the controller performance appears to improve. It will now be shown that this is because the droop-controlled microgrid becomes increasingly less stable as this gain is increased. The proposed control design mitigates this destabilizing factor.

The case where all inverters are identically rated is shown in figure 5.10. This can be

compared to figure 5.11., the where the power rating at node 3 is decreased to $\frac{2}{3}$ that of the other power sources. We see that the while these scenarios are similar, there is a notable increase in oscillatory behavior at node 3; other output frequencies have also suffered, but much more subtly. This oscillation is especially conspicuous in figure 5.12, where the power rating at node 3 is decreased to $\frac{1}{2}$ that of the other power sources. Here the oscillation at node 3 is clearly visible, and due to the frequency coupling this has led to observable, but less exaggerated, oscillatory behavior at nodes 4, 5, and 6.

That said, the proposed control design has eliminated this oscillatory transient, especially at node 3. This results in a significantly shorter settling time, in the most extreme case. In this sense the controller has mitigated the destabilizing effects of the weaker power source.

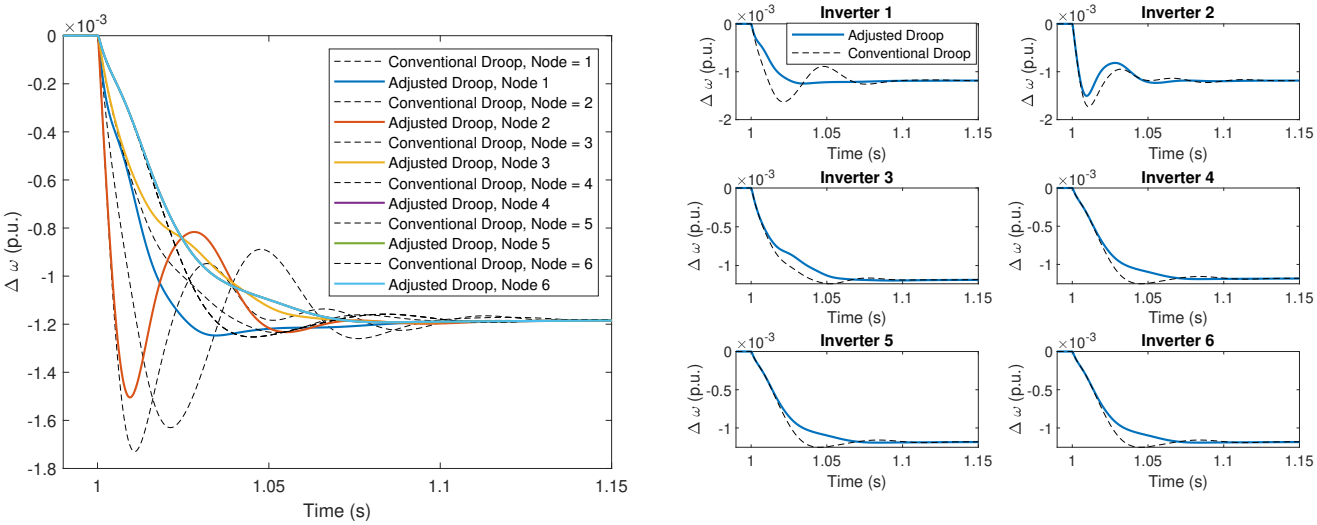


(a) Inverter output frequencies.

(b) Individual frequency comparisons.

Figure 5.10: Inverter output frequencies; all power sources are identical.

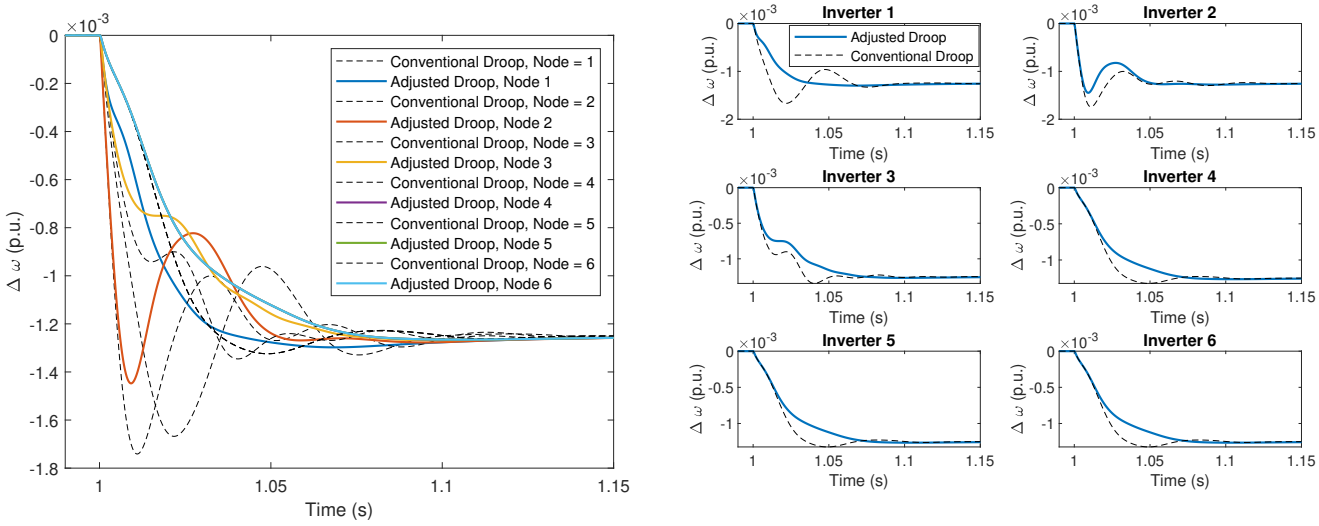


(a) Inverter output frequencies.

(b) Individual frequency comparisons.

Figure 5.11: Inverter output frequencies; the power rating at node 3 has been lowered to $\frac{2}{3}$ that of the other power sources.

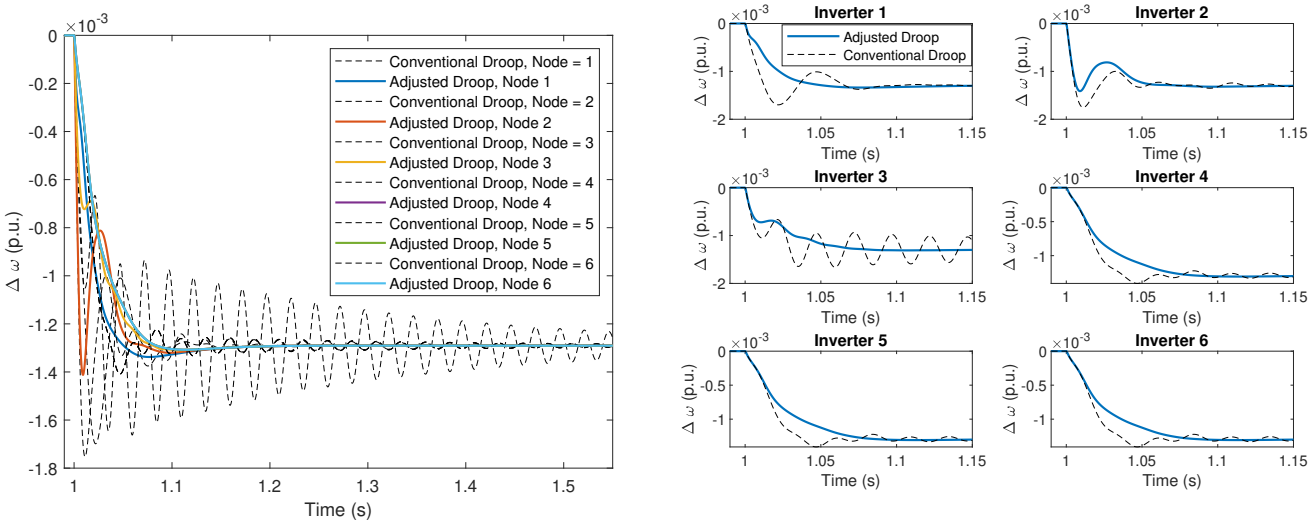


(a) Inverter output frequencies.

(b) Individual frequency comparisons.

Figure 5.12: Inverter output frequencies; the power rating at node 3 has been lowered to $\frac{1}{2}$ that of the other power sources.

## 5.7 Discussion

As previously touched upon, there are three major implications of these results. These results pertain to (1) the degree to which the proposed control design offers stability and robustness improvements; (2) the significance of the model during controller synthesis; (3) the relevance of controller placement for performance gains.

### 5.7.1 Transient Improvements: Stability and Robustness

First it can be seen that the proposed control architecture offers significant improvements in terms of dynamic performance relative to the conventional droop method for inverters: the proposed control design resulted in inverter outputs which settled faster, with fewer

oscillations, and with increased synchronism. Across all comparisons, the 'controlled' cases outperformed the 'uncontrolled' cases, with the exception of the configurations in which only a single droop controller was adjusted with the proposed design. Even the weakest results, observed in the configuration in which all power sources were identically related, showed notable transient improvement upon incorporating the proposed droop adjustment; peak undershoot and settling time were decreased by upwards of 40% and 30% respectively. This improved controlled response also manifested itself in terms of improved synchronism between generators, as quantified by the reduced variance of the output frequencies; the peak variance was reduced by more than 30%, with an integrated variance reduction exceeding 48%.

While these improvements were observed when all power sources were identically rated, the results were even more considerable as the droop gain at even a single inverter was varied. Since this corresponds to the case where a less powerful source is included in the microgrid, this has noteworthy applications for real systems. As a given source becomes weaker, it can be observed that the conventionally controlled microgrid became less stable; the grid responded to the same disturbance with an increasingly oscillatory response. Despite this loss of stability with conventional controllers, the proposed design essentially eliminated the negative changes brought upon the system by this weaker source. Most conspicuously, the oscillatory frequency response at the weaker inverter was controlled to be stable; however the coupled frequency response at the other generators was also improved, as shown in Figure 5.12.

These stability improvements can be interpreted together with the improvement in robustness, as measured by the infinity norm of the microgrid transfer function. The proposed

design resulted in reductions to this norm, implying improved robustness of the closed-loop system. In the case where source 3 was simulated to be weaker than the others, this norm was reduced by more than 78%, even in the worst case in which only a single inverter- the inverter associated with this weaker source- was equipped with the proposed droop adjustment.

### 5.7.2 Impact of Model Type

Second, we can compare results across model type, i.e. controller performance when it was synthesized with a full model that mapped out the full microgrid, a 'regional' model that only mapped its neighboring nodes, and a 'solitary' model that knew nothing of the remainder of the microgrid. These results show that model type had a pronounced effect, but up to a point.

Across all simulations, we can see that as expected, the full model resulted in the best microgrid performance. This was to be expected, as these controllers had the most information regarding the effects actuated by their individual outputs.

However it can be seen that only mild losses were incurred if the controllers were instead synthesized using the regional models. Between these cases, the reductions in infinity norms were typically unchanged, while the settling times and peak undershoots were comparable; the full model did tend to result in improved synchronism, as evidenced by the integrated variance. These losses appeared to be minor, suggesting that the bulk of improvements could be attained using only regional models during controller synthesis.

Alternatively, the simplification of the model eventually resulted in a considerable reduction in performance. The solitary model-types resulted in the worst performance across all simulations, by a considerable margin, yet still showed improvement relative to the con-

ventional droop controllers. Nevertheless these improvements were approximately reduced by an order of magnitude relative to the full and regional model types. The notable exception is in the least stable configuration, configuration 3, in which even the solitary model-type resulted in a significantly more robust system compared to the conventional droop controllers.

### 5.7.3 Role of Controller Topology

Finally, it was observed that controller placement had a notable effect on the resulting microgrid performance. Note that we refer to the adjustment to the droop mechanism as a 'controller,' and so the conventional droop is referred to as 'uncontrolled.'

Generally, the microgrid performed better with more controllers rather than fewer, matching physical intuition. However, judicious placement of controllers may offset these losses. Across all simulations, the microgrid performed best when all inverters were equipped with the proposed controller. However the performance was nearly as good if only two of the six inverters were similarly controlled. In particular, controllers placed at the weaker power source and the inverter at the disturbed node resulted in comparable performance to the case where all inverters were controlled. Again, this reduction eventually showed losses. When only a single inverter was controlled with the proposed design, even the best results were often comparable to the uncontrolled case.

Moreover, in the cases in which one power source was weaker than the others, the convex solver failed to even converge to a solution if the weaker power source was not equipped with the proposed controller. In fact, no suitable feedback matrix could be generated even if all inverters were equipped with the proposed controller *except* the inverter at the weaker source. This suggests that in model-based designs, it may be necessary to include controllers

to handle 'problematic' features of the dynamic system.

We note that these results require further exploration. While it is intuitive that more controllers means better performance, it is a somewhat open question of how many controllers may be needed in a microgrid. If the goal is to limit the number of controllers, then it may be necessary to explore topology-specific configurations to identify where controllers need to be located. That said, in this case the proposed controllers would not require additional sensor data compared to the conventional droop controller; they would simply require that the same sensor measurements be used in a slightly different way. In this sense, it would not be prohibitive to change the droop method to match this proposed design.

## 5.8 Conclusion

We conclude this section by remarking that the proposed control design has shown considerable improvement relative to the conventional droop controller, across multiple transient metrics and robustness criteria. Additionally, the proposed design does not interfere with the steady-state power sharing characteristic that makes droop controllers so attractive, nor does it require any additional sensor data or intercommunication between nodes.

Instead, the proposed design simply requires more 'startup' cost during controller synthesis. Much as droop controllers require tuning in order to set desirable droop gains, the proposed controllers would require a model of the microgrid in order to be synthesized. But as shown, the necessary model for effective control is fairly simple; considerable grid-wide improvements can be attained if the controllers are synthesized with a truncated model of only their neighboring nodes.

With these improvements, the resulting microgrid can be more robust, particularly to power sources of variable strength. This enhances the flexibility of a microgrid, and allows for greater incorporation of distributed energy resources.

# Chapter 6

# Wind Turbine Frequency Support in Microgrids

This section outlines a proposed controller to allow a wind turbine to participate in primary frequency control. The controller draws power from the rotational inertia stored in the rotor of the wind turbine, in order to provide rapid power injections during transient periods [1].

As mentioned earlier, most modern wind turbine generators are decoupled from grid frequency through power electronics, and so the inertia of the turbine's rotor and generator do not contribute to the overall grid inertial response. This exacerbates the challenge of frequency regulation as more conventional units are replaced by wind turbines, and weakens the grid's ability to handle power quality disturbances. To improve the overall competitiveness of wind power, it is therefore necessary for wind turbines to provide control or support during these transient perturbations.

The motivating idea behind this research is that although wind turbines can con-

[1] Results in this section have been published in [71]:

M. Chu Cheong, Z. Ma, H. Qian, J. Conger, P. Du, and D. Chen, "Wind Turbine Participation in Primary Frequency Control," *Journal of Dynamic Systems, Measurement, and Control*, vol. 141, p. 104501, May 2019.

M. Chu Cheong primarily led this work, with joint collaboration from Z. Ma. The responsibilities of Chu Cheong included leading the overall project and design, as well as integrating the proposed control methodology into the system model. H. Qian and J. Conger provided modeling assistance, while P. Du and D. Chen provided advisory input.

tribute to frequency variability, they also possess a significant amount of stored rotational energy in the turbine rotor. The goal of this project was to show that using this physical inertia, a wind turbine can be used to support the network's frequency response by emulating the inertial response of a traditional synchronous generator.

This behavior is facilitated by the power electronics in variable-speed wind turbines, which allow for fast actuation of the generator torque. Because the torque can be rapidly adjusted and commanded, a wind turbine can quickly ramp up its overall power output by drawing power from its heavy, spinning rotor. This allows the wind turbine to potentially provide an inertial frequency response that could be more responsive than that of a traditional generator.

This fundamental idea is not new, but proposed methodologies have been limited or flawed. Generally, the implementation of this idea has resulted in controllers that are either inefficient or not robust. In many cases, the proposed controllers are either efficient but potentially unstable, or operate with guaranteed robustness and stability but waste power in the process. Inefficiency generally results from deloaded controllers, which intentionally capture less power than that which is available, in order to ensure a power reserve. On the other end of the spectrum, there are proposed controllers which seek to maximize power capture and provide support when required, but then fail to account for turbine aerodynamics and may result in turbine instability or critical slowdowns. The goal of this research was to design a controller which could address the shortcomings of these approaches.

In this project, we developed a robust controller for wind turbine operation that allowed the wind turbine to participate in grid frequency control. The resulting controlled turbine was designed to operate in conjunction with a conventional power source, such as a

backup diesel generator. The idea is that these power sources can provide power at different timescales, and using this controller they can complement each other to better support the grid. Wind turbines can inject power quickly, but may not be able to sustain this increased output; slower generators can provide sustained power, but ramp up much more slowly. If these sources are controlled to operate together, the resulting frequency support is shown to result in superior grid performance.

For the proposed controller, the wind turbine was controlled to inject active power proportional to the measured frequency error; if more power was required than what was available from the wind, power was drawn from the rotational energy of the turbine's rotor. To achieve this objective and avoid behavior such as critical slowdowns, wind turbine dynamics were included into the proposed control design in order to ensure stable operation and control of the turbine.

## 6.1 Wind Turbine Model

An NREL 1.5 MW WindPact turbine was simulated for this application. Specifically, this was a doubly-fed induction generator (DFIG) type turbine, in which a wind turbine was coupled with a doubly-fed induction generator to allow for variable-speed operation.

The wind turbine frequency dynamics were modeled with a one-mass model which assumes a rigid base, tower, and shaft:

$$(J_r + G_r^2 J_g)\dot{\omega} = \frac{\pi}{64}\rho_{air} D_r^5 \frac{C_p(\beta, \lambda)}{\lambda^3}\omega^2 - b\omega - G_r T_g, \tag{6.1}$$

with the tip speed ratio, $\lambda$, defined as

$$\lambda = \frac{\omega D_r}{2V_w}. \tag{6.2}$$

In this equation $J_r$ is rotor inertia ($kg/m^2$), $J_g$ is generator inertia ($kg/m^2$), $\omega$ is the turbine's rotor angular velocity (rpm), $\rho_{air}$ is air density ($kg/m^3$), $D_r$ is rotor diameter ($m$), $\beta$ is the blade pitch angle (degrees), $b$ is the frictional loss constant, $G_r$ is the gear ratio, $T_g$ is the generator torque, and $V_w$ is wind speed (m/s). This expression is expressed more concisely by introduction of aerodynamic torque:

$$T_{aero} = \frac{pi}{8\omega}\rho_{air}D_r^2V_w^3C_p, \tag{6.3}$$

such that

$$(J_r + G_r^2J_g)\dot{\omega} = T_{aero} - b\omega - G_rT_g. \tag{6.4}$$

This reformulation was utilized during the controller design process.

The power coefficient, $C_p$ is a measure of the overall efficiency of the wind turbine. $C_p$ is a function of the blade pitch angle $\beta$ and the tip speed ratio $\lambda$, and was computed by NREL's WT-Perf program; this software package uses blade element momentum theory to predict wind turbine performance.

## 6.2 Control Methodology

For this design, the goal was to control power injection on the primary and secondary timescales. As described in previous section, spinning generators demonstrate a linear relationship between active power supply and frequency. This can be simplified for a network of $n_g$ power sources and $n_l$ loads, where the relationship between power and frequency can be expressed by a first-order lag transfer function:

$$\Delta f(s) = \frac{1}{2H_{sys} + D_{sys}}(\sum_{j=1}^{n_g}\Delta P_{g,j}(s) - \sum_{k=1}^{n_l}P_{l,k}(s)). \tag{6.5}$$

In this relationship $H_{sys}$ represents the network's rotational inertia, while $D_{sys}$ represents the damping present in the system. Note that here $f$ is used to represent the network frequency, while $\omega$ is reserved for the wind turbine rotor frequency; these quantities are physically decoupled and are generally not identical.

When overall load does not match overall supply, network frequency deviates from its nominal setpoint. To handle this discrepancy, we can adjust the power outputs from individual generators. These generators do not instantly respond to commanded power signals; the response can also be simplified as a first-order lag function:

$$\Delta P_g = \frac{1}{\tau_{gen} s + 1} \Delta P_{g,cmd}, \tag{6.6}$$

where $P_g$ represents the output power from the generator and $P_{g,cmd}$ represents the commanded power signal to the generator. It can be seen that if $\Delta P_l$ changes, $\Delta P_g$ will lag, resulting in frequency error.

In the proposed control design, a wind turbine is controlled to operate in tandem with a synchronous generator. For the coupled system, the overall change in output power, $\Delta \tilde{P}_g$, can be expressed as:

$$\Delta \tilde{P}_g = \Delta P_{wt} + \frac{1}{\tau_{gen} s + 1} \Delta P_{g,cmd}, \tag{6.7}$$

where $\Delta P_{wt}$ is the controlled change in wind turbine output power. The hypothesis that motivated this design is the idea that the wind turbine can rapidly increase its output power to mitigate the slow response of the traditional generator. However, this increased power output may not be sustainable depending on wind conditions, and so the controller ramps down the wind turbine output as the traditional generator ramps up. The goal of this design

is to more closely track changes in load, which cannot be perfectly forecasted, in order to minimize $\Delta f$ in the system.

The proposed control design depends on controlled modulation of the wind turbine's output power, which in turn depends on wind turbine's generator torque:

$$P_{wt} = T_g G_r \omega. \tag{6.8}$$

This torque can be rapidly actuated in order to draw power from the wind turbine's rotor, as it is directly proportional to the quadrature component of the rotor current:

$$T_g = -\frac{L_m e_t}{L_s + L_m} I_{qr}, \tag{6.9}$$

where $L_m$ is the magnetizing inductance, $L_s$ is the stator leakage inductance, $e_t$ is the terminal voltage of the DFIG, and $I_{qr}$ is the quadrature component of the rotor current in the d-q frame.

$I_r$ can be controlled to meet its commanded value by adjusting the $V_{qr}$, the quadrature component of the controllable rotor voltage. For these purposes, $V_{qr}$ is adjusted using a PI controller:

$$V_{qr}(s) = (K_{pq} + \frac{K_{iq}}{s})(I_{qr,ref}(s) - I_{qr}(s)). \tag{6.10}$$

By modifying $V_{qr}$, the wind turbine torque can therefore be controlled to the desired degree. The $V_{qr}$ response, and thus the torque response, is on the order of milliseconds; this is significantly faster than the rate at which a traditional generator can change its power output.

The proposed control laws for controlled torque generally fall into two main categories, depending on the wind turbine's power output relative to its rated capacity: (1) partial load

operation, and (2) full load operation. At partial load, the wind turbine produces less power than its rating. In this situation, the wind turbine blade pitch angle, $\beta$, is set to its optimal value to maximize energy capture; the wind turbine's generator torque is actuated in order to provide frequency support for the microgrid. Alternatively during full load operation, when the wind turbine power output is at its rated value, then a novel optimal control procedure has been implemented in order to avoid critical overspeeding.

### 6.2.1 Partial Load Operation

Under these conditions, the blade pitch angle is set to its optimal value. Depending on the magnitude of network frequency error, $|\Delta f|$, the torque is commanded to be:

$$T_{g,cmd} = \begin{cases} T_{energy} & |\Delta f| \leq \Delta f_s \\ T_{grid} & |\Delta f| \geq \Delta f_d \\ \frac{|\Delta f| - \Delta f_s}{\Delta f_d - \Delta f_s} T_{grid} + \frac{\Delta f_d - |\Delta f|}{\Delta f_d - \Delta f_s} T_{energy} & \Delta f_s < |\Delta f| < \Delta f_d \end{cases} \tag{6.11}$$

where $T_{energy}$ and $T_{grid}$ are control schemes that apply depending on the grid status.

The control strategy is designed to change depending on the degree to which the grid is disturbed. As the outlined control laws are generally nonlinear, a switched control methodology is adopted to handle these different scenarios. Specifically, if the grid frequency deviation is less than $\Delta f_s$, we have considered the grid to be 'safe' and not in need of wind turbine support, while if the frequency deviation exceeds $\Delta f_d$, we have considered the grid to require support from the wind turbine. $\Delta f_d$ and $\Delta f_s$ are not the same to avoid limit cyclic behavior, where the grid would undesirably oscillate between 'safe' and 'disturbed' behavior. In the interim between these two event-marking thresholds, the designated control laws are linearly interpolated.

In addition to grid conditions, different operating modes are also included in the

design to accommodate various turbine conditions. The control law varies depending on the measured rotor frequency, $\omega$, to ensure stable turbine performance.

If the grid experiences a small frequency deviation, less than $\Delta f_s$, then the goal of controller is simply to track its nominal power setpoint, $P_{wt}^0$ as best as possible. In this situation, the torque is commanded to follow $T_{energy}$, which is defined as

$$T_{energy} = \begin{cases} K_{stc}\omega^2 & \omega \leq (P_{wt}^*/(G_r K_{stc}))^{1/3} \\ \frac{P_{wt}^0}{G_r \omega} & \text{else} \end{cases} \tag{6.12}$$

This scheme ensures that if the nominal power setpoint $P_{wt}^0$ is greater than the available wind power, then the wind turbine will seek to optimize its power capture. If the wind conditions make it possible to meet $P_{wt}^0$, then this setpoint will be tracked.

Alternatively, if the grid undergoes a more significant frequency deviation which exceeds $\Delta f_d$, then the controller switches to a supporting role, as dictated by $T_{grid}$:

$$T_{grid} = \begin{cases} K_{stc}\omega^2 & \omega \leq \omega^* \\ \frac{P_{cmd}}{G_r \omega} & \omega \geq \omega^{opt} \\ \frac{\omega - \omega^*}{\omega^{opt} - \omega^*} \frac{P_{cmd}}{G_r \omega} + \frac{\omega^{opt} - \omega}{\omega^{opt} - \omega^*} K_{stc}\omega^2 & \omega^* < \omega < \omega^{opt} \end{cases} \tag{6.13}$$

$\omega^{opt}$ refers to the optimal rotor speed in terms of energy capture, as determined by

$$\omega^{opt} = \frac{2V_w \lambda^{opt}}{D_r}, \tag{6.14}$$

where $V_w$ is wind speed and $D_r$ is rotor diameter, as before. $\lambda^{opt}$ represents the optimal tip speed ratio, which is fixed for a given wind turbine.

In this control scheme, the controller attempts to track the commanded power until the rotor frequency is too low to safely extract more power. If the rotor speed exceeds its optimal value, then the power output can be easily tracked; wind energy capture increases

as the the turbine rotor slows. As more power is commanded, the wind turbine's output power approaches the captured input wind power, at which point the system would be at a steady-state.

If even more power is commanded, then the turbine frequency decreases and falls below $\omega^{opt}$; in turn, the captured wind power decreases. This can result in instability: in this scenario the turbine is slowing, and as it slows it captures less power, and slows further. To avoid this failure mode, the output power is reduced and the generator torque is shifted to maximize energy capture to allow the turbine frequency to recover.

As with $\Delta f_s$ and $\Delta f_d$, two event marking frequencies are designated here to avoid cyclic switching behavior. $\omega^* < \omega^{opt}$ is a threshold chosen to avoid switching transients between the 'power tracking' and 'turbine recovery' modes.

### 6.2.2 H-2 Gain Scheduled Pitch Control During Full Load Operation

If the wind conditions are such that the available wind power exceeds the commanded wind power, then the turbine is free to operate at its rated speed. In this operating mode, over-speeding is a concern for the wind turbine. Torque modulation alone cannot solve this problem. If torque were to be increased, the turbine could be slowed, but at the cost of tracking error: the output power would increase.

To avoid this issue while still tracking $P_{cmd}$, blade pitch angle $\lambda$ is no longer held fixed. Traditional blade pitch angle controllers apply gain-scheduled pitch control to minimize the deviation between rotor speed and its setpoint under volatile wind flow. However this application requires that the wind turbine must track its commanded reference, and so a simple gain scheduled pitch controller is not optimal and robust enough for this application.

For example, conventional gain-scheduled controllers rely on wind speed measurements and this methodology can be challenged in variable wind conditions; this may not be an issue for normal wind turbine operation, but the wind turbine is being used for specific power injection in this application and so precision is more emphasized.

An H-2 gain scheduled controller was developed in this project in order to more optimally control $\lambda$. Specifically, a PI controller is used to minimize the error between $\omega$ and $\omega_{rated}$:

$$\beta_{cmd} = K_p(\beta, P_{cmd})(\omega - \omega_{rated}) + K_i(\beta, P_{cmd}) \int_{t_0}^{t_f} (\omega - \omega_{rated}) dt. \tag{6.15}$$

$K_p$ and $K_i$ are the scheduled proportional and integral gains; the goal is to optimally choose $K_p$ and $K_i$.

These gains were determined by optimizing a cost function which considers both the error in $\omega$ and the degree of control actuation, the rate of change of the pitch angle $\frac{d\lambda}{dt}$. For a given wind speed disturbance $d(s)$, this cost function can be written as

$$E = W \| \frac{\Delta\omega(s)}{d(s)} \|^2 + \| \frac{s\beta(s)}{d(s)} \|^2, \tag{6.16}$$

where $W$ is the relative importance of minimizing the rotor speed deviation relative to minimizing the pitch rate. The specific norm used for this application is the H-2 norm:

$$E = W \| \frac{\Delta\omega(s)}{d(s)} \|^2 + \| \frac{s\beta(s)}{d(s)} \|^2. \tag{6.17}$$

The two transfer functions in this cost function are obtained by taking the first-order Taylor expansion of equation 6.1, around its rated steady-state where $T_{aero} = G_r T_g = \frac{P_{cmd}}{\omega_{rated}}$.

In this expansion, $T_{aero} = T_{aero}(\beta, \omega, V_w)$, while $T_g = T_g(\omega)$:

$$\begin{aligned} J_d\dot{\omega} =& (T_a) - (G_r T_g) \\ \approx& (T^0_{aero} + \frac{\partial T_{aero}}{\partial \beta}\Delta\beta + \frac{\partial T_{aero}}{\partial \omega}\Delta\omega + \frac{\partial T_{aero}}{\partial V_w}\Delta V_w) - (G_r T^0_g + G_r \frac{\partial T_g}{\partial \omega}\Delta\omega) \\ \approx& (\frac{P_{cmd}}{\omega_{rated}} + \frac{\partial T_{aero}}{\partial \beta}\Delta\beta + \frac{\partial T_{aero}}{\partial \omega}\Delta\omega + \frac{\partial T_{aero}}{\partial V_w}\Delta V_w) - (\frac{P_{cmd}}{\omega_{rated}} - \frac{P_{cmd}}{\omega^2_{rated}}\Delta\omega) \end{aligned} \tag{6.18}$$

In this linearization step, the damping constant $b$ is neglected as it generally has a negligible effect upon the system. Furthermore, $\frac{\partial T_{aero}}{\partial \omega}\Delta\omega$ is dominated by the remainder of the equation, and so this linearization can be simplified to:

$$J_d\Delta\dot{\omega} = \frac{\partial T_{aero}}{\partial \beta}\Delta\beta + \frac{\partial T_{aero}}{\partial V_w}\Delta V_w + \frac{P_{cmd}}{\omega^2_{rated}}\Delta\omega. \tag{6.19}$$

Labeling the disturbance due to wind speed variations:

$$d(s) := \frac{\partial T_{aero}}{\partial V_w}\Delta V_w, \tag{6.20}$$

then we can rewrite the Taylor expansion using equation 6.15

$$\begin{aligned} J_d\dot{\omega} - \frac{\partial T^0_{aero}}{\partial \beta}\Delta\beta - \frac{P_{cmd}}{\omega^2_{rated}}\Delta\omega =& d \\ J_d\dot{\omega} - (\frac{\partial T^0_{aero}}{\partial \beta}K_p + \frac{P_{cmd}}{\omega^2_{rated}})\Delta\omega - \frac{\partial T^0_{aero}}{\partial \beta}K_i \int \Delta\omega dt =& d, \end{aligned} \tag{6.21}$$

where this partial derivative $\frac{\partial T^0_{aero}}{\partial \beta}$ can be computed for all equilibrium pitch angles $\beta_{rated}$

$$\frac{\partial T^0_{aero}}{\partial \beta} = \frac{\pi}{8\omega_{rated}}\rho_{air} D_r^2 V^3_{w,0}\frac{\partial C_p}{\partial \beta}. \tag{6.22}$$

This can be written in the frequency domain as

$$\frac{\Delta\omega(s)}{d(s)} = \frac{s/J_d}{s^2 + c_1 s + c_2}, \tag{6.23}$$

where

$$\begin{aligned} c_1 &= -\frac{1}{J_d}\left(\frac{\partial T^0_{aero}}{\partial \beta}K_p + \frac{P_{cmd}}{\omega^2_{rated}}\right) \\ c_2 &= -\frac{1}{J_d}\left(\frac{\partial T^0_{aero}}{\partial \beta}K_i\right). \end{aligned} \tag{6.24}$$

Equation 6.15 can be used to relate $\beta(s)$ to $\omega(s)$ and write this transfer function in terms of the pitch rate, $s\beta(s)$:

$$\frac{s\beta(s)}{d(s)} = -\frac{1}{\frac{\partial T^0_{aero}}{\partial \beta}}\frac{(c_1 + \frac{P_{cmd}}{J_d\omega^2_{rated}})s^2 + c_2 s}{s^2 + c_1 s + c_2}. \tag{6.25}$$

To minimize the cost function $E$ in equation 6.17, the H-2 norms of equations 6.23 and 6.25 were computed. For a transfer function, $\hat{G}(s)$, with realization

$$\begin{aligned} \dot{x} &= Ax + Bu \\ y &= Cx \end{aligned} \tag{6.26}$$

the H-2 norm can be found as

$$\|\hat{G}\|^2_{H2} = \text{trace}(CQC^T), \tag{6.27}$$

where $Q$ is the solution to the Lyapunov equation:

$$AQ + QA^T + BB^T = 0. \tag{6.28}$$

Both 6.23 and 6.25 are second-order transfer functions, and so the cost function $E$ can be computed analytically as

$$E = \frac{W}{2J_d^2 c_1} + \frac{c_2(c_1 + \frac{P_{cmd}}{J_d\omega^2_{rated}})^2 + (c_2 - c_1(c_1 + \frac{P_{cmd}}{J_d\omega^2_{rated}}))^2}{2c_1(\partial T_{aero}/\partial\beta)^2}. \tag{6.29}$$

$c_1$ and $c_2$ can be computed such that $E$ is minimized by solving $\frac{\partial E}{\partial c_1} = \frac{\partial E}{\partial c_2} = 0$ for $c_1$ and $c_2$. The global minimum solution results in the pair of equations:

$$\begin{aligned}(9c_1^2 - 2c_1\frac{P_{cmd}}{J_d\omega_{rated}^2} + (\frac{P_{cmd}}{J_d\omega_{rated}^2})^2)(c_1 + \frac{P_{cmd}}{J_d\omega_{rated}^2})^2 &= \frac{4W}{J_d^2}(\frac{\partial T_{aero}}{\partial \beta})^2 \\ c_2 &= \frac{1}{2}(c_1^2 - (\frac{P_{cmd}}{J_d\omega_{rated}^2})^2).\end{aligned} \tag{6.30}$$

Using the relations in equation 6.24, the optimal PI gains are given as

$$\begin{aligned}K_p(\beta, P_{cmd}) &= - J_d(\frac{\partial T_{aero}}{\partial \beta})^{-1}(c_1 + \frac{P_{cmd}}{J_d\omega_{rated}^2}) \\ K_i(\beta, P_{cmd}) &= - c_2 J_d(\frac{\partial T_{aero}}{\partial \beta})^{-1}.\end{aligned} \tag{6.31}$$

The resulting gains are independent of wind-speed measurements, and so the controller is more robust to variable wind conditions and more reliable for the desired application.

## 6.3 Results

The controller was tested against simulated wind conditions in a 4-node 60 MW microgrid. It was observed that the proposed design was able to effectively reduce the peak frequency deviation; relative to the new steady-state, frequency overshoot was reduced by as much as 44%. Moreover, the design was shown to be effective in both deloaded and undeloaded conditions, demonstrating the flexibility and efficiency of the controller.

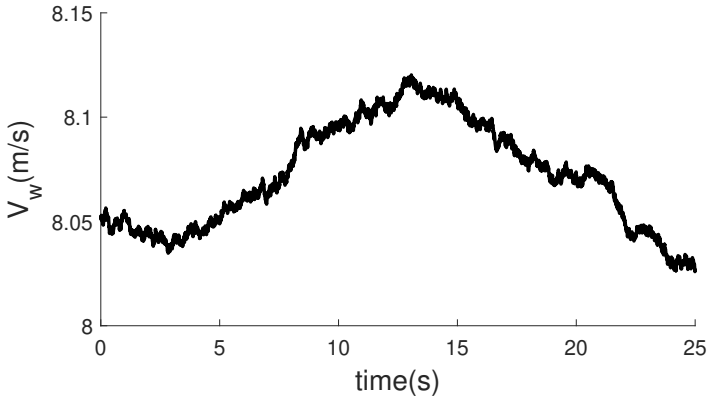


Figure 6.1: Wind speed profile used for testing the proposed control design.

The simulated microgrid was modeled as an interconnection of 4 separate subsystems. Each subsystem was comprised of a load and a generator, with the exception of subsystem 2 which also included a wind turbine. In the simulated microgrid, each generator is is assumed to be identically rated. At steady-state, the active power contributions of each subsystem (i.e. from the generator and possibly the wind turbine) were approximately 15 MW.

After 1 second, a sudden load increase of 3 MW is simulated via a step change in the power draw at subsystem 4; this represented a 5 % increase in total active power load. This in turn triggers an under-frequency event in the microgrid.

To test the ability of the proposed controller to respond to this frequency deviation, we considered a wind profile with a time resolution of 2 ms and a mean value of approximately 8 m/s. The wind-speed time history can be seen in Figure 6.1.

Three separate cases were explored. In the first 'no support' case, the wind turbine did not provide frequency support, and simply tracked its nominal power output setpoint of 0.6 MW. In the second 'undeloaded' case, the wind turbine contributed to frequency control.

As before, the nominal power output setpoint was 0.6 MW, but notably this is close to the maximum available wind power given the wind speed conditions; as a result, the wind turbine cannot capture more power to counteract a frequency disturbance. In the third 'deloaded' case, the wind turbine also contributed to frequency control, but with a nominal power setpoint of 0.3 MW. During this deloaded case, there was more available wind power than was captured, but as a result the wind turbine operated near its rated rotor speed; overspeeding was therefore a concern and was addressed by the blade pitch angle controller.

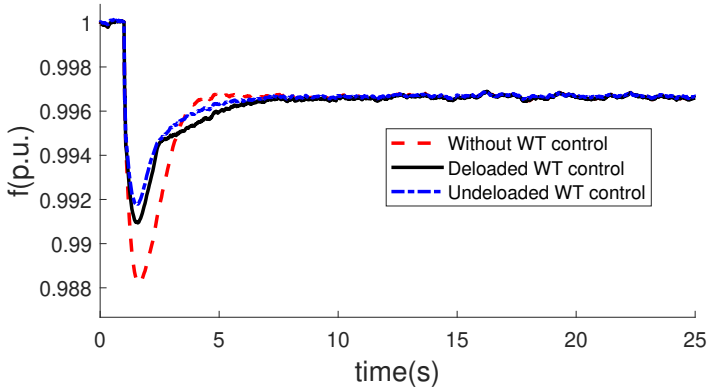


Figure 6.2: Microgrid frequency deviation with varying levels of support from the wind turbine

With a change in load at time $t = 1s$, the grid frequency is expected to drop. This grid behavior is shown in Figure 6.2.

The main question was simply this: how well did this controller mitigate frequency deviations? As can be shown in 6.2, the effects of the proposed controllers can most notably be seen during the immediate transient period following the grid disturbance. The wind turbine controllers allowed the system to respond more rapidly during the ramping-up period

of the conventional generators. As a result, the peak frequency undershoot was curtailed due to these controllers, while the final steady-state frequencies were approximately the same in all cases. In the per-unit basis (p.u.), the final steady-state frequency was approximately 0.997. In the 'no support' case, the peak frequency error occurred at 0.9883 p.u., compared to 0.9911 p.u. in the undeloaded case and 0.9919 p.u. in the deloaded case.

Given the nature of proportional control, some degree of steady-state error is to be expected in response to a sustained load variation. Therefore the frequency undershoot was compared to the final approximate steady-state frequency value. With this benchmark, the frequency undershoot was reduced by 34.7% in the undeloaded case, and 43.4% in the deloaded case- a noteworthy reduction.

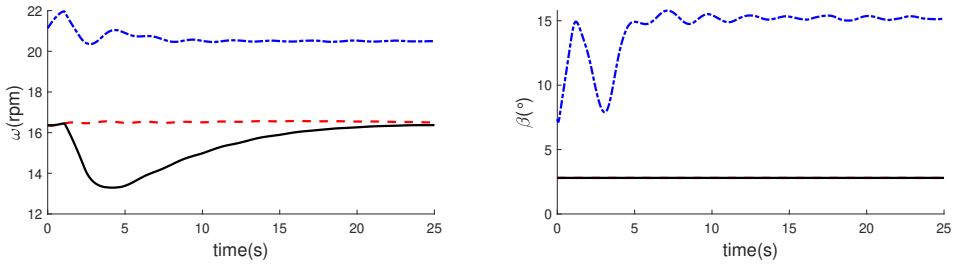


Figure 6.3: Performance comparison with respect to wind turbine characteristics, illustrating rotor frequency (RPM) and blade pitch angle.

As earlier emphasized, a key point of focus in this research was not only on the grid behavior, but also on the status of the wind turbine insofar as its stability was concerned. To this end, rotor frequency $\omega$ and blade pitch angle $\beta$ are shown in Figure 6.3. As expected, the 'no support' case shows approximately no variation in rotor speed and no change in blade pitch angle during the simulation. In both the deloaded and undeloaded case with wind turbine support, the rotor speed dropped in order to allow the wind turbine to inject active

power into the system. However the deloaded case showed a much smaller rotor slowdown; as the nominal power setpoint was significantly lower than the available wind power, the deloaded case was able to increase its power output without slowing down as severely. The blade pitch angle controller was only active during the deloaded case. In this scenario, the wind turbine was operating near its rated rotor speed because less power was sent to the microgrid.

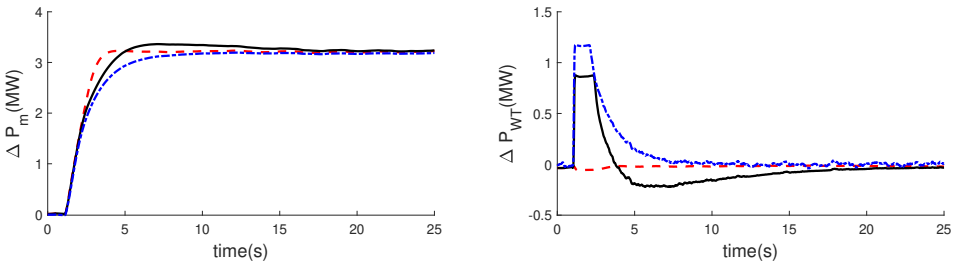


Figure 6.4: Power injections from the wind turbine and associated diesel generator. While the sum power contribution is the same across individual cases, the proportion provided by the wind turbine varies.

To better illustrate the behavior of the power injected to the grid, the power contributions from the wind turbine and diesel generator at subsystem 2 can be seen in Figure 6.4. This makes it clear that the wind turbine provides support during the transient period while the diesel generator ramps up. Additionally, this figure highlights a key difference between deloaded and undeloaded control, which is the recovery period following power injection from the wind turbine. As can be seen in Figure 6.4, following the large power injection between 1 and 4 seconds, the undeloaded wind turbine provides less power than its nominal setpoint. This is consistent with the rotor speed data in Figure 6.3, where the undeloaded control has resulted in a moderately slowed wind turbine. In order to recover to its nominal operating

point, the wind turbine is designed to shunt some power to its rotor in order to speed back up. This was not an issue in the undeloaded scenario, where it was not necessary for the rotor to slow down as significantly in order to provide frequency support to the grid.

## 6.4 Discussion

This research resulted in a controller for a wind turbine for primary frequency control. This represented an improvement over similar wind turbine inertial controllers that have been proposed in the literature, in that it was able to operate in both deloaded and undeloaded conditions and considered wind turbine dynamics to avoid unstable turbine modes.

In addition, a novel optimal blade pitch angle controller was developed using H-2 methods, in order to avoid wind turbine overspeeding during full-load operation. Not only did this optimize the blade pitch control, but it resulted in a controller that did not require error-prone real-time wind speed measurements.

The proposed controller demonstrated smooth control actions during the transitions between normal operation and frequency deviation events. The controlled system showed that the control design effectively improved grid stability by reducing the frequency deviation and recovery time.

# Chapter 7

# Decentralized Estimation for Model-Based Control

## 7.1 Overview

In this chapter we outline and propose a method for decentralized estimation in microgrids. The previous chapter presented a coordinated control design for a wind turbine to provide frequency support to a microgrid. However this application highlights a problem with regards to information sharing. Coordinated control either requires that the individual sources have knowledge of each other; in a microgrid with real-time communication constraints, this is a significant limiting factor. In some cases it may be sufficient to assume that the coordinated sources are directly coupled, and are able to freely share information, but this is a notable design constraint. This motivates the idea that 'remote' state information is necessary, thus presenting the need for decentralized estimation.

In this proposed design, we make use of the concept that local information provides insight into grid-wide behavior. Specifically, frequencies in a stable power network are synchronized:

$$\lim_{t\to\infty} \omega_i = \omega_j, \tag{7.1}$$

where $\omega_i$ and $\omega_j$ refer to the frequencies of individual generators, $i$ and $j$. The main idea is that we can then use this synchronization in order to approximate a remote measurement. This in turn can be used in conjunction with the microgrid model to allow for more accurate

and rapid state estimation compared to the case where we assume that we simply have no information regarding remote states.

For a conventional state estimator, the challenge is that we have potentially noise-polluted sensor measurements that provide information about a subset of the state, but we would like more complete and accurate state information [49, 48]. This problem can be addressed by using the sensor measurements in conjunction with a model of the system dynamics to estimate the propagation of unknown states.

In the decentralized case, the challenge is that the available local sensor information generally does not provide meaningful data about the remainder of the state. As a result, attempts to estimate full state information with this local sensor data may result in excessively slow or potentially unstable estimators, which would be useless for meaningful applications.

For the microgrid, we take advantage of a physical feature unique to power systems in order to leverage local data such that it can be used to estimate grid-wide states. Microgrids, and power systems in general, are commonly powered by some combination of synchronous generation or droop-controlled inverter-interfaced sources. In both of these cases, frequency and active power are strongly coupled across power sources due to the frequency synchronization in a power system. As a result, we will show that local frequency and active power measurements can be used to improve the estimate of remote nodes in a microgrid.

## 7.2 Estimator Construction

A typical linear model may be generally described as

$$\begin{aligned} \dot{x} &= Ax + Bu + Gw \\ y &= Cx + Du + h, \end{aligned} \tag{7.2}$$

where $x$ is the modeled state, $y$ is the set of measurements from the system, $u$ is the control input, $w$ is the disturbance or perturbation to the system, and $h$ is the disturbance to the measurement. For this application, the linear model is as described in chapter 6.

When parts of the state are unknown, a state observer may be used for estimation. The purpose of this estimator is to use the known measurements, combined with a model of the system, to get a better idea or estimate of the unknown parts of the state. We define the observer as $\hat{x}$, with some observer gain matrix $L$ such that

$$\begin{aligned} \dot{\hat{x}} &= A\hat{x} + B_u u + L(y - \hat{y}) \\ \hat{y} &= C\hat{x} + Du. \end{aligned} \tag{7.3}$$

A stable estimator is only possible if the system is at least detectable; the unstable modes of the system must be measurable in some sense [48]. If the system is detectable, then an estimator can be found such that the error propagates as

$$\begin{aligned} e &= x - \hat{x} \\ \dot{e} &= (A - LC)e + Gw - Lh. \end{aligned} \tag{7.4}$$

The challenge is then choosing $L$ such that $A - LC$ is Hurwitz, so that the estimator error converges to 0. Various methods exist for the selection of $L$, either through explicit pole placement techniques or via optimization to minimize uncertainty as in the case of the Kalman filter [49].

That said, the detectability standard is not particularly powerful in the context of decentralized systems. For the case of a microgrid linearized around a stable equilibrium, the system may not have any dynamically unstable modes that diverge, and so any local measurement may result in a detectable system. However that does not mean that any local measurements will necessarily contribute meaningful updates to the full estimated state,

which would in turn allow for faster or more optimal estimation. More importantly, intrinsic model inaccuracies can lead to estimator drift without sufficient sensor data. Intuitively this is reasonable; for something like a vehicular control problem, we would expect that an acceleration measurement would result in a good estimate of velocity, but for microgrid control, a local current measurement does not necessarily provide substantial information about the state of a network bus several kilometers away.

In this design, the key idea is that the frequency is synchronized for all generators and droop-controlled inverters in a microgrid; even if the frequencies go somewhat out of phase during transient disturbances, they settle to a common equilibrium. The goal is to leverage this synchronization so that a local frequency measurement can be used as a proxy for other frequencies throughout the network. Knowing the frequency at a remote node, for example, would allow for meaningful or at least improved state estimation at that node.

Consider the node from which we have real-time measurements; we can consider this node 1, without loss of generality. We have an actual measurement of frequency at node 1, $\omega_1$. Therefore for our pseudo-measurement of node $j$, we have

$$y_j = \omega_1 = y_1. \tag{7.5}$$

This can be interpreted as

$$\begin{aligned} y_j &= \omega_j + h_j(t), \\ &= Cx_j + h_j(t). \end{aligned} \tag{7.6}$$

where $h_j(t)$ represents the transient difference between $y_j$ and $y_1$. As the generators are kept in phase with each other by local droop controllers and the physics of synchronous generation, we know that

$$\lim_{t\to\infty} h(t) = 0. \tag{7.7}$$

Specifically, we expect $h(t)$ to settle on the order of seconds, as this is the primary timescale range in power systems. Ideally we would then use $y_j$ to estimate $x_j$.

## 7.3 Disturbance Reconstruction and Measurement Error

A challenge with state estimation is dealing with the measurement error, $h$, and plant disturbances, $w$. The guiding principle behind the well-known Kalman filter is to assume that these disturbances are zero-mean and Gaussian; under these conditions the filter provides the best possible estimate for a linear system [49]. In this case, our disturbances do not fit this description, and so this section outlines how these disturbances are modeled and handled by the proposed estimator. The goal is to outline a means by which the filter can be implemented.

In the case of measurement signals, $y$, the errors $h$ are due to the transient period during which individual frequencies are asynchronous. Meanwhile the plant disturbances, $w$, represent changes in real power demand/supply. Neither of these are Gaussian, and while $h$ decays to 0, $w$ is certainly not zero-mean. That said, the proposed hypothesis is that these unconventional errors can still be leveraged towards effective state estimation. We will now formalize this measurement and estimation process.

As described, the relevant disturbances to the microgrid are not zero-mean. Accordingly they cannot be neglected when considering estimator stability, as in canonical formulations of state estimators. The estimator described in equation 7.4 is stable provided the matrix $A - LC$ is Hurwitz, which means that the estimate will not diverge from the true state. However if $h$ and $w$ are not zero-mean, then the estimate will exhibit steady-state errors relative to its actual value. In typical modeling and estimation problems, distur-

bances are often safely modeled as zero-mean and Gaussian. This approach is effective for sensor-noise problems, but less so when dealing with power demand surges; power imbalances may be zero-mean over long timescales, but are decidedly not zero-mean at the rapid, primary timescale where they may appear more like step disturbances. Therefore in order for this methodology to have useful applications in microgrids, it is necessary to handle these disturbances in more detail.

The challenge of non-zero mean disturbances could be resolved if the disturbance, $w$, were perfectly known to the estimator. In that case, we would have feedforward compensation of $w$ in the form of

$$\dot{\hat{x}} = A\hat{x} + Bu + Gw + L(y - \hat{y}), \tag{7.8}$$

where the estimator can perfectly account for the disturbance and thus better track the state propagation. But this is not a realistic approach; it requires knowledge of an unknown disturbance.

To deal with this issue, we first restrict this problem to the case where $w$ represents the class of real power disturbances to the network, in order to again take advantage of the fact that synchronous/droop-controlled generators proportionally share the real power load. This subset of problems represents the bulk of load challenges expected in a microgrid, where we are concerned with matching real power demand and supply.

At equilibrium, a network of $n$ droop-controlled inverters will share the total change in real power load in the network $\Delta P_{tot}$ proportional to their droop gains $m_i$ such that

$$m_1 \Delta P_1 = m_2 \Delta P_2 = \cdots = m_n \Delta P_n \tag{7.9}$$

where

$$\sum_{i=1}^{N} \Delta P_i = \Delta P_{tot}. \tag{7.10}$$

An approximation of the real power load can therefore be computed from a measurement of the local load at node $i$, $P_i$, as

$$\Delta P_{tot} = \Delta P_i(\frac{m_i}{m_1} + \frac{m_i}{m_2} + \cdots + \frac{m_i}{m_n}). \tag{7.11}$$

The obvious limitation is that this equality does not hold during the system transients. However the proposal is that this is a sufficient approximation such that the estimator may be useful for control purposes, particularly if the controller is sufficiently robust.

The second challenge associated with this unknown disturbance, $w$, is that the 'location' of the disturbance within the grid is also unknown. By this we mean that there may be a power imbalance event at any individual node, or some combination of imbalances across multiple nodes, but this distinction cannot be readily ascertained without some sort of inter-network communication. Consider that $w$ is in general a $n \times 1$ vector such that

$$w = [w_1, w_2, \ldots, w_n]^T \tag{7.12}$$

where $w_i$ represents the real power imbalance at node $i$, as would be expected from a sudden change in demand. Suppose we reconstruct the disturbance as described, such that our estimated disturbance $\hat{w}$ satisfies

$$\sum_{i=1}^{n} \hat{w}_i = \Delta P_{tot}. \tag{7.13}$$

. Without information exchange between multiple measurement points, a local measurement cannot sufficiently differentiate to ensure that $w_i = \hat{w}_i$. Even if the total power imbalance can be correctly estimated, we may expect the system to respond differently if the source of

the load imbalance is distributed evenly across the microgrid, compared to the case where it is entirely localized at a particular node.

This issue cannot be solved using decentralized information; without communication from other nodes, standard techniques are not sufficient to identify the source of the disturbance within the grid. That said, it may not be necessary to perfectly resolve this issue. The main challenge associated with the unknown disturbances, $w$, is that when $w$ is not zero-mean, the estimate has steady-state errors. For our applications, we therefore are interested in reducing the effect of this steady-state estimation error. If the total load can be reasonably approximated, then the steady-state error may be sufficiently mitigated. In this case, our error dynamics propagate as

$$\dot{e} = (A - LC)e + G(w - \hat{w}) - Lh. \tag{7.14}$$

In this formulation, we see that the estimator sees a zero-mean perturbation along the plant disturbance channel. If we consider

$$\tilde{w} = w - \hat{w} = [w_1 - \hat{w}_1, w_2 - \hat{w}_2, \ldots, w_n - \hat{w}_n]^T, \tag{7.15}$$

then because

$$\sum_{i=1}^{n} \hat{w}_i = \sum_{i=1}^{n} w_i, \tag{7.16}$$

on average $\tilde{w}$ is zero mean. As a result, we would then eliminate the issue of steady-state offset error with the estimator.

As a function of the local state, $x_1$, this may be written as

$$\hat{w} = \begin{bmatrix} \hat{C}_{p1} & 0 & \ldots & 0 \\ \hat{C}_{p2} & 0 & \ldots & 0 \\ \vdots & & & \\ \hat{C}_{pn} & 0 & \ldots & 0 \end{bmatrix} \begin{bmatrix} x_1 \\ x_2 \\ \vdots \\ x_n \end{bmatrix} = \hat{C}_p x, \tag{7.17}$$

where $\hat{C}_{pj}$ is the matrix to measure the active power load at node 1, and then scale it proportionally to the droop gain at node $j$:

$$\hat{C}_{pj}x_1 = (\Delta P_1)\frac{m_1}{m_j}. \tag{7.18}$$

This may be taken a step further, if the location of the disturbance is known *a priori*. Such a situation may be realistic if the configuration of the microgrid is such that there is a particular region whose demand is expected to vary, or if information can be sent to the controller regarding an expected maintenance or disturbance issue. In this case, instead of simply the sum of estimated disturbances matching the total grid disturbance, we can design the estimated disturbance such that the individual channels match more closely.

For example, if it is known that the disturbance is localized at node $k$, then $\hat{w}_j = 0$, for $j \neq k$:

$$\hat{w} = [0, 0, \ldots, 0, \hat{w}_k, 0, \ldots, 0]^T. \tag{7.19}$$

This can be represented as

$$\hat{w} = \begin{bmatrix} 0 & 0 & \ldots & 0 \\ \vdots & & & \\ 0 & 0 & \ldots & 0 \\ \sum_{i=1}^{n} \hat{C}_{pi} & 0 & \ldots & 0 \\ 0 & 0 & \ldots & 0 \\ \vdots & & & \\ 0 & 0 & \ldots & 0 \end{bmatrix} \begin{bmatrix} x_1 \\ \vdots \\ 0 \\ x_k \\ 0 \\ \vdots \\ x_n \end{bmatrix} = \hat{C}_p x, \tag{7.20}$$

**Note: Power Filtering** Instead of explicitly measuring the local load, and extrapolating this measurement to be representative of the grid-wide load, we take a filtered version of this measurement. This mitigates some of the overshoot associated with the power

measurement. For this application, a simple first-order lag filter is applied to the power measurement:

$$\frac{d}{dt}P_{filt} = \frac{1}{\tau_f}(P_{inst} - P_{filt}). \tag{7.21}$$

The filter time constant, $\tau_f$, is tuned experimentally. An example of the load reconstruction is shown in figure 7.1, in which the reconstructed load is compared to the true load; the unfiltered reconstruction better captures the initial growth of the step disturbance, but the filtered reconstruction reduces the overshoot without increasing the settling time.

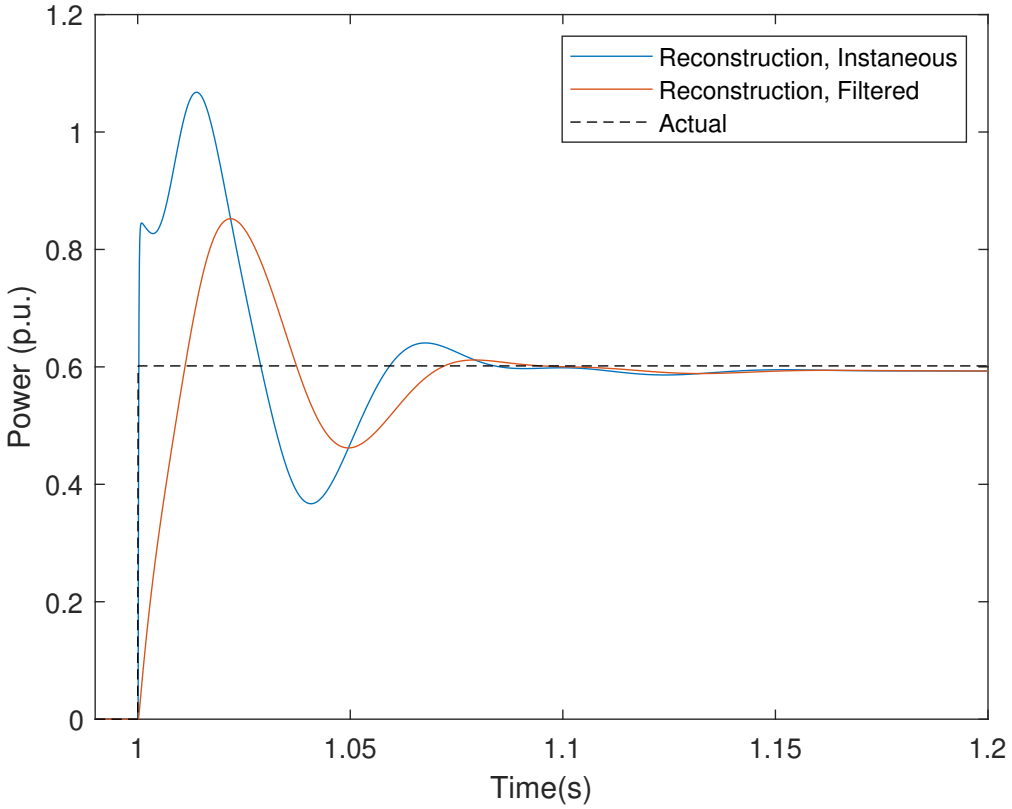


Figure 7.1: Comparison of reconstructed load, using instantaneous local measurements with and without a filter.

### 7.3.1 Estimator Synthesis

Now equipped to address system disturbances, we can model the proposed estimator design as a whole:

$$\begin{aligned} \frac{d}{dt}\begin{bmatrix} x \\ \hat{x} \end{bmatrix} &= \begin{bmatrix} A & 0 \\ LC_y + B_w\hat{C}_p & A - L\hat{C}_y \end{bmatrix}\begin{bmatrix} x \\ \hat{x} \end{bmatrix} + \begin{bmatrix} B_w \\ 0 \end{bmatrix} w + \begin{bmatrix} 0 \\ L \end{bmatrix} h \\ \begin{bmatrix} y \\ \hat{y} \end{bmatrix} &= \begin{bmatrix} C_y & 0 \\ 0 & \hat{C}_y \end{bmatrix}\begin{bmatrix} x \\ \hat{x} \end{bmatrix} + \begin{bmatrix} h \\ 0 \end{bmatrix}, \end{aligned} \tag{7.22}$$

where $h$ represents sensor error. Note that here we have distinguished between $C_y$ and $\hat{C}_y$. $C_y$ is the measurement matrix of the 'real' state, $x$, but it makes the pseudo-measurement approximation where local frequency measurements are taken as pseudo-measurements of remote frequencies. Alternatively, $\hat{C}_y$ measures the 'remote' estimator variables exactly, instead of taking local measurements as a proxy, as there are no constraints on what can be measured from the estimated state. This can be written as

$$\begin{aligned} C_y x &= [\omega_1, \omega_1, \ldots, \omega_1]^T, \\ \hat{C}_y \hat{x} &= [\hat{\omega}_1, \hat{\omega}_2, \ldots, \hat{\omega}_n]^T \end{aligned} \tag{7.23}$$

The estimator gain, $L$, can be designed in a variety of ways. For this application, we treat the issue as a Kalman filtering problem as described previously. The Kalman filter can offer optimal state estimation, provided that conditions are met: when the plant disturbances and sensor errors are zero-mean and Gaussian, then the Kalman filter state estimate minimizes estimation error [49]. However, even if these errors are not Gaussian, the Kalman filter still provides the best linear unbiased estimate . The errors under consideration for this problem are neither zero-mean nor are they Gaussian, but as shown, they can be manipulated such that they are potentially applicable to this problem. For a more complete reference regarding the background and synthesis of the Kalman filter, we refer the reader

to [49, 47]; the contribution of this section is instead focused on the implementation of such filter techniques, rather than the proofs that guarantee their optimality.

In order to synthesize $L$, we need some information regarding the uncertainty of our disturbances $w$ and $h$. For this problem, we have already outlined that as our disturbance is not zero-mean, we have taken steps to approximate $w$ with $\hat{w}$. Therefore typically we would be interested in

$$\begin{aligned} Q &= E[(w - \bar{w})(w - \bar{w})^T] \\ R &= E[(h - \bar{h})(h - \bar{h})^T], \end{aligned} \tag{7.24}$$

where $\bar{w}, \bar{h}$ represent the average value of these quantities. However in this problem we are interested in looking at the variance of the zero-mean equivalents:

$$\begin{aligned} Q &= E[(\tilde{w} - \bar{\tilde{w}})(\tilde{w} - \bar{\tilde{w}})^T] \\ R &= E[(h - \bar{h})(h - \bar{h})^T]. \end{aligned} \tag{7.25}$$

As has been described, $\tilde{w} = w - \hat{w}$ can be taken as zero-mean provided that the disturbance is an active power disturbance. The measurement error $h$ is not explicitly zero-mean, but decays to zero due to the convergence of the droop controllers.

On an intuitive level, $Q$ describes the uncertainty present in the reconstructed disturbance, both in terms of magnitude and its 'distribution', i.e. where the disturbance is presumed to originate from. Meanwhile $R$ represents the uncertainty due to the pseudo-measurement, and how accurate it may be to use a local frequency measurement as a proxy for remote frequency measurements.

The variance of these quantities can be experimentally computed, in order for estimator tuning. To determine $Q$, we can explicitly measure $\hat{w}$ by taking the difference between

the true disturbance and the reconstructed disturbance. Similarly, we can compute $R$ by measuring $h$, the difference between the actual inverter output frequencies throughout the microgrid compared to the local inverter frequency. These variances are time-varying, as the transient errors are expected to exceed the errors at equilibrium; after the inverters have settled, the steady-state values are more easily predicted due to the frequency synchronization and proportional load sharing.

To standardize this computation, we can take the covariance measured for a predetermined disturbance, over the settling time of the inverter; after this transient period, the errors are expected to be smaller due to the steady-state frequency synchronization and load sharing. The magnitude of this predetermined tuning disturbance depends on expected conditions for the system.

An example is illustrated in figure 7.2, which shows the error associated with the pseudo-measured frequency, as well as the error associated with the reconstructed disturbance. In both cases, we see that the steady state error decays to 0 after the inverter response has settled. For this scenario, the measurements are taken at node 1, while the actual disturbance occurs at node 3; the specific topology is not particularly relevant to this example aside from denoting that the measured and disturbed nodes are not the same.

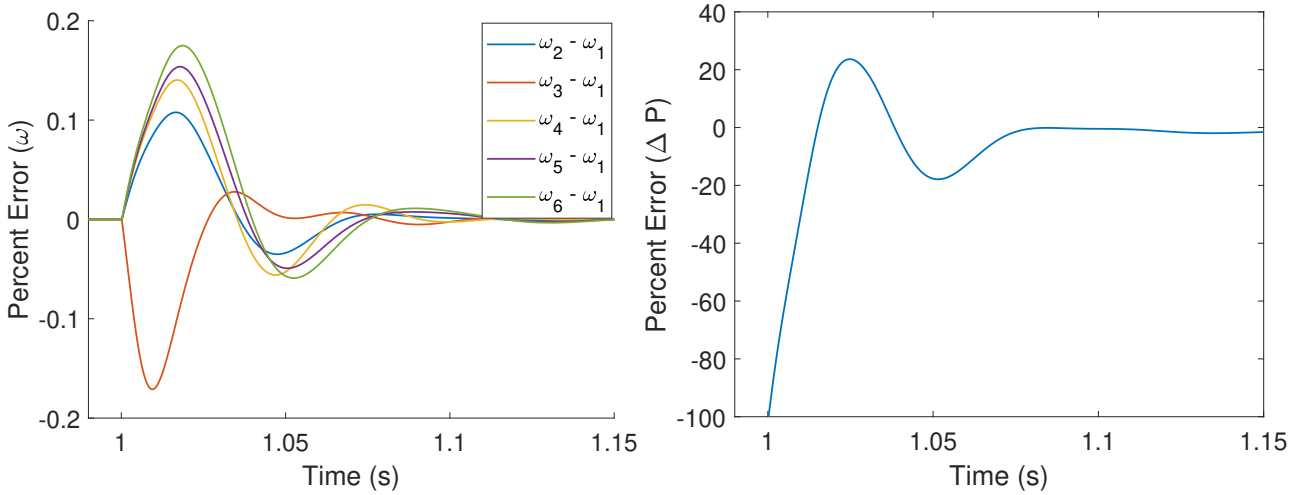


(a) Error (as a percentage) associated with using $\omega_1$ as a proxy measurement for other inverter frequencies throughout the microgrid.

(b) Error (as a percentage) associated with the reconstructed power disturbance, based on local measurements at node 1, compared to the actual power disturbance.

Figure 7.2: Error associated with using local measurements to approximate grid-wide values.

With covariance matrices $Q$ and $R$, along with the linear model defining the problem, the estimator gain $L$ can then be obtained, as described in chapter 2 or the provided references.

## 7.4 Extensions to Control

In this section we outline how the aforementioned estimator may be used to facilitate control of the microgrid. We describe how the estimator can coordinate to allow for state feedback control, as well as why this design is useful.

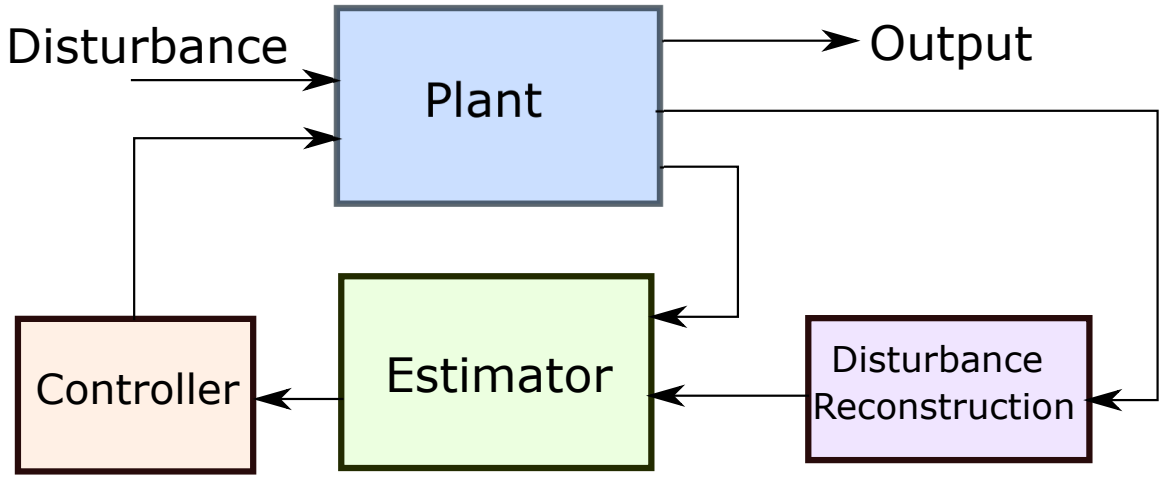


Figure 7.3: Block diagram structure outlining general controller-estimator structure

The proposed estimator allows for decentralized state feedback control, in which knowledge of the state of the system is required for effective control. As has been outlined in previous sections, decentralized control is constrained to use only local sensor data for control, and as such full-state feedback control is typically not feasible. In this case, however, the use of the decentralized estimator allows for full-state feedback control; the controller is actuated based on the estimate of the state.

This is similar to the concept of the linear-quadratic-Gaussian (LQG) controller, in which a Kalman filter is used to estimate the state of the system, and then this estimate is used for control actuation via the linear-quadratic-regulator (LQR) control law. This problem is compounded slightly due to the necessity to estimate the disturbance as well. The general estimator-controller structure is illustrated in figure 7.3, in which it can be seen how the various components of this system would coordinate with each other. For this application, local sensor readings are used to reconstruct the disturbance. These local

measurements, along with the estimated disturbance, are then used to estimate the state of the full microgrid. This estimate is then used to generate a local control signal to be sent to the microgrid.

That said, there is the question of why a state estimate would even be required. Conventional decentralized controllers, such as droop controllers, do not require full-state information to make a control decision. Similarly, the methods outlined in previous chapters only require local sensor data for real-time control.

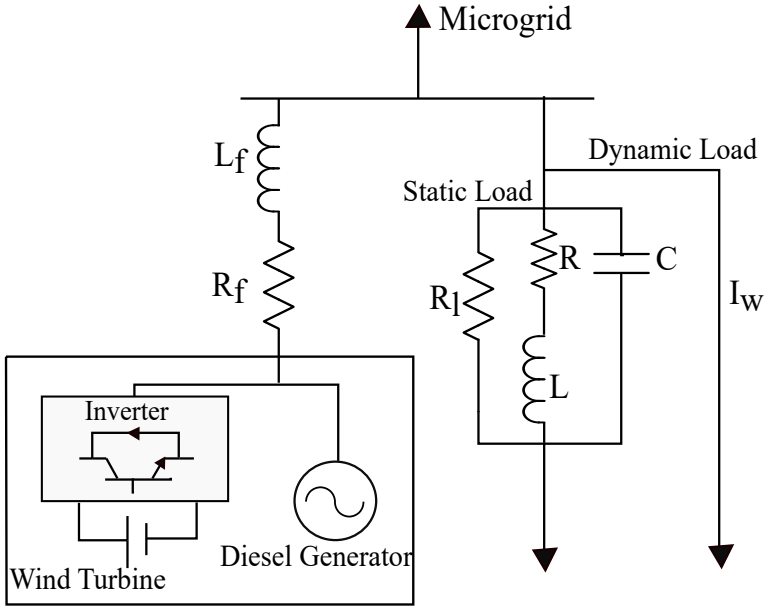


Figure 7.4: Hybrid controller featuring a wind turbine for fast power injection, and a diesel generator for sustained power output.

The primary motivating factor for the estimator-controller structure is to facilitate coordinated control between power sources, as may be the case when an individual controller is designed to operate based on the status of a remote power source or grid condition.

Consider figure 7.4, in which a wind turbine and synchronous generator are coordinated for microgrid support; this controller structure was outlined in detail in chapter 6. The general idea was that synchronous generators can offset microgrid power imbalances via sustained increases in power output, but these sources ramp up slowly; meanwhile wind turbines can be controlled to rapidly provide power injections to the grid, but cannot sustain this output without jeopardizing turbine stability. These two sources were coordinated such that while the slower power source ramped up to its new reference output, the faster power source provided the difference between the actual power output and the reference power output of the slower source. However a key idea in this process is that the control signal to the fast source is dependent on information regarding the current status of the slow source; without this information, coordination is impossible.

Similarly, methods like model predictive control require information about the system's full state in order to make control actions. In these control architectures, decisions are designed by minimizing a cost function subject to some set of constraints, but this cost function generally includes the condition of the full state. The proposed estimator would allow for decentralized estimation, such that the problem of decentralized model predictive control would be reduced to the traditional model predictive control problem.

To verify the effectiveness of this estimator for control applications, we consider a simplified version of the control design outlined in chapter 6. This basic control law can be summarized as follows:

$$\begin{aligned} \frac{d}{dt}(P_{slow}) &= \frac{1}{\tau}(P_ref - P_{slow}) \\ P_{fast} &= P_{ref} - P_{slow}, \end{aligned} \tag{7.26}$$

where $P_{ref}$ refers to the reference power output to which the slow source is ramping; $P_{fast}$ and

$P_{slow}$ refer to the power outputs from the fast and slow controlled power sources, respectively; $\tau$ refers to the time constant of the dynamic response associated with the slow power source.

However unlike the methods in chapter 6, we consider again a 6-node microgrid in which the fast and slow power sources are separated and do not have explicit real-time measurements regarding the status of the other. In this case, we consider the microgrid configured as in figure, in which the 'fast' wind turbine is located at node 1, and the 'slow' diesel generator is located at node 6. The power reference for the slow power source is computed to be 30% of the increased load seen at node 6:

$$P_{ref} = 0.3\Delta P_6. \tag{7.27}$$

Now the control law for the fast power injection is designed instead as

$$\begin{aligned} \frac{d}{dt}(P_{slow}) &= \frac{1}{\tau}(P_ref - P_{slow}) \\ P_{fast} &= \hat{P}_{ref} - \hat{P}_{slow}, \end{aligned} \tag{7.28}$$

where $\hat{P}_{ref}$ and $\hat{P}_{slow}$ refer to the estimates for the new reference output, as well as the estimate of the power output from the slow source. In this case we do not model the full controller design, which would include wind turbine modeling and optimal blade pitch angle actuation; this is a simple reproduction of the controller designed to identify whether remote coordination can be effective.

## 7.5 Simulations and Results

In this section we present the results of the estimator, as well as the estimator as applied to the coordinated wind turbine control problem. We show estimator performance

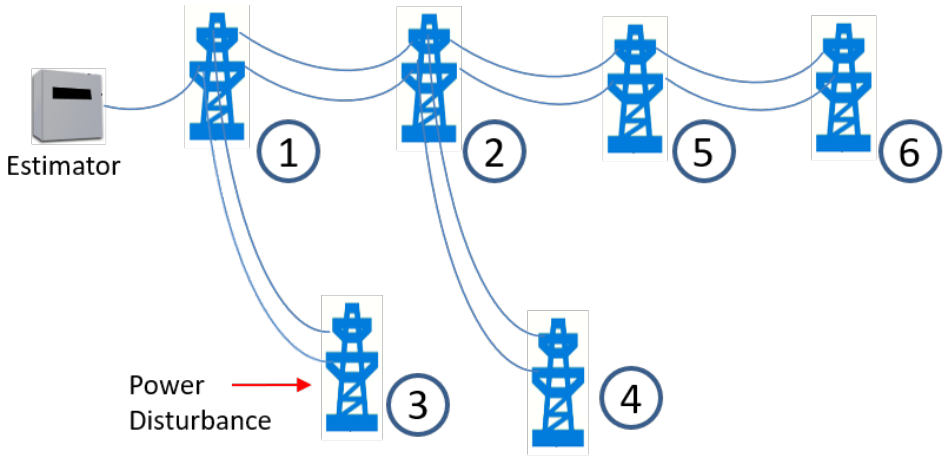


Figure 7.5: Example microgrid with estimator

when the disturbance location with respect to the grid is unknown, and considered to be evenly distributed throughout the grid. In addition, we also show estimator performance when the disturbance location is similarly unknown, but the covariance matrices $Q$ and $R$ have been tuned to better match the disturbance; this is representative of the case where historical load data may be used to provide more insight into prior probability distributions.

Microgrid parameters are given as in table 4.1; all power sources are identically rated. The specific interconnection within the grid is shown in figure 7.5. The estimator is at node 1, and therefore only has access to real-time measurements from node 1.

Covariance matrices $Q$ and $R$ are approximated by measuring the system response to a predetermined step disturbance at node 5; this location was randomly chosen. Its magnitude is taken to be a 50% step increase of the steady-state active power load at node 5, corresponding to a 8.4% in grid-wide load. The time constant for the filtered power is set to be $\tau_f = 0.015$, tuned experimentally.

The estimator is tested against a step disturbance at node 3. Its magnitude is taken to be a 25% step increase of the steady-state active power load at node 3. This corresponds to a grid-wide increase of 4.2% of the active power consumption.

The hybrid controller is also tested using the proposed estimator. In this scenario, the controlled wind turbine is located at node 1, while the slower power source is located at node 6; in this way, the effectiveness of the estimate for control purposes can be evaluated. The same disturbance is simulated: a 25% step increase in active power demand at node 3. This configuration is shown in figure 7.6. For a given increase in load at node 6, $\Delta P_6$, the slow power source is controlled to increase its output to match 35% of this increase:

$$\Delta P_{ref} = 0.35 \Delta P_6. \tag{7.29}$$

The time constant for this slow power source is set as $\tau_s = 0.5$.

### 7.5.1 Estimation: Even Distribution of Reconstructed Load

In this scenario, the disturbance actually occurs at node 3; it is the load at node 3 that experiences the step increase. However the estimator reconstructs the magnitude of the disturbance, and instead assumes that this disturbance is evenly distributed across all nodes.

The estimated frequency from each individual inverter is provided in figure 7.7, while the estimated output current along the d-phase is given in 7.8. We can see that due to the identically distributed load assumption, the estimated quantities are similarly identical; this is to the detriment of the estimator accuracy, because the actual quantities are not identical to each other. However, while the estimate does suffer somewhat, it does succeed in terms

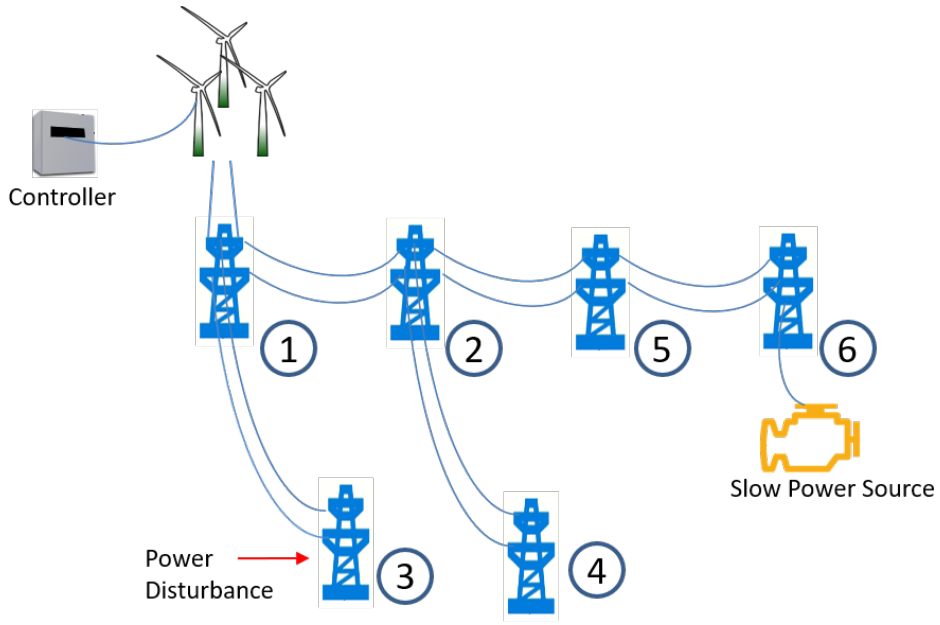


Figure 7.6: Example control application of proposed estimator design

of capturing some of the transient response; the estimated derivative is on the same order of magnitude, with correct sign. Moreover, the estimate rapidly converges as the inverter output settles.

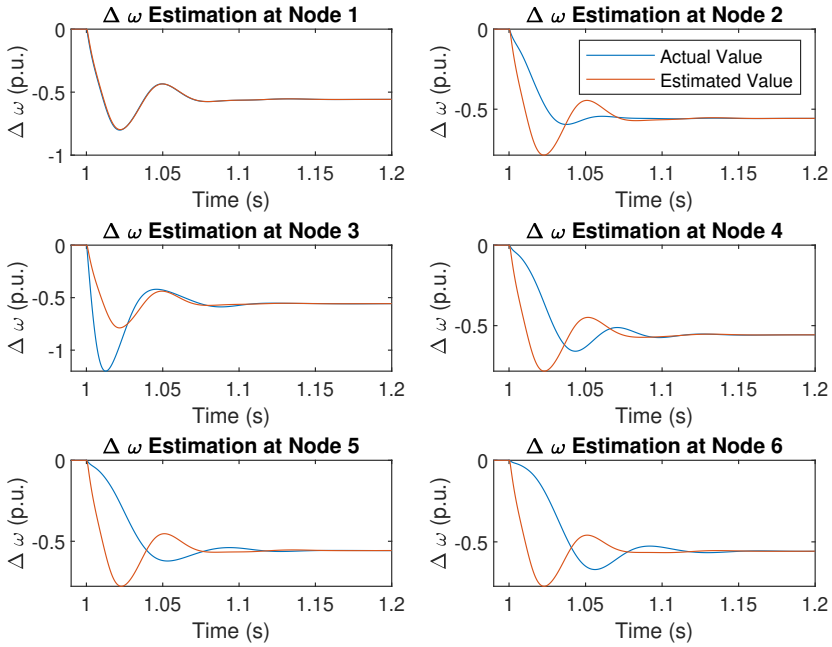


Figure 7.7: Estimated inverter output frequencies; load is assumed to be evenly distributed.

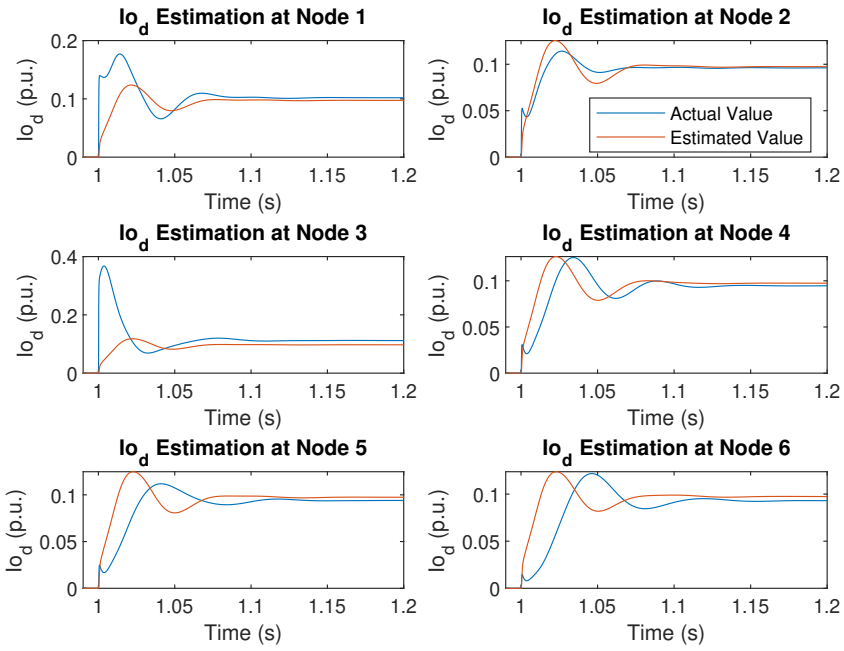


Figure 7.8: Estimated inverter output current; load is assumed to be evenly distributed

### 7.5.2 Estimation: Improved Covariance Matrix

In this scenario, the disturbance actually occurs at node 3; it is the load at node 3 that experiences the step increase. However the estimator reconstructs the magnitude of the disturbance, and instead assumes that this disturbance has occurred at its local node, node 1.

To demonstrate the relevance of an appropriate $Q$ matrix, the covariance of the disturbance error $\tilde{w}$, in this case we have fitted $Q$ more strongly to the simulated disturbance. This is meant to reproduce the case in which we have more prior information regarding the location of the disturbance. In this case we have designed $Q$ based on the pre-measured

system response to a 50% load increase at node 3; in contrast, the actual disturbance is a 25% load increase at node 3.

The estimated frequency from each individual inverter is provided in figure 7.9, while the estimated output current along the d-phase is given in 7.10. In these figures we can see that while the 'location' assumption was incorrect, the resulting estimate appears to be more accurate than the previous case in which the disturbance was assumed to evenly distributed throughout the microgrid. Notably, however, the estimates at node 3 are conspicuously worse than the other estimates.

The purpose of these figures is to highlight that information regarding load distribution probabilities can be helpful in improving the state estimate, by allowing for better tuned covariance matrices, $Q$. This is an overfitted example, but presents an 'ideal' case.

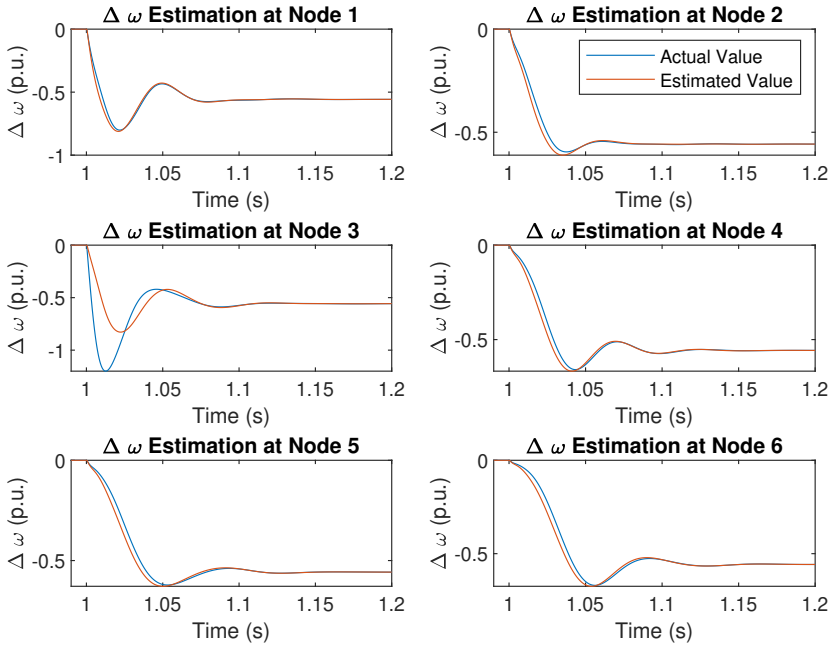


Figure 7.9: Estimated inverter output frequencies; system has been tuned for this disturbance

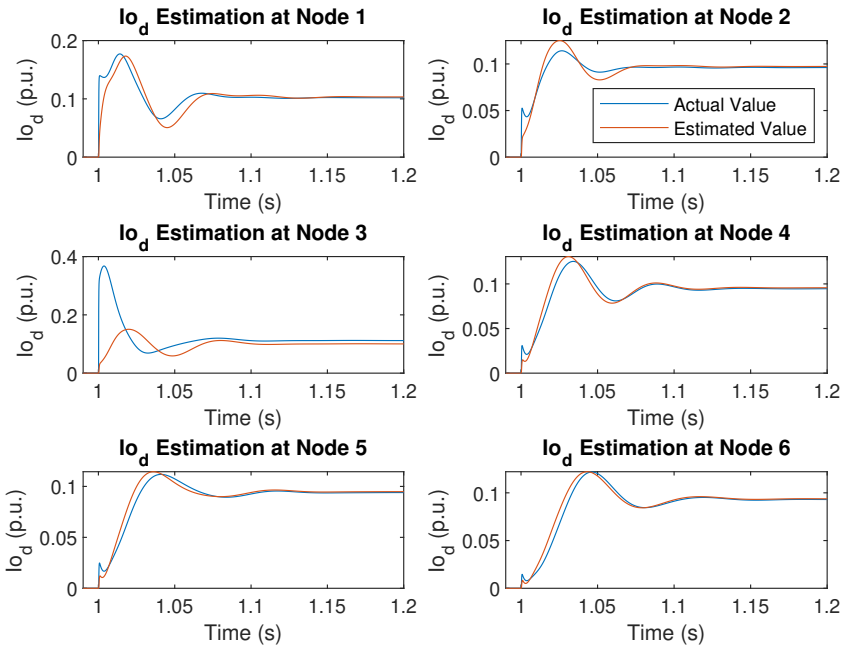


Figure 7.10: Estimated inverter output current; system has been tuned for this disturbance

### 7.5.3 Estimator for Control

For this result, we compare the microgrid response across 5 scenarios. (1) The microgrid receives no power support from either the slow or fast power sources. (2) The microgrid only receives support from the slow power source. (3) The microgrid receives support from both power sources, and the wind turbine has explicit state knowledge of the slow controller so the estimator is not required. (4) The microgrid receives support from both power sources, and the wind turbine uses the estimator to determine the status of the slow power source, and thus its own control action; the estimator has no prior knowledge about the nature of the disturbance, and the reconstructed load is evenly distributed throughout the microgrid.

(5) The microgrid receives support from both power sources, and the wind turbine uses the estimator to determine the status of the slow power source, and thus its own control action; the disturbance covariance matrix is fitted closely to the actual disturbance.

The controller performance can be seen in figure 7.11, which shows the average frequency error in each of these cases. It can be seen that without any support, the frequency error is greatest, while with only the slow support, the frequency error slowly decreases over time.

When the wind turbine is included, allowing for fast power injection, the results with and without estimation are comparable. Even when the transient estimate is poor, as in the case where the reconstructed load is evenly distributed throughout the grid, the estimate is still sufficient for effective control. In all cases, the frequency undershoot and settling time are approximately consistent with each other. This suggests that for this application, the proposed estimator is sufficient to be used for effective control.

### 7.5.4 Comparing Proposed Estimator Design to Conventional Estimator

We now compare these results to the case of the typical estimator design, in which we do not make the pseudo-measurement approximation, i.e. that the measurement of frequency at node 1 is a reasonable proxy for a measurement of frequency at a remote node. We also consider the performance of the conventional estimator with and without the reconstructed disturbance.

In this case, we consider the estimator where

$$y_k = [I_{o,d1}, I_{o,q1}, V_{g,d1}, V_{g,q1}, \omega_1]^T. \tag{7.30}$$

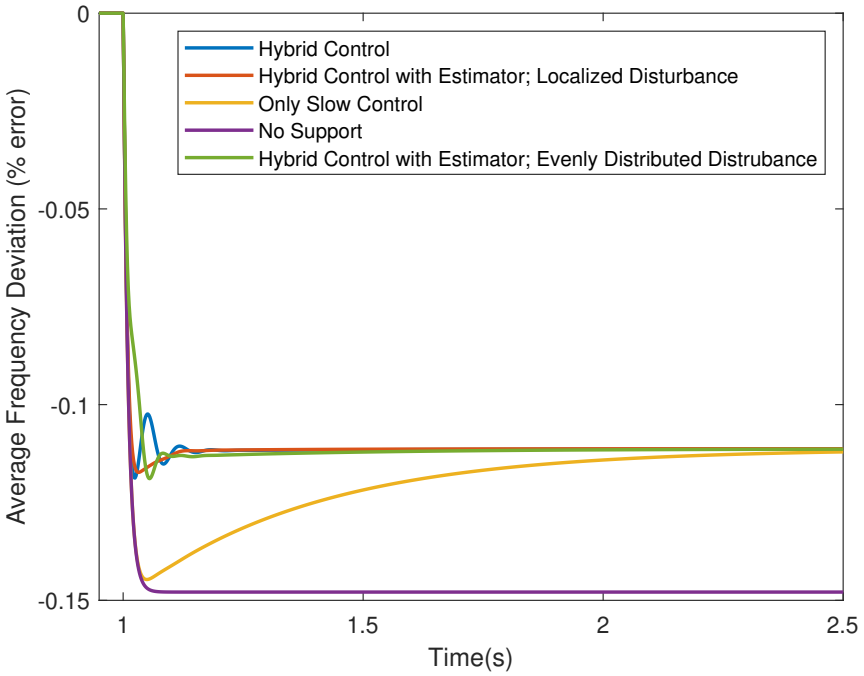


Figure 7.11: Hybrid controller performance across various scenarios, comparing performance where the state information is exactly known vs. when it must be estimated.

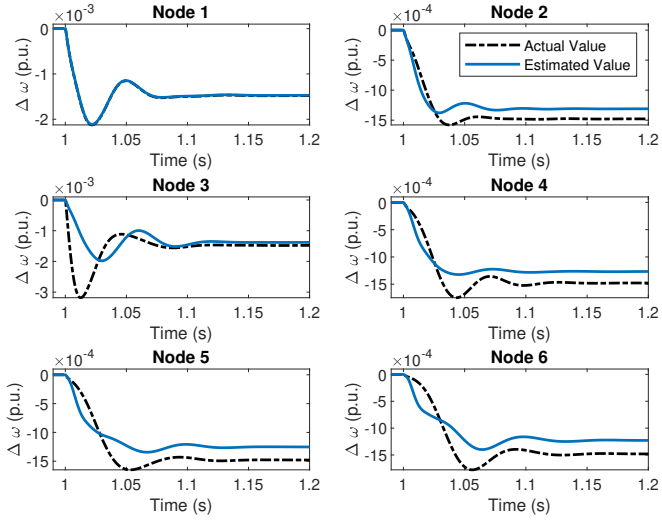


Figure 7.12: Conventional estimator performance without including the reconstructed disturbance; estimating inverter frequencies.

These are all local state measurements made at node 1. Alternatively we compare this to the proposed estimator design, in which the only measured variable is $\omega_1$, which stands as a proxy for other frequencies throughout the microgrid.

$$y_p = [\omega_1, \omega_1, \ldots, \omega_1]^T. \tag{7.31}$$

First we show the performance of the conventional estimator that utilizes the reconstructed disturbance. In figure 7.12, we see the estimates for inverter frequency. It is readily apparent that the conventional estimator suffers compared to the proposed estimator shown in 7.9; in particular, the estimator is unable to correctly track the steady-state frequency for remote nodes in contrast to the proposed estimator design. The estimate at the local node tracks the actual value effectively, but at remote nodes, the estimate is comparatively poor.

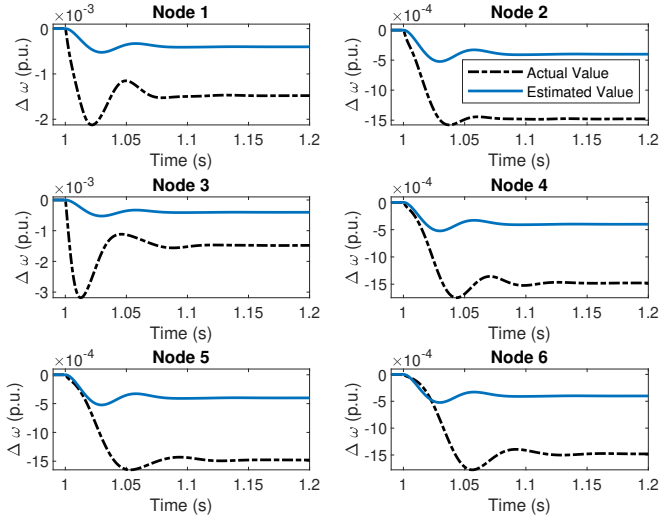


Figure 7.13: Conventional estimator performance without including the reconstructed disturbance.

We then consider the performance of the conventional estimator without the benefit of the reconstructed disturbance, in figure 7.13. Here there are conspicuous losses; the estimated frequencies are egregiously incorrect compared to the actual values both in terms of their transient and steady-state values.

## 7.6 Discussion

From these results, we have two main conclusions. The disturbance reconstruction is shown to be effective, and the pseudo-measurement of frequency allows for state estimation of non-frequency variables. This facilitates state feedback control in which local controllers require knowledge of remote states.

First we see that the disturbance reconstruction method allows for significantly im-

proved estimation. Even without knowing the origin of the microgrid disturbance, we are able to reasonably approximate the magnitude of the increased power demand on the system. This in turn allows for state estimates that are free of steady-state offset error.

Second, the pseudo-measured frequency allows for improved state estimates at remote nodes. The resulting state estimates are shown to reasonably track the true steady-state, unlike the estimates produced by the conventional state estimator in which this pseudo-measurement is not taken. The argument could be made that because frequency converges anyway, frequency estimates are less powerful; however as shown, even the output current is shown to be tracked with this proposed design.

Notably, the choice of the covariance matrix $Q$ has a significant effect on the performance of the estimator. In this design, $Q$ is chosen by simulating the microgrid response to some predetermined disturbance, and then comparing the true disturbance to its reconstructed value. Therefore if the system is tuned to expect disturbances at node $j$, and the actual disturbance is at node $j$, then the estimator can better relate its measurements for accurate estimates. While it is impossible to know the future, this highlights the need and relevance for accurate data in the design process. That said, even the case that represented minimal *a priori* knowledge- tuning the estimator to expect disturbances along all channels with equal probability- resulted in reasonable state estimation that was able to effectively track the steady states.

These results allow for effective coordinated control. With the ability to locally estimate the state at a remote node, the wind turbine was able to coordinate its power output to minimize the overall frequency deviation in tandem with a slower diesel generator. This potentially has applications for more complex control schemes, in which knowledge of

the full state is required.

## 7.7 Conclusion and Future Work

The presented method allows for full state estimation using only local real-time measurements. Taking advantage of the frequency synchronization intrinsic to power systems, as well as the active power load sharing presented by synchronous generators and droop-controlled inverters, we are able to design an estimator for improved real-time state estimation. This makes it possible to implement controllers that require full-state information. These results compare favorably to the 'conventional' estimator, which neglects to take advantage of this synchronization.

In addition, we present a disturbance reconstruction method in order to address the issue that standard estimation techniques demonstrate steady-state offset errors with disturbances that have nonzero mean. In this way, local measurements are used compute the magnitude of the disturbances to active power in the system. This facilitates state estimation that is free of steady-state offset error; without this disturbance reconstruction, the state estimate is shown to suffer significant losses.

We note that the covariance matrices, $Q$ and $R$, play a significant role in the accuracy of the estimate, and in this leaves an open question for future work. The matrix $Q$ describes the uncertainty present in the reconstructed disturbance, both in terms of magnitude and its 'distribution', i.e. where the disturbance is presumed to originate from. Meanwhile $R$ represents the uncertainty due to the pseudo-measurement, and how accurate it may be to use a local frequency measurement as a proxy for remote frequency measurements. These quantities are data-dependent, varying with typical load usage profiles and the structure of

the network at the very least. The best choices of these matrices may result in significantly improved state estimates; inversely, poor selection of $P$ and $Q$ may result in considerable losses. A method to better determine these values is an avenue for future work.

# Chapter 8

# Conclusion

We have presented a series of topics that share a consistent theme and build off each other, and so it may be useful to review that overarching idea here. The main goal has been to explore the limits of decentralized control in an islanded microgrid. In answering this question, we have attempted to understand the role that the microgrid model can play in decentralized control.

We first presented results in which all inverters were controlled as desired. This demonstrated the effectiveness of decentralized control in microgrids, and showed that H-infinity methods could be used to more optimally control the transient response in microgrids. These results showed effective improvements in both voltage and frequency. However the limitation with this methodology was that while it could be effective in isolation, it did not allow for synchronous operation in parallel with more conventionally controlled power sources. The control was effective, but it required that all controllers followed the prescribed control scheme in order to maintain frequency synchronism between power sources. This can be a limiting factor in microgrids, where we seek modular 'plug and play' controllers.

Therefore this was followed with a framework which was designed to easily operate in parallel with a conventional microgrid, with either synchronous sources or droop-controlled inverters. We outlined a method with which individual inverters could be controlled, so as

to improve the robustness and transient performance of a microgrid. These results were successful in that we identified that the structure or topology of a microgrid can impact the transient response and stability of the system, and that this transient behavior could be improved by judiciously placing individual controllers.

The challenge with this methodology was that while the controllers were able to improve the microgrid response, the implication was also that more such controllers were required in order to be assured of 'good' performance. The proximity of the controller relative to the disturbance, in addition to its location within the microgrid, had a pronounced effect on its grid-wide impact; therefore it would be reasonable to assume that the best performance could be attained if all the inverters were controlled in such a manner. However in this approach, the proposed control would override the frequency-setting ability of a droop controller, rather than working alongside it. Because the controller modulated its output power in order to effect change, it was no longer possible to set frequency or voltage proportional to this same output power. In this sense, an increased number of such controllers would actually detract from the microgrid's robustness. In the extreme case, where all inverters but one were controlled with the proposed design, then there would only be one frequency-setting unit in the microgrid; if this unit were to go offline for any reason, the microgrid would not be able to stably operate without changing the control scheme.

To avoid the issue of a single point of failure, we followed these results with a decentralized control scheme in which instead of supplanting a droop controller, we supplemented it. We designed an alternative to the droop law, in which the steady-state behavior was unchanged, while the transient behavior was improved. No additional sensor data would be required, nor would any additional power injection be necessary, particularly since the

steady-state power sharing was unchanged; this was an alternative decentralized rule for how frequency and voltage could be set by the inverter. Most importantly, this method could easily operate in parallel with existing systems and controllers without introducing any failure points; it was even shown that the transient microgrid performance could be significantly improved if only a few judiciously chosen inverters were equipped with this proposed control design.

There are, however, no free lunches to be had in most areas of optimization. In this case, while the improvements were significant compared to the conventionally controlled microgrid, it came at the cost of synthesizing these controller gains with a microgrid model. However we were able to show that even with a reduced model, that only modeled the neighboring regions of the microgrid relative to the controller, the resulting controller was still able to provide significant improvements.

In addition to focusing on 'grid-wide' interconnections and control, we also presented a specific application to improve microgrid power quality in which a wind turbine was controlled to provide frequency support for a microgrid. In the previous cases, the overall amount of power supplied to the grid did not change; we just modified how this power was supplied, in order to minimize transient losses. In this case, we explored how a wind turbine could be stably controlled in order to take advantage of the significant rotational inertia stored in its rotor, so as to provide power on-demand to the microgrid. The challenge was that the wind turbine had a limited amount of rotational power that it could safely afford to share with the grid, but by operating in tandem with a slower, sustained power source, we illustrated a design in which microgrid support could be supplied rapidly and sustainably.

This design faced challenges with regards to decentralization. As noted, the wind

turbine was used in such a way that made best use of its rapidly injected, but limited, power reservoir. However in order to make this control decision, the wind turbine needed to know the condition of other components connected to the grid. This motivated the idea of decentralized state estimation in a microgrid. If this were possible, then general optimal control methodologies which required full-state information could be more effectively realized.

We concluded this research by presenting a method for decentralized state estimation in a microgrid, in which local measurements made it possible to reasonably estimate the state throughout the microgrid. By leveraging the convergence of frequencies in a microgrid, as well as the active power sharing, local measurements provided insight into grid conditions throughout the system. This in turn made for improved state estimation using only local data. The effectiveness of this result was demonstrated with a simple reproduction of the aforementioned wind turbine controller; using this method, the wind turbine was able to coordinate with a remote power source for effective combined control.

Altogether the ideas presented here have shown how the extent to which decentralized control in microgrids can be expanded. As noted in the earlier literature review, a significant proportion of research focuses on decentralized control without considering the connectedness or model of a microgrid. We have shown that there significant benefits to be gained by considering the microgrid model during controller synthesis. As 'smart grids' and distributed energy resources continue to grow in the future, expanding our research perspective beyond the control of individual devices and inverters will allow us to consider how these modeled components work in tandem, and in so doing will provide more efficient answers to future questions.

# Appendices

# Appendix A

# Optimal Transient Droop Control

This appendix contains all the results described in chapter.

## A.1 Configuration 1: All Power Sources Identical

In this case, all microgrid power sources are identically rated. Results are shown for varying degrees of model complexity, and varying number of controllers.

### A.1.1 Full-Model; All Inverters Controlled

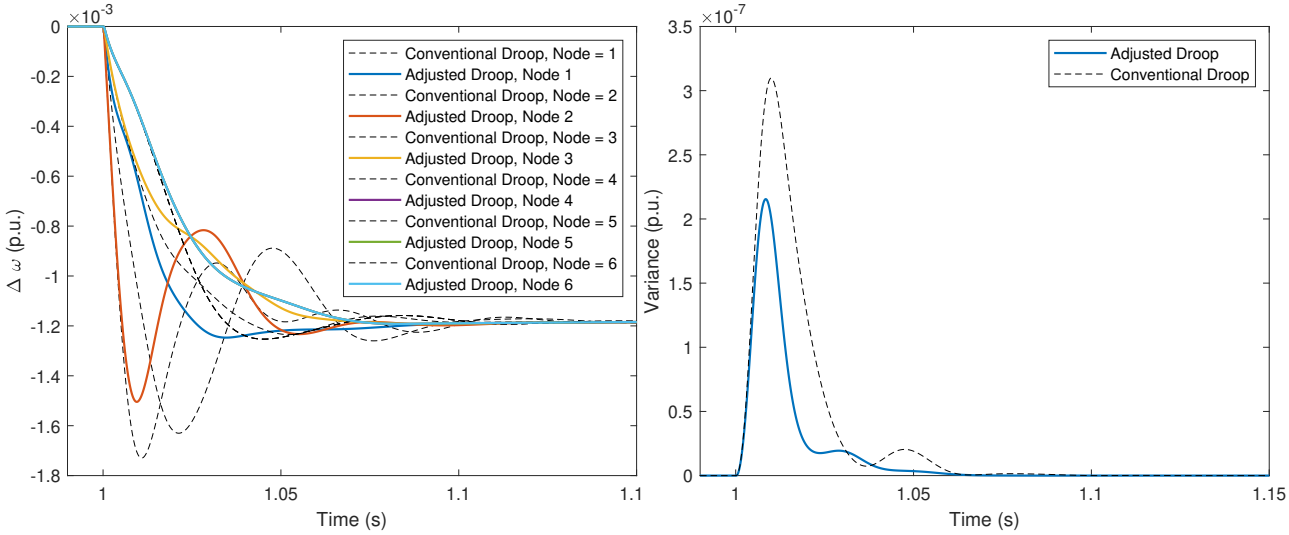


(a) Inverter output frequencies.

(b) Associated variance for inverter frequencies.

Figure A.1: Inverter output frequencies and associated variance for the full-model control synthesis; all generators are controlled.

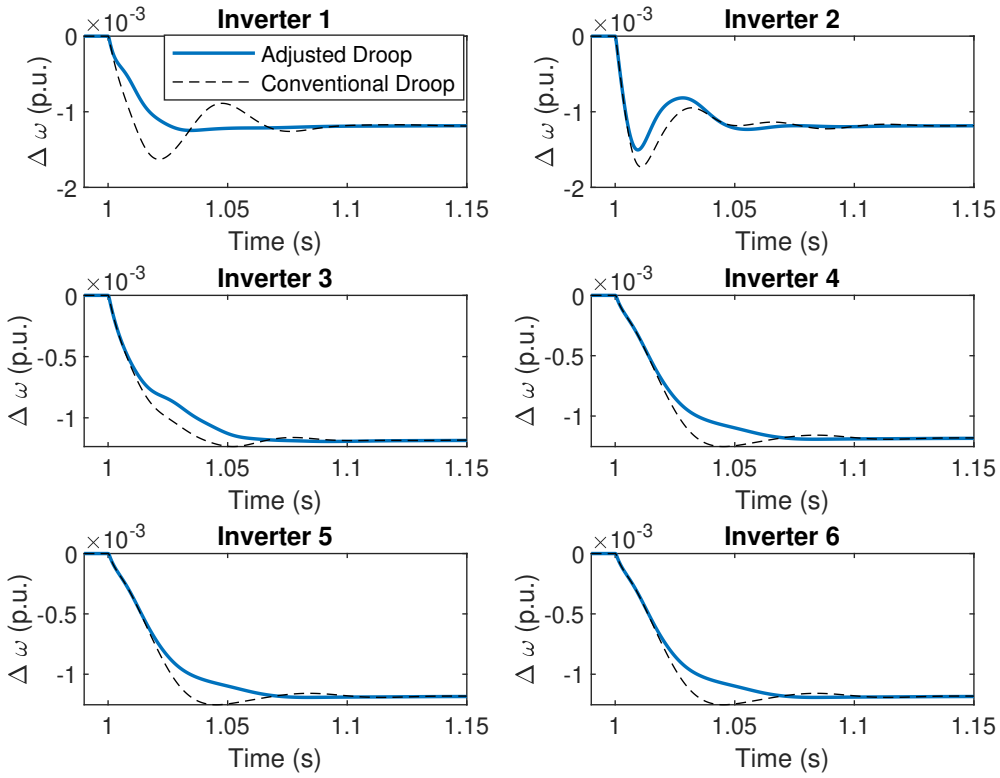


Figure A.2: Inverter frequency comparisons at each individual node, with and without droop adjustments. Results are for the full-model control synthesis; all generators are controlled

### A.1.2 Full-Model; Only Inverters 2, 3 Controlled

Here we reduce the number of controllers to only control inverters 2 and 3.

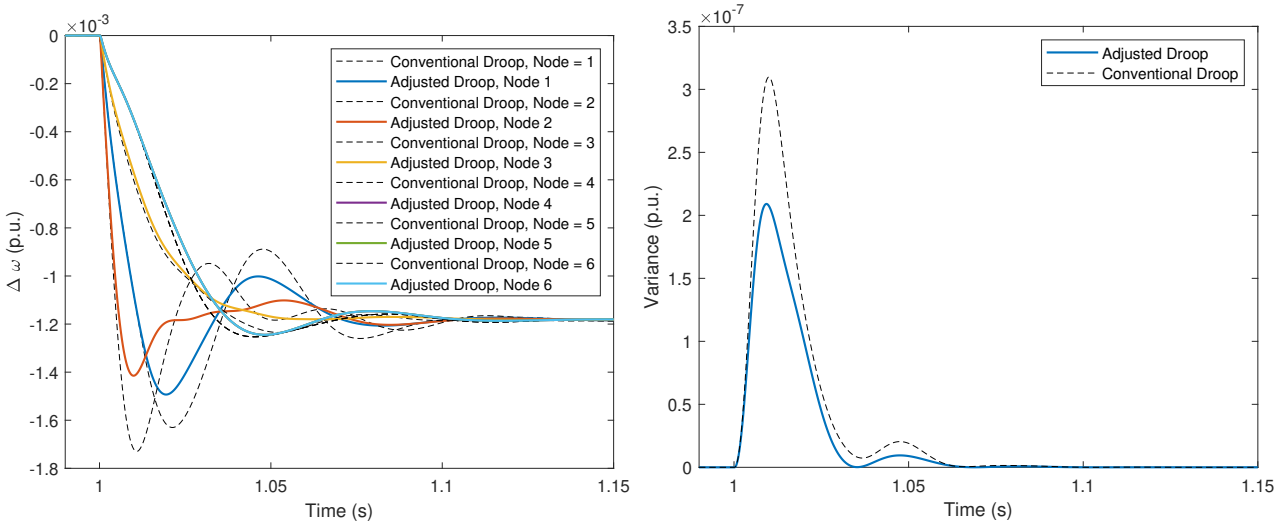


(a) Inverter output frequencies.

(b) Associated variance for inverter frequencies.

Figure A.3: Inverter output frequencies and associated variance for the full-model control synthesis; only inverters 2 and 3 have droop adjustments.

### A.1.3 Full-Model; Only Inverter 3 Controlled

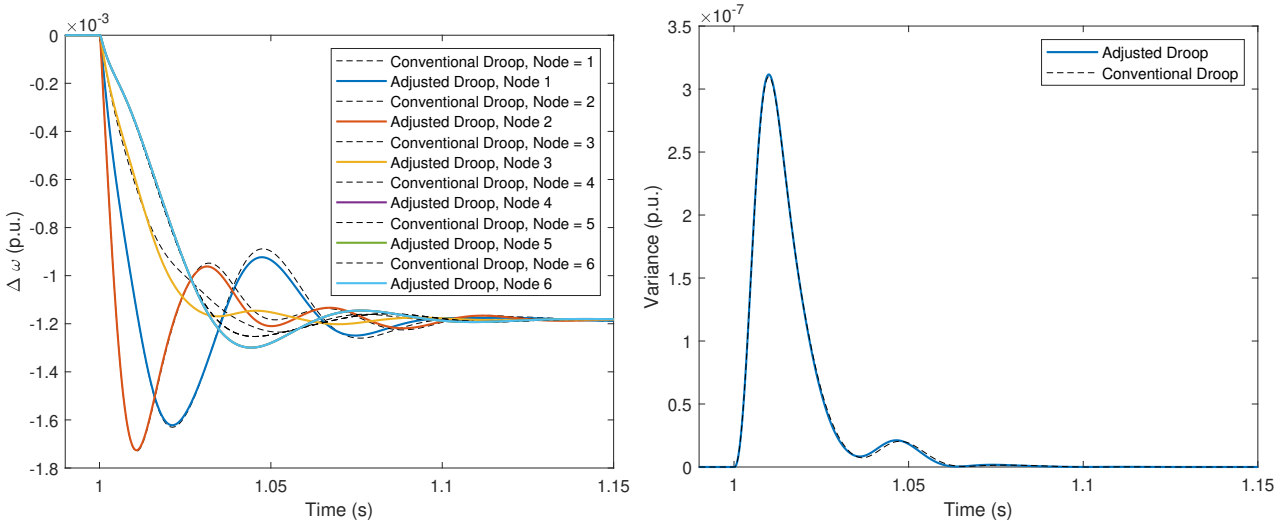


(a) Inverter output frequencies.

(b) Associated variance for inverter frequencies.

Figure A.4: Inverter output frequencies and associated variance for the full-model control synthesis; only inverter 3 has droop adjustments.

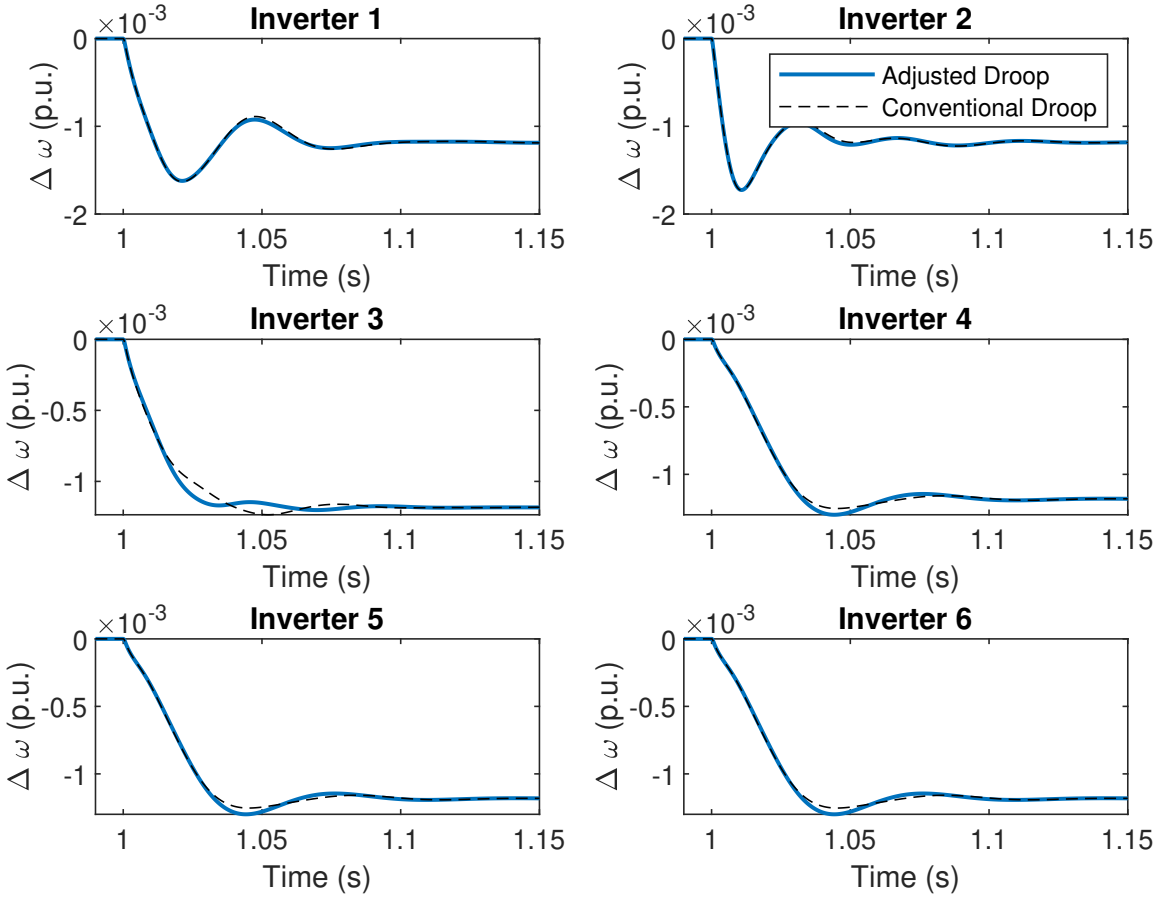


Figure A.5: Inverter frequency comparisons at each individual node, with and without droop adjustments. Results are for the full-model control synthesis; Only inverter 3 has droop adjustments

### A.1.4 Regional-Model; All Inverters Controlled

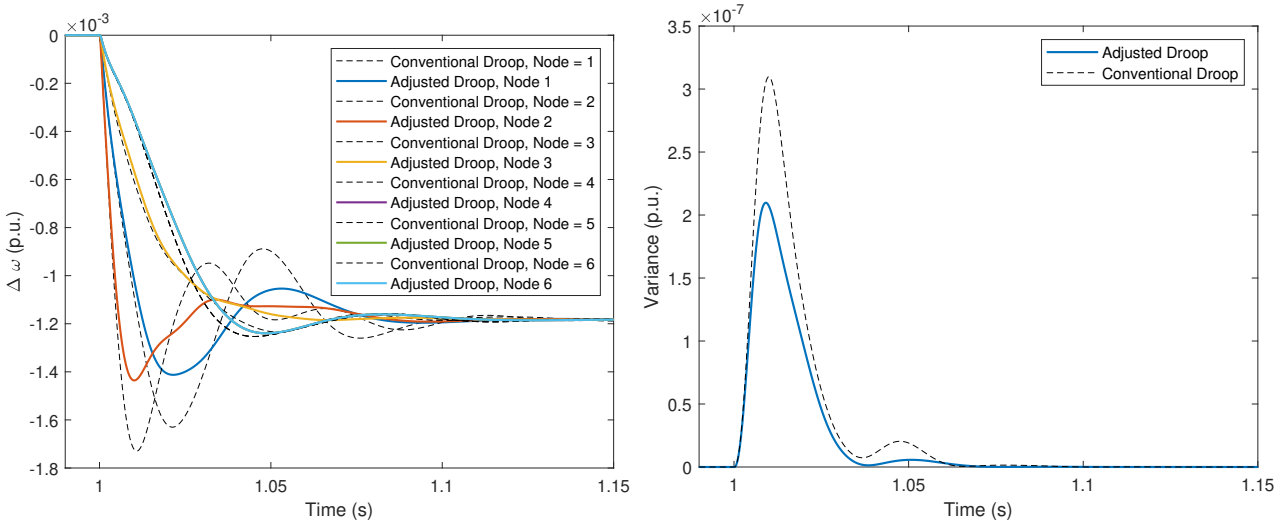


(a) Inverter output frequencies.

(b) Associated variance for inverter frequencies.

Figure A.6: Inverter output frequencies and associated variance for the regional-model control synthesis; all inverters have droop adjustments.

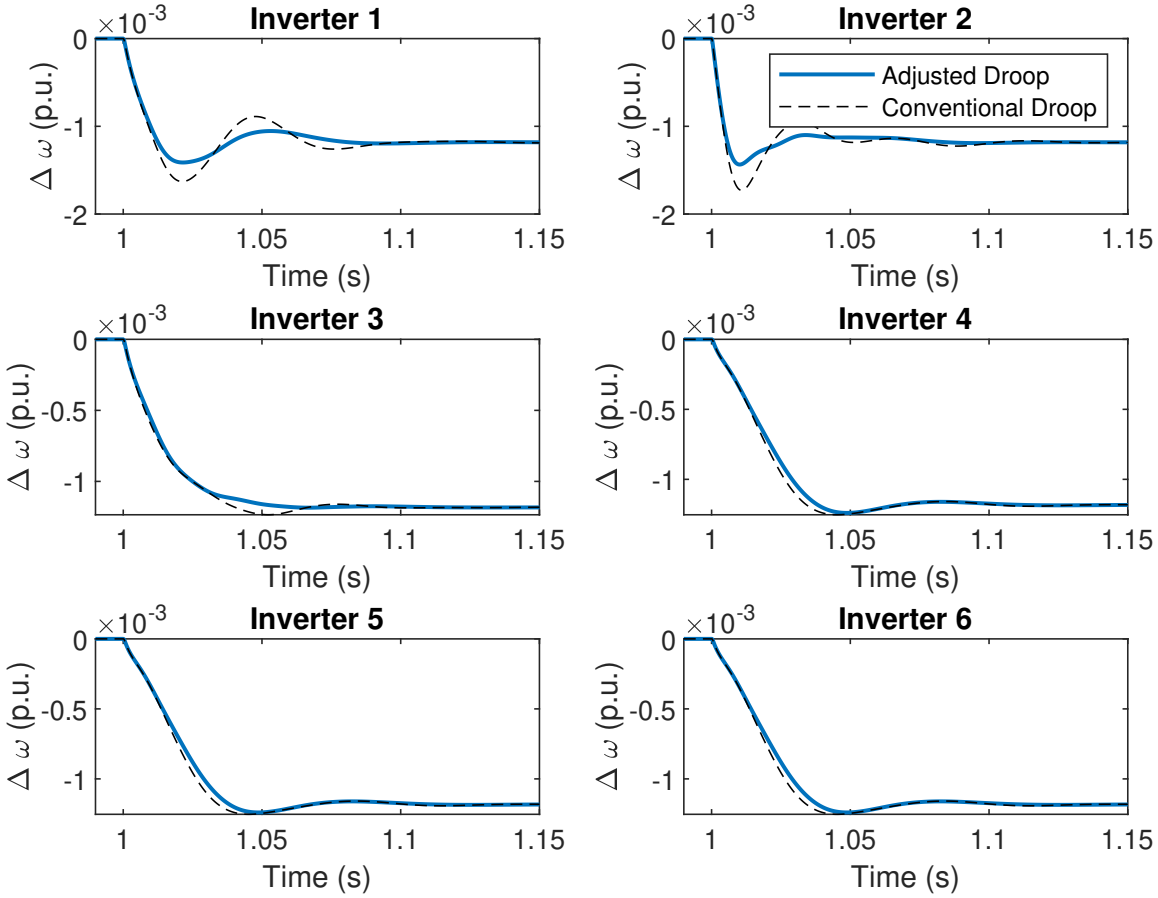


Figure A.7: Inverter frequency comparisons at each individual node, with and without droop adjustments. Results are for the regional-model control synthesis; all inverters have droop adjustments.

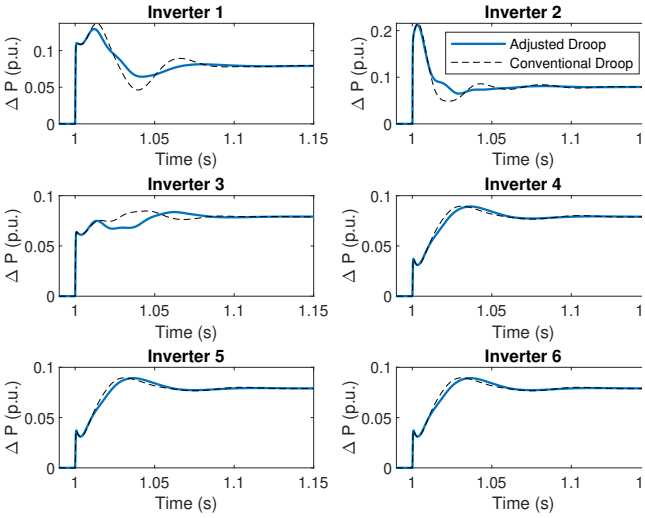


(a) Change in active power following a disturbance.

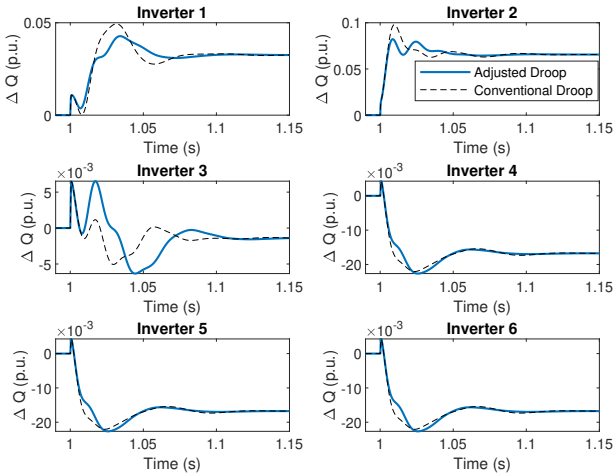


(b) Change in reactive power following a disturbance.

Figure A.8: Active and reactive power outputs for the regional-model control synthesis; all inverters have droop adjustments.

### A.1.5 Regional-Model; Inverters 2,3 Controlled

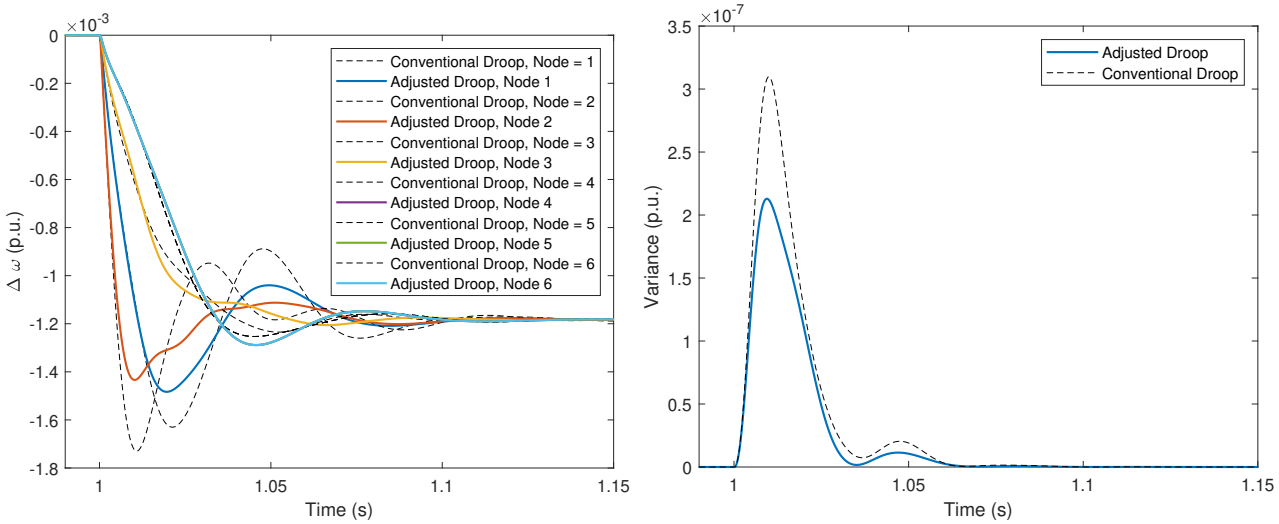


(a) Inverter output frequencies.

(b) Associated variance for inverter frequencies.

Figure A.9: Inverter output frequencies and associated variance for the regional-model control synthesis; only inverters 2 and 3 have droop adjustments.

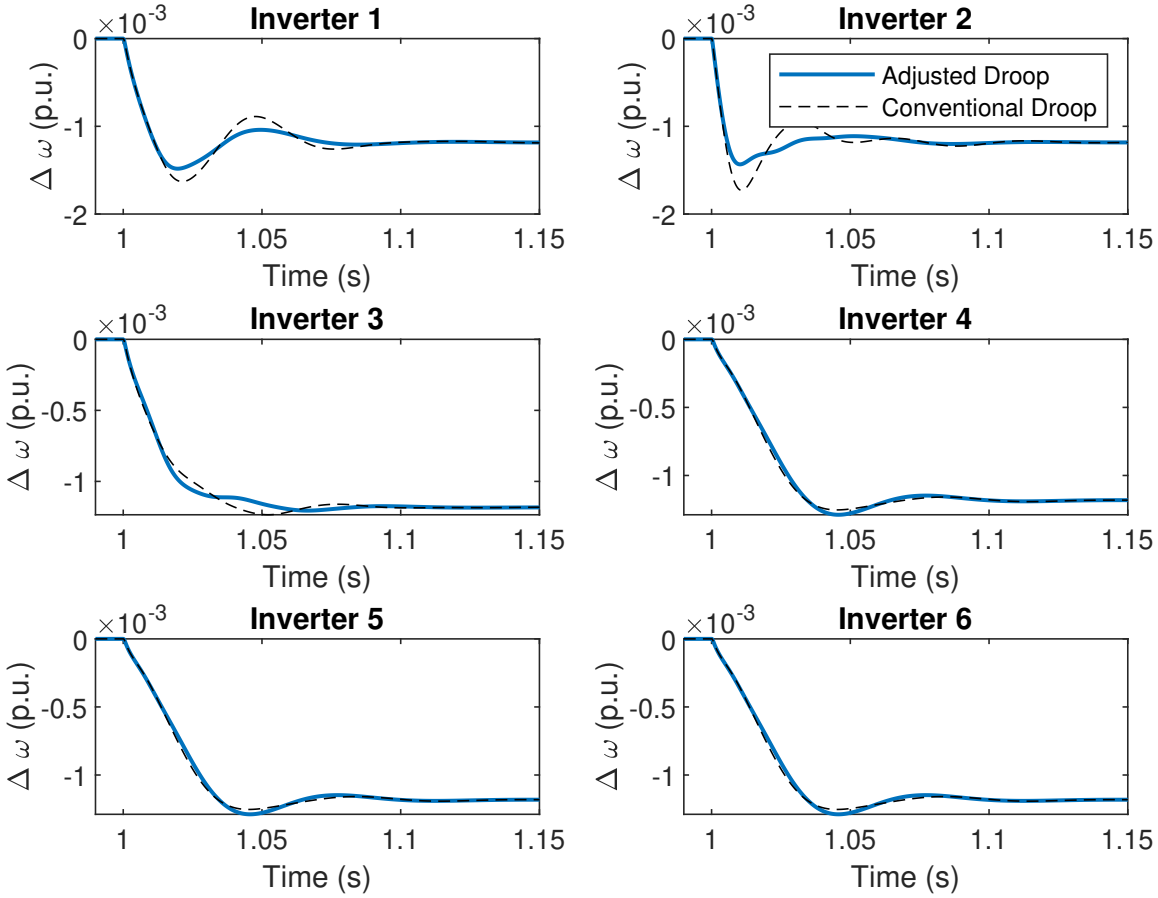


Figure A.10: Inverter frequency comparisons at each individual node, with and without droop adjustments. Results are for the regional-model control synthesis; only inverters 2 and 3 have droop adjustments.

### A.1.6 Solitary-Model; All Inverters Controlled

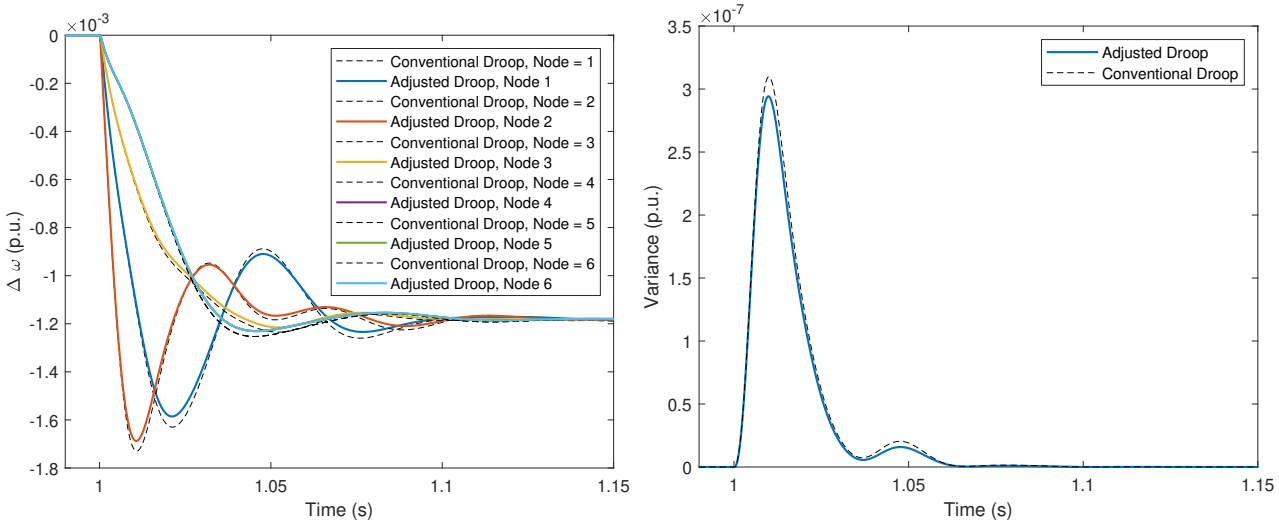


(a) Inverter output frequencies.

(b) Associated variance for inverter frequencies.

Figure A.11: Inverter output frequencies and associated variance for the solitary-model control synthesis; all inverters have droop adjustments.

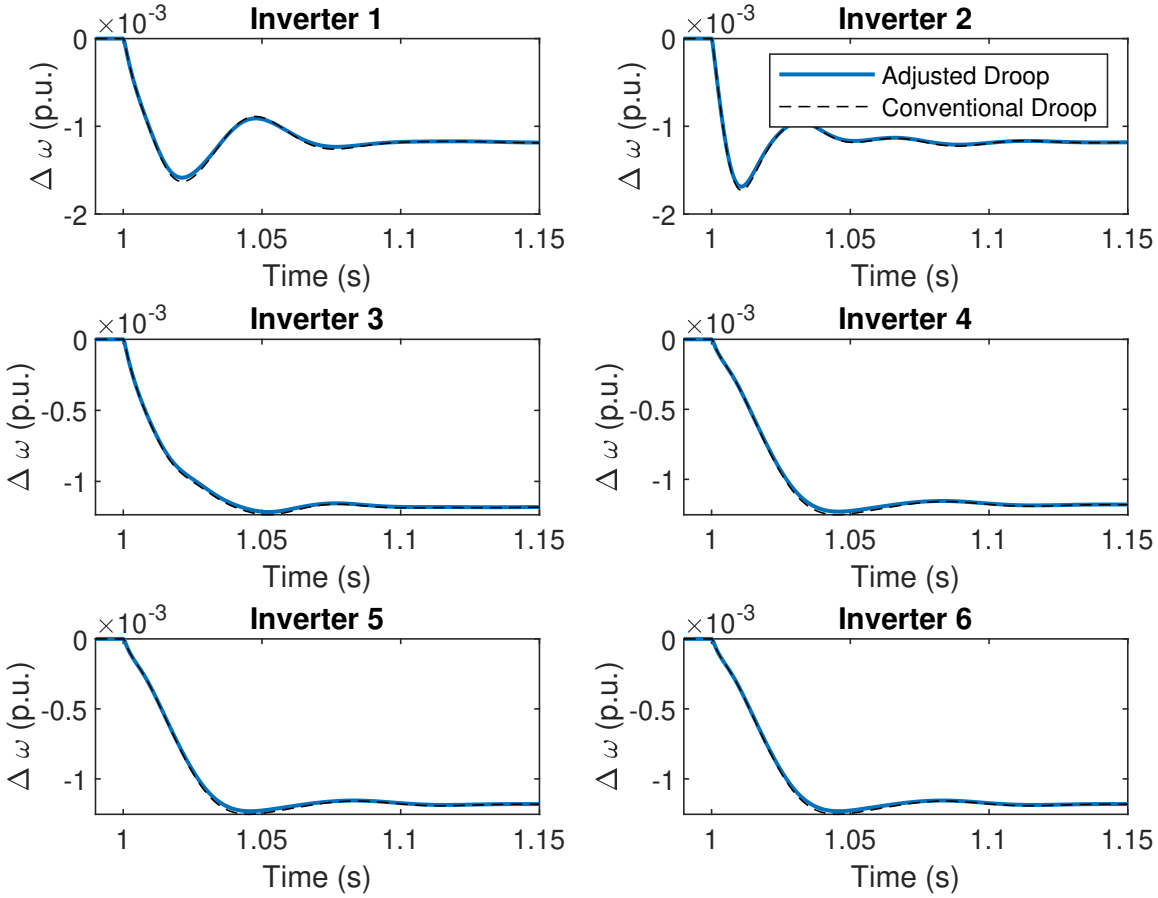


Figure A.12: Inverter frequency comparisons at each individual node, with and without droop adjustments. Results are for the solitary-model control synthesis; all inverters have droop adjustments.

## A.2 Configuration 2: Variation at Source 3

In this case, we vary the droop gain at node 3 to simulate the condition in which this power source can provide 67% of the rated power of the other sources.

### A.2.1 Full-Model; All Inverters Controlled

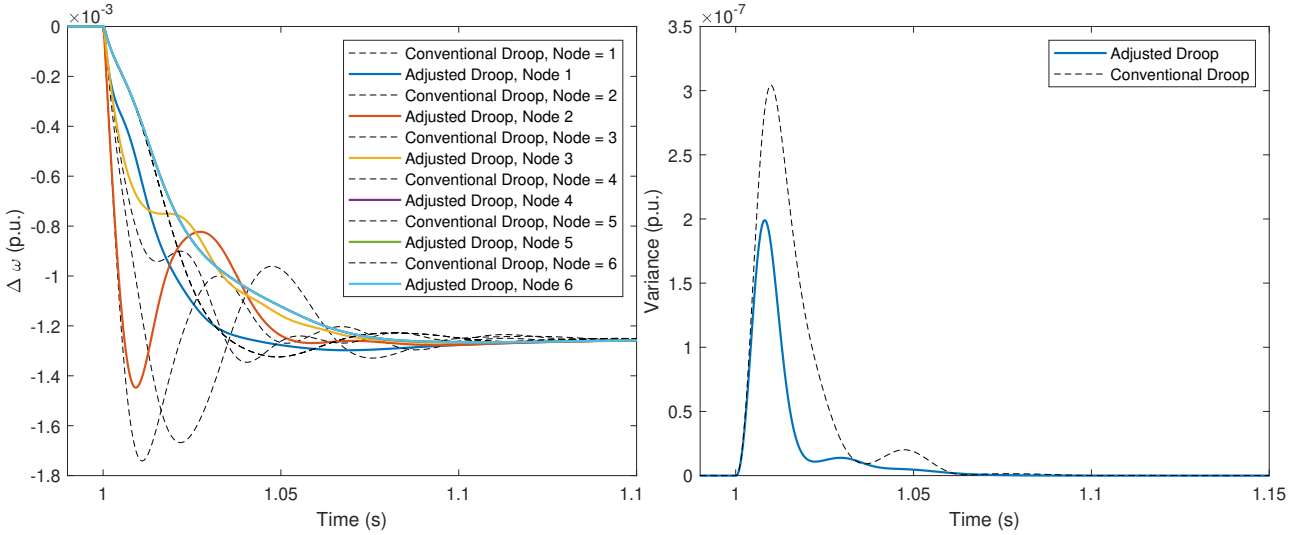


(a) Inverter output frequencies.

(b) Associated variance for inverter frequencies.

Figure A.13: Inverter output frequencies and associated variance for the full-model control synthesis; all generators are controlled.

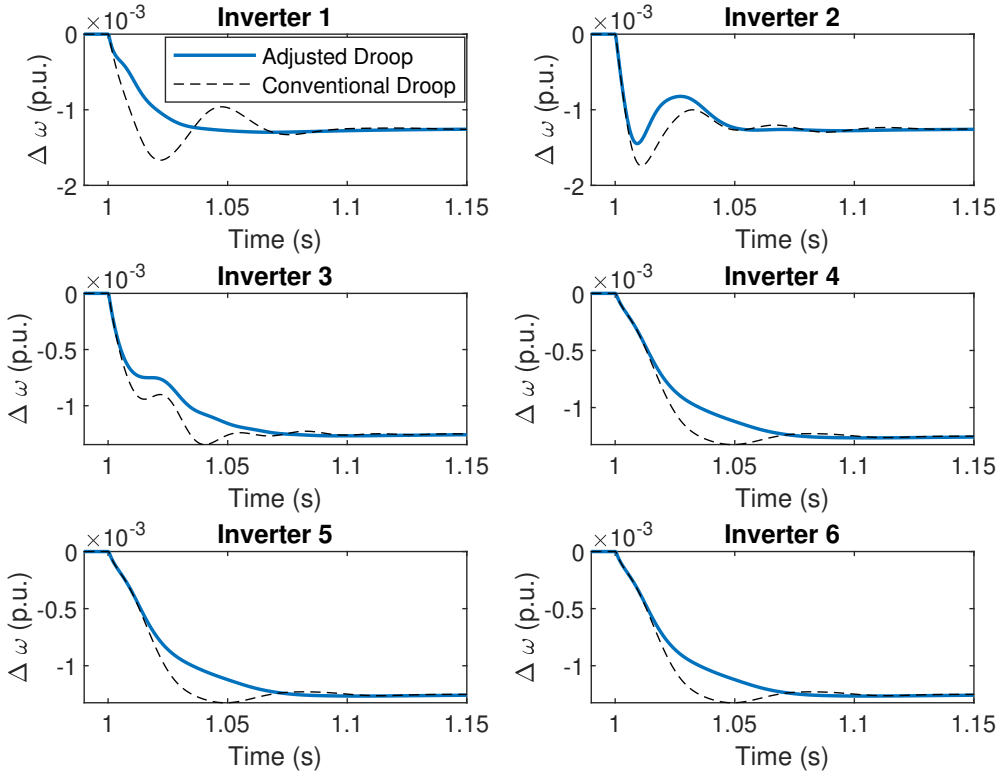


Figure A.14: Inverter frequency comparisons at each individual node, with and without droop adjustments. Results are for the full-model control synthesis; all generators are controlled

### A.2.2 Full-Model; Only Inverters 2, 3 Controlled

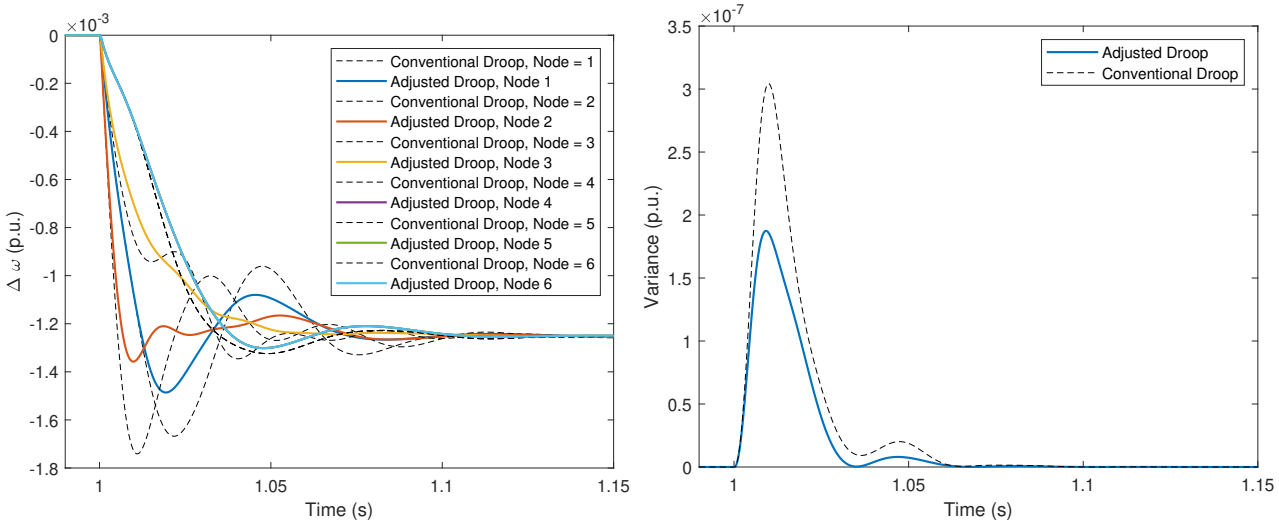


(a) Inverter output frequencies.

(b) Associated variance for inverter frequencies.

Figure A.15: Inverter output frequencies and associated variance for the full-model control synthesis; only inverters 2 and 3 have droop adjustments.

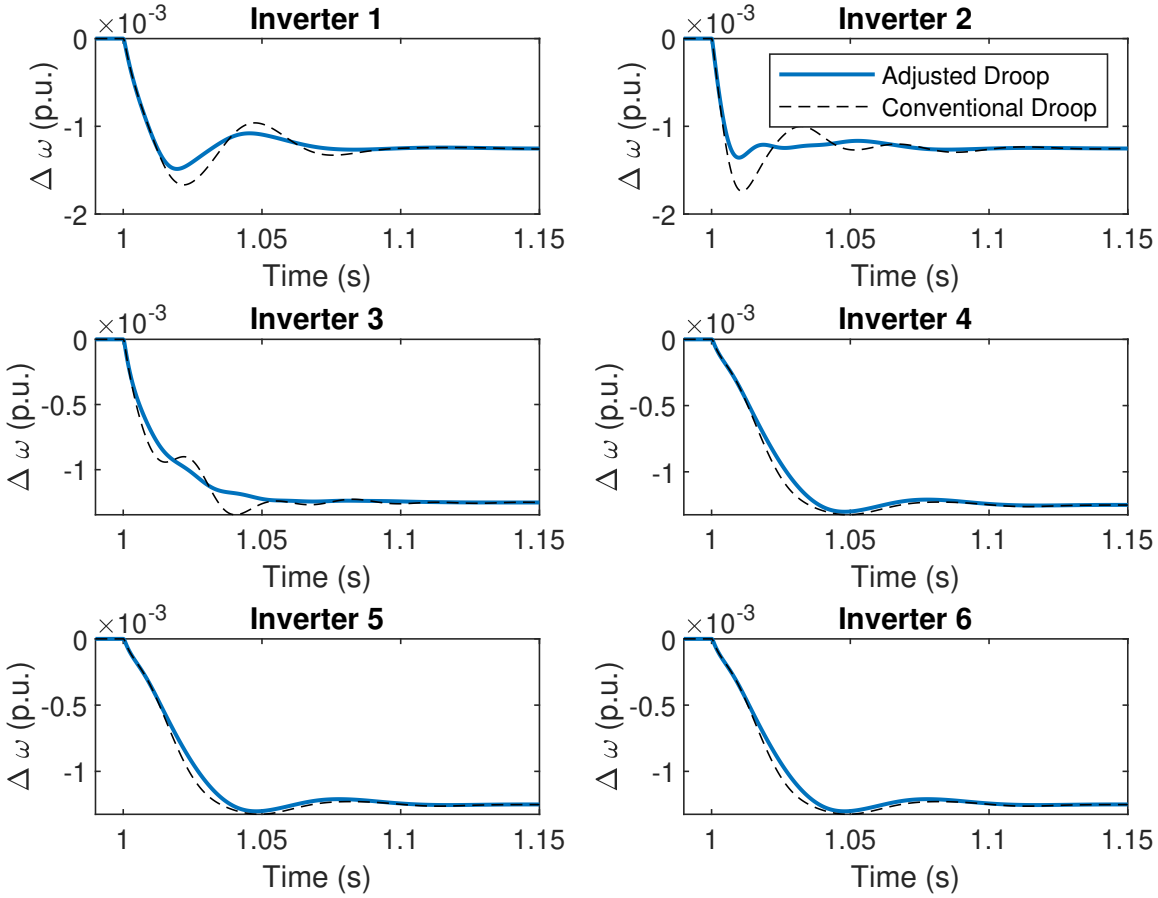


Figure A.16: Inverter frequency comparisons at each individual node, with and without droop adjustments. Results are for the full-model control synthesis; Only inverter 3 has droop adjustments

### A.2.3 Full-Model; Only Inverter 3 Controlled

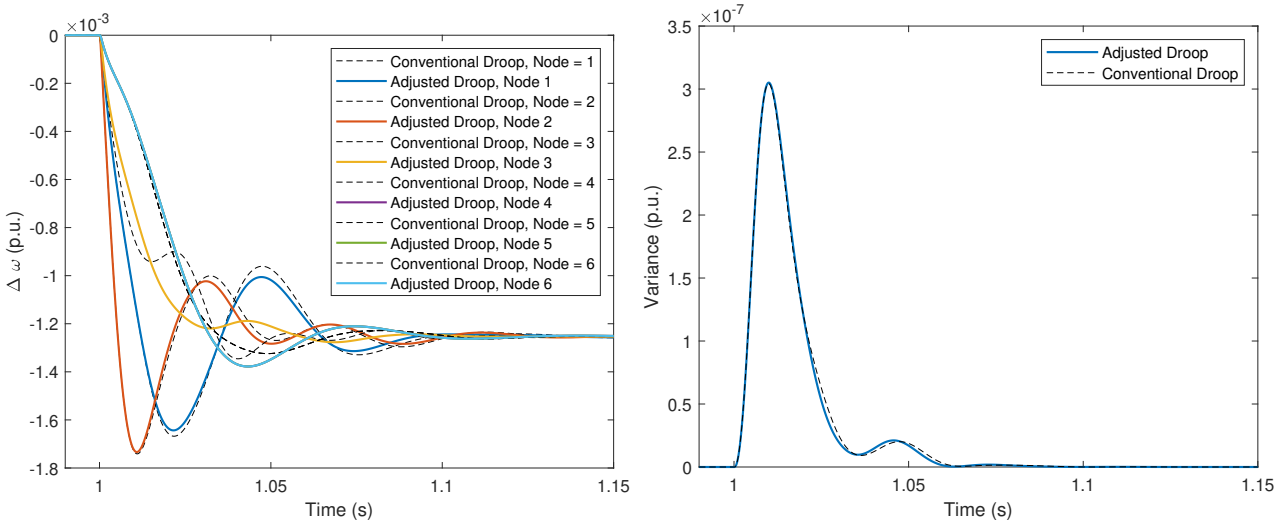


(a) Inverter output frequencies.

(b) Associated variance for inverter frequencies.

Figure A.17: Inverter output frequencies and associated variance for the full-model control synthesis; only inverter 3 has droop adjustments.

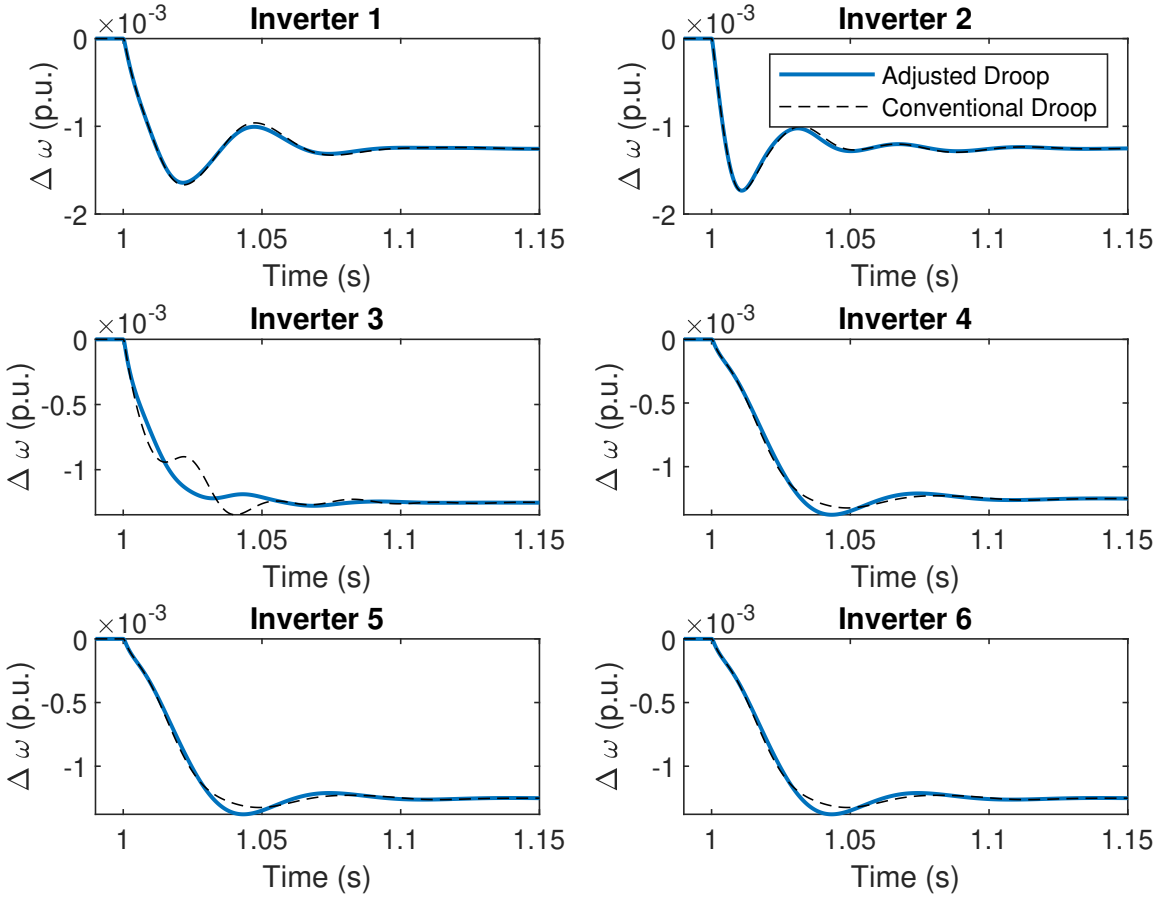


Figure A.18: Inverter frequency comparisons at each individual node, with and without droop adjustments. Results are for the full-model control synthesis; Only inverter 3 has droop adjustments

### A.2.4 Regional-Model; All Inverters Controlled

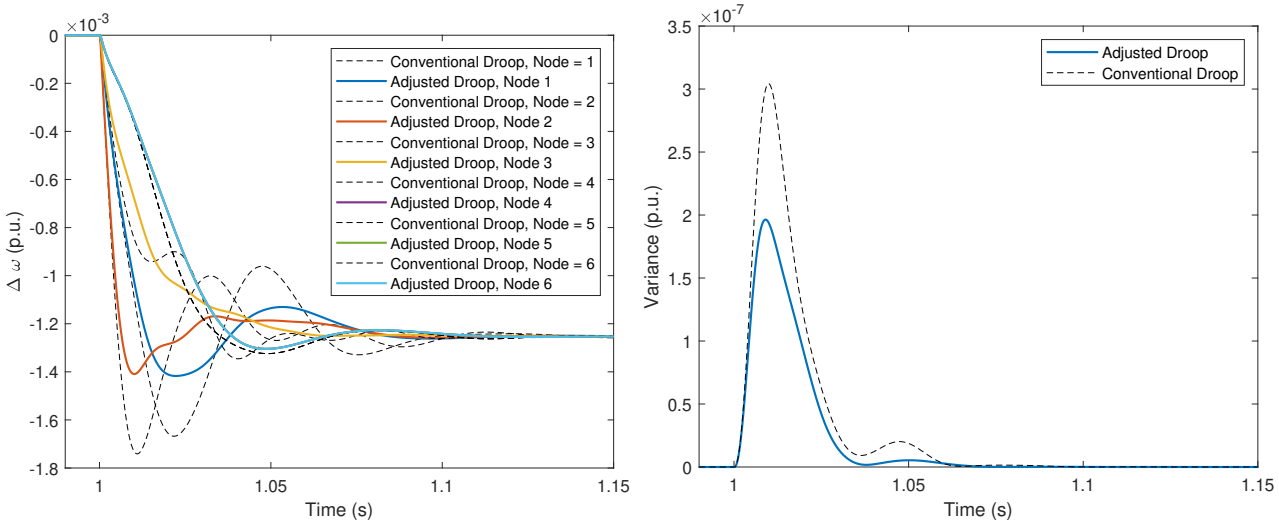


(a) Inverter output frequencies.

(b) Associated variance for inverter frequencies.

Figure A.19: Inverter output frequencies and associated variance for the regional-model control synthesis; all inverters have droop adjustments.

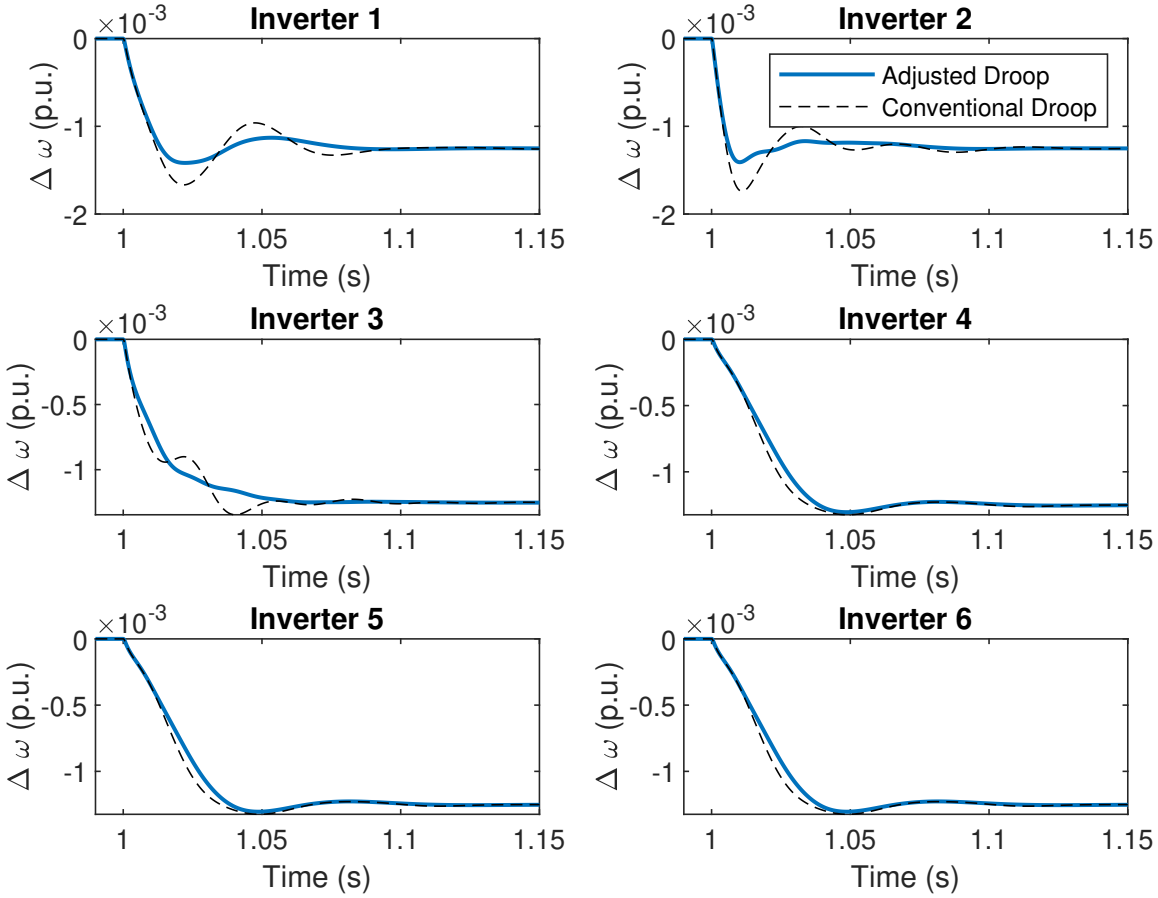


Figure A.20: Inverter frequency comparisons at each individual node, with and without droop adjustments. Results are for the regional-model control synthesis; all inverters have droop adjustments.

### A.2.5 Regional-Model; Inverters 2,3 Controlled

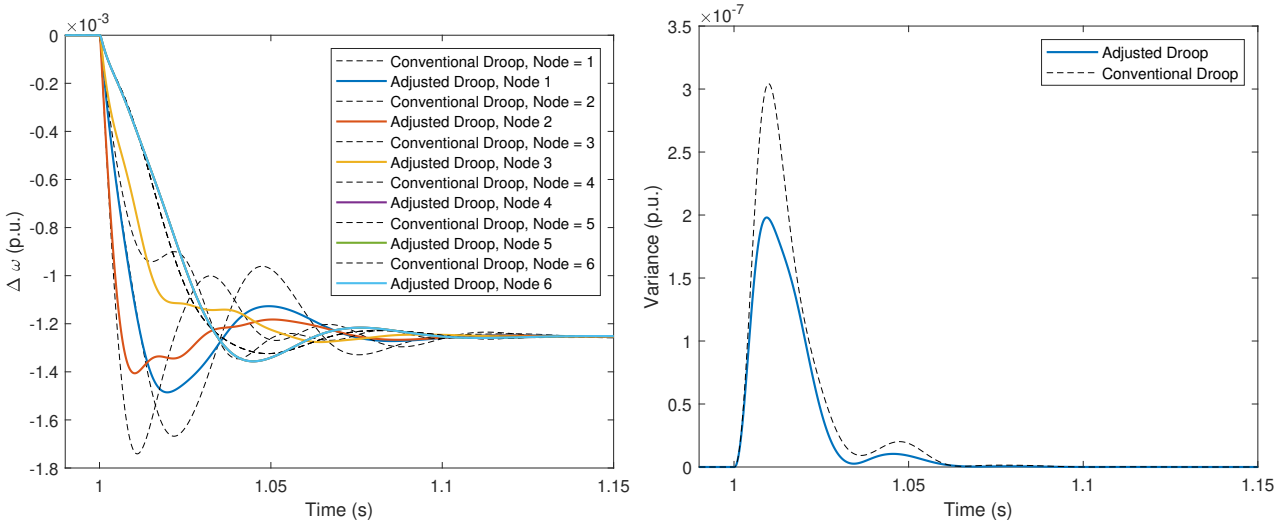


(a) Inverter output frequencies.

(b) Associated variance for inverter frequencies.

Figure A.21: Inverter output frequencies and associated variance for the regional-model control synthesis; only inverters 2 and 3 have droop adjustments.

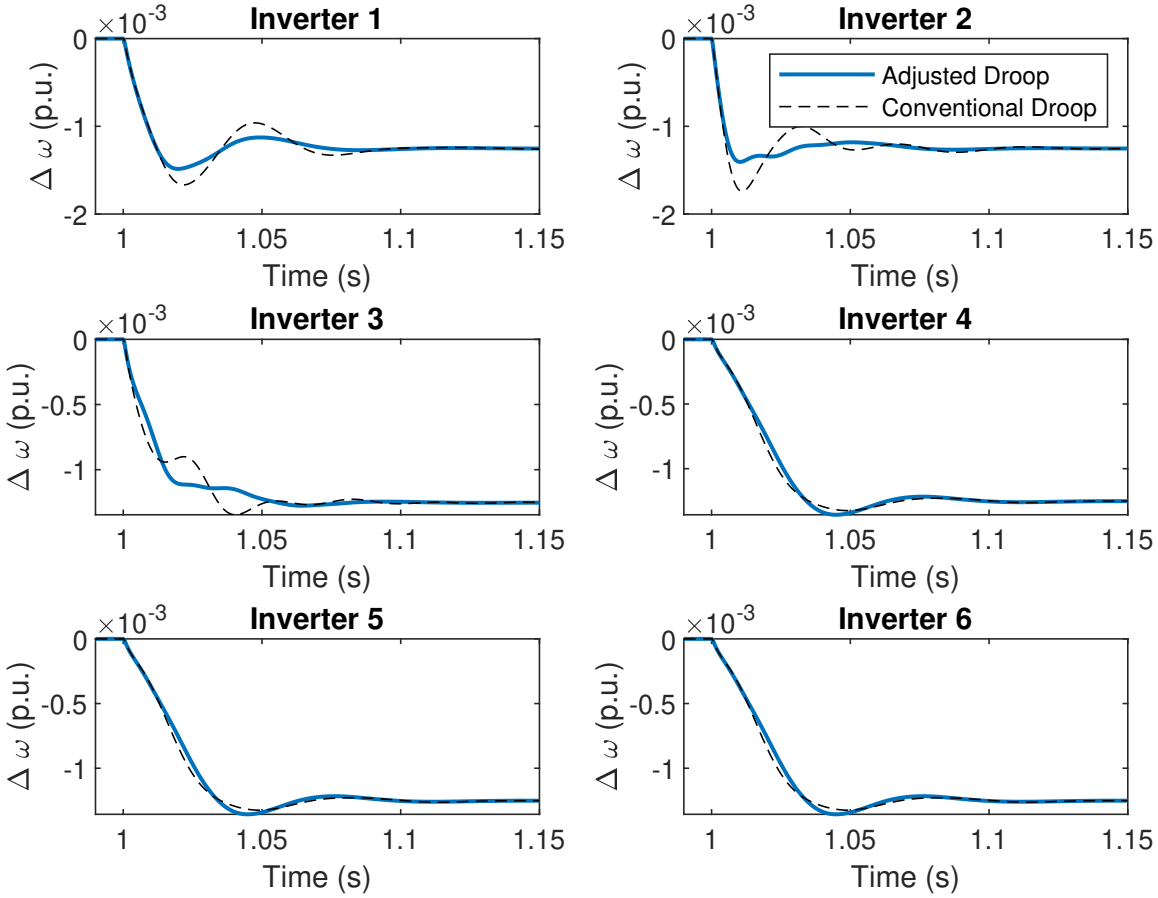


Figure A.22: Inverter frequency comparisons at each individual node, with and without droop adjustments. Results are for the regional-model control synthesis; only inverters 2 and 3 have droop adjustments.

### A.2.6 Solitary-Model; All Inverters Controlled

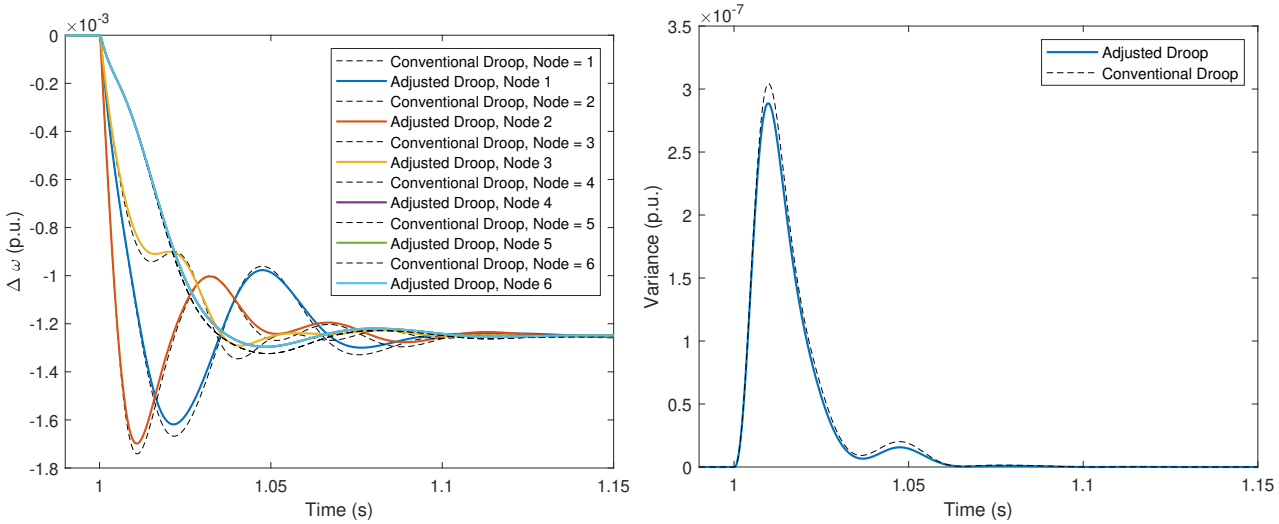


(a) Inverter output frequencies.

(b) Associated variance for inverter frequencies.

Figure A.23: Inverter output frequencies and associated variance for the solitary-model control synthesis; all inverters have droop adjustments.

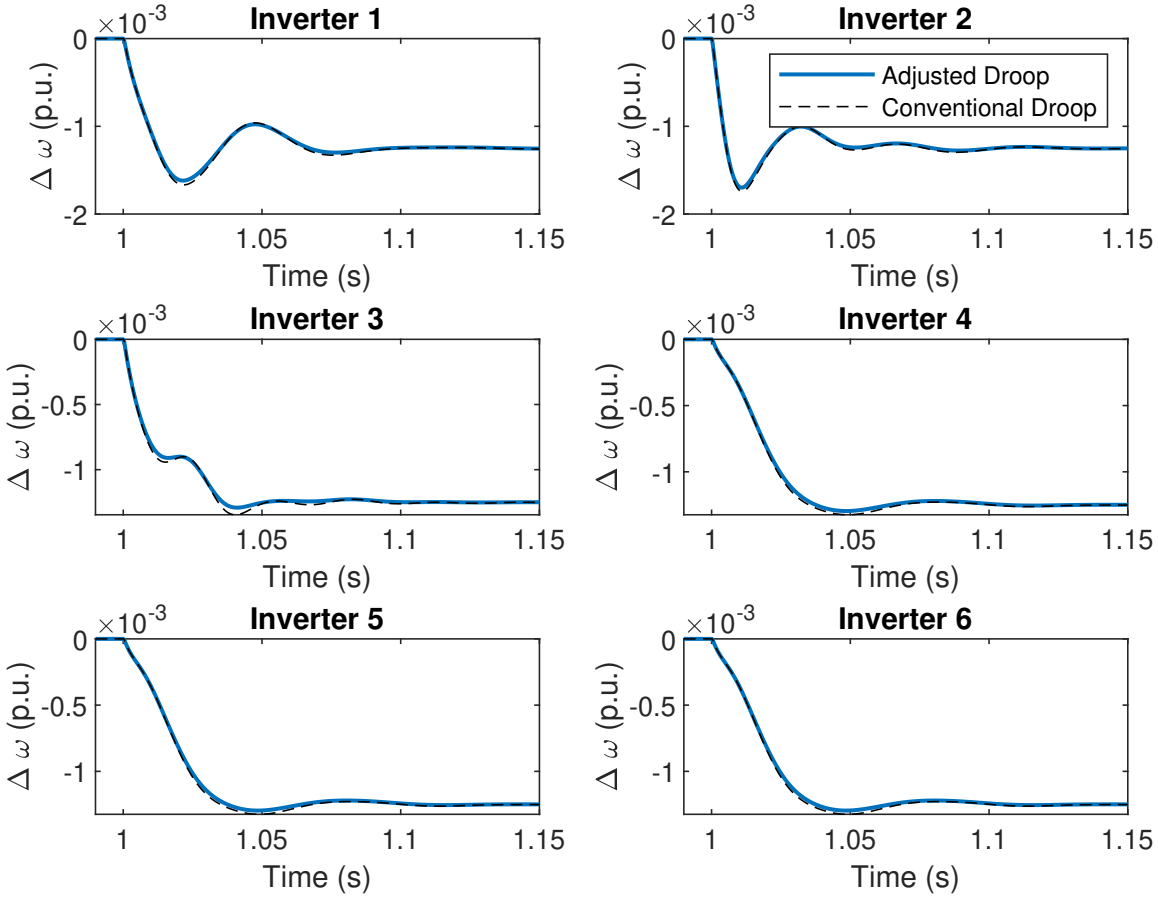


Figure A.24: Inverter frequency comparisons at each individual node, with and without droop adjustments. Results are for the solitary-model control synthesis; all inverters have droop adjustments.

## A.3 Configuration 3: Significant Variation at Node 3

In this case, we vary the droop gain at node 3 to simulate the condition in which this power source can provide 50% of the rated power of the other sources.

### A.3.1 Full-Model; All Inverters Controlled

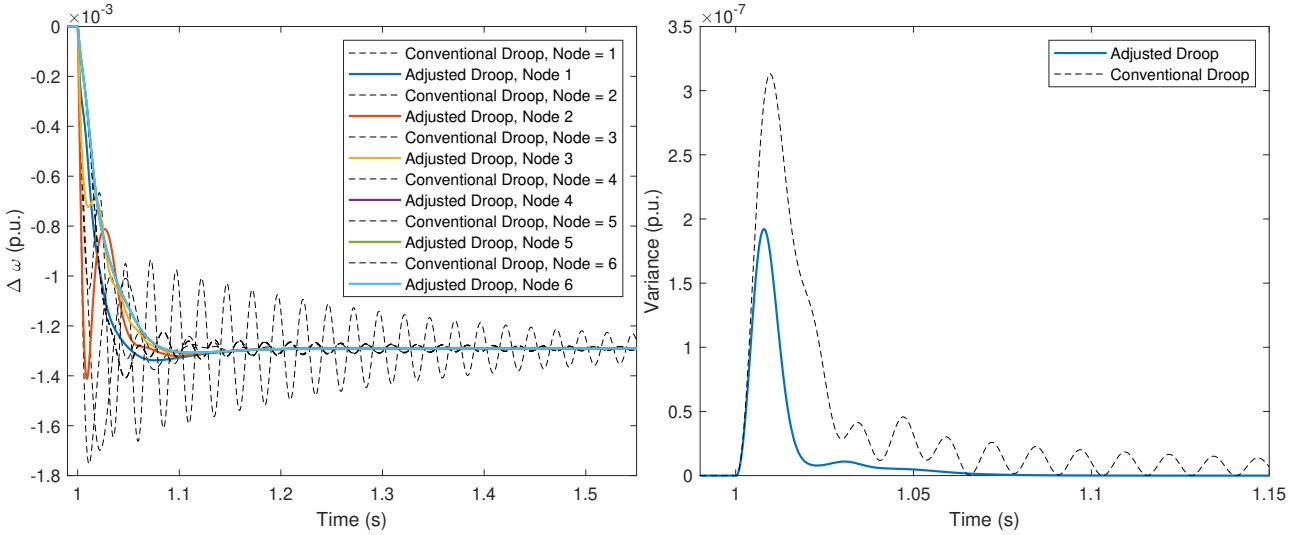


(a) Inverter output frequencies.

(b) Associated variance for inverter frequencies.

Figure A.25: Inverter output frequencies and associated variance for the full-model control synthesis; all generators are controlled.

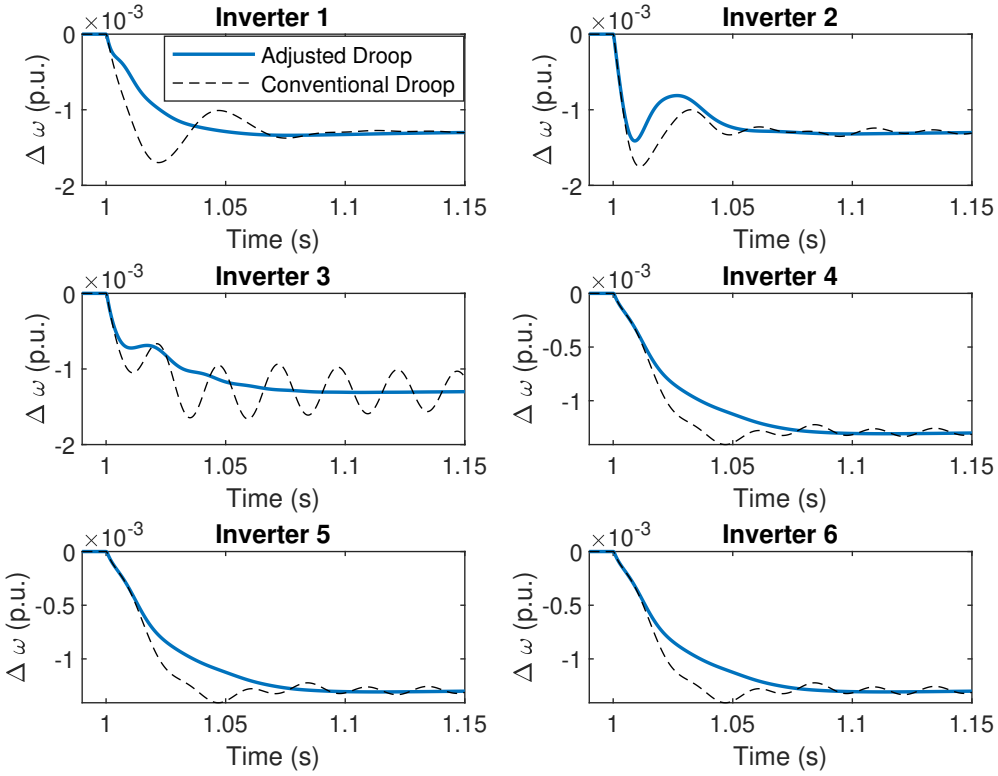


Figure A.26: Inverter frequency comparisons at each individual node, with and without droop adjustments. Results are for the full-model control synthesis; all generators are controlled

### A.3.2 Full-Model; Only Inverters 2, 3 Controlled

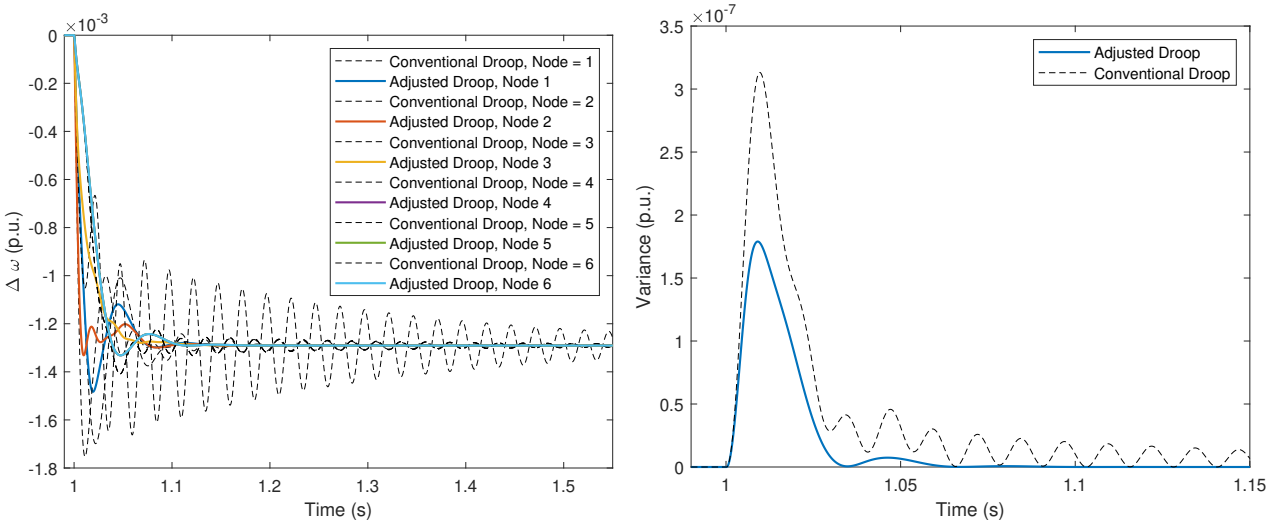


(a) Inverter output frequencies.

(b) Associated variance for inverter frequencies.

Figure A.27: Inverter output frequencies and associated variance for the full-model control synthesis; only inverters 2 and 3 have droop adjustments.

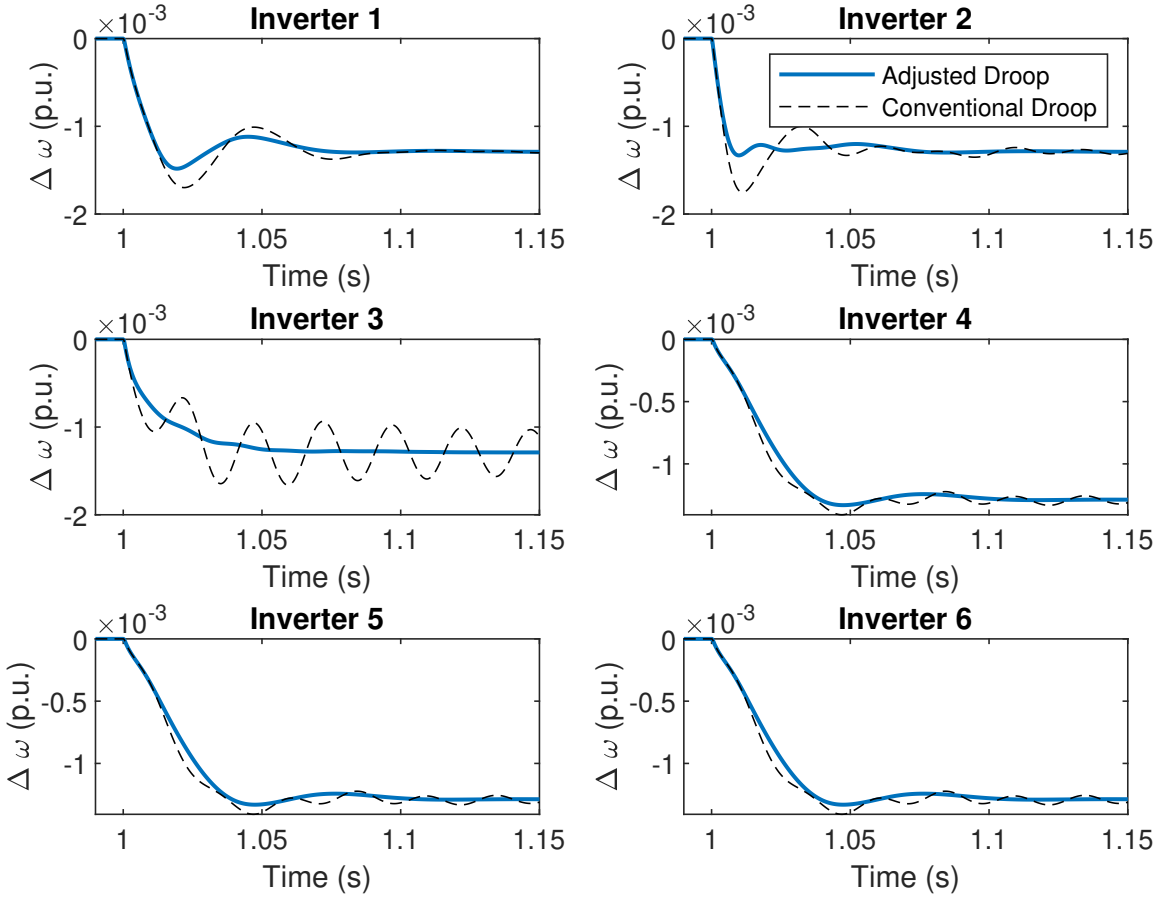


Figure A.28: Inverter frequency comparisons at each individual node, with and without droop adjustments. Results are for the full-model control synthesis; Only inverter 3 has droop adjustments

### A.3.3 Full-Model; Only Node 3 Controlled

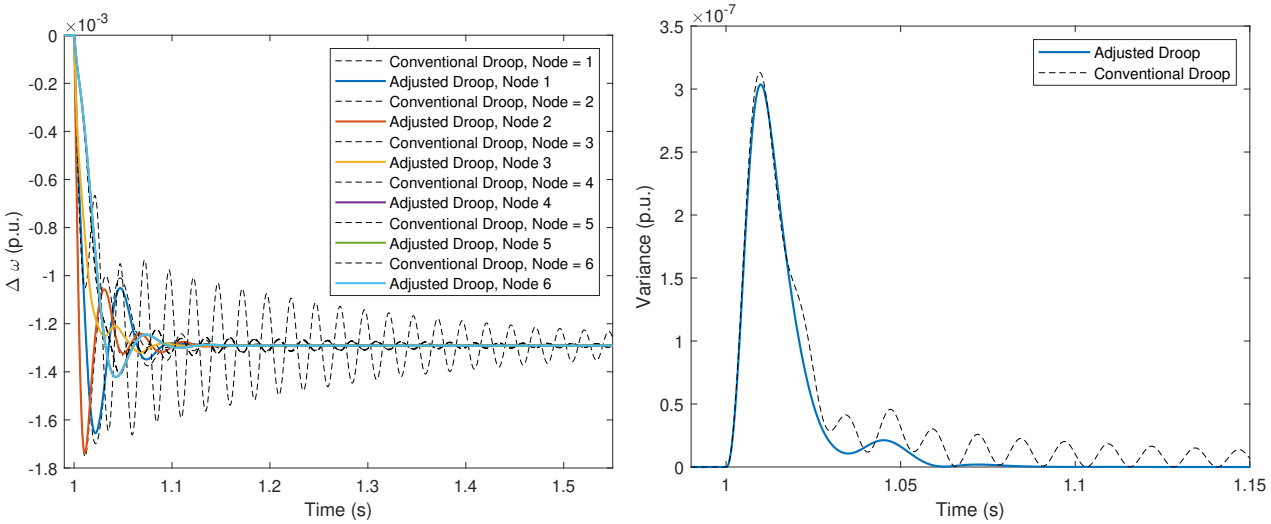


(a) Inverter output frequencies.

(b) Associated variance for inverter frequencies.

Figure A.29: Inverter output frequencies and associated variance for the full-model control synthesis; only inverter 3 has droop adjustments.

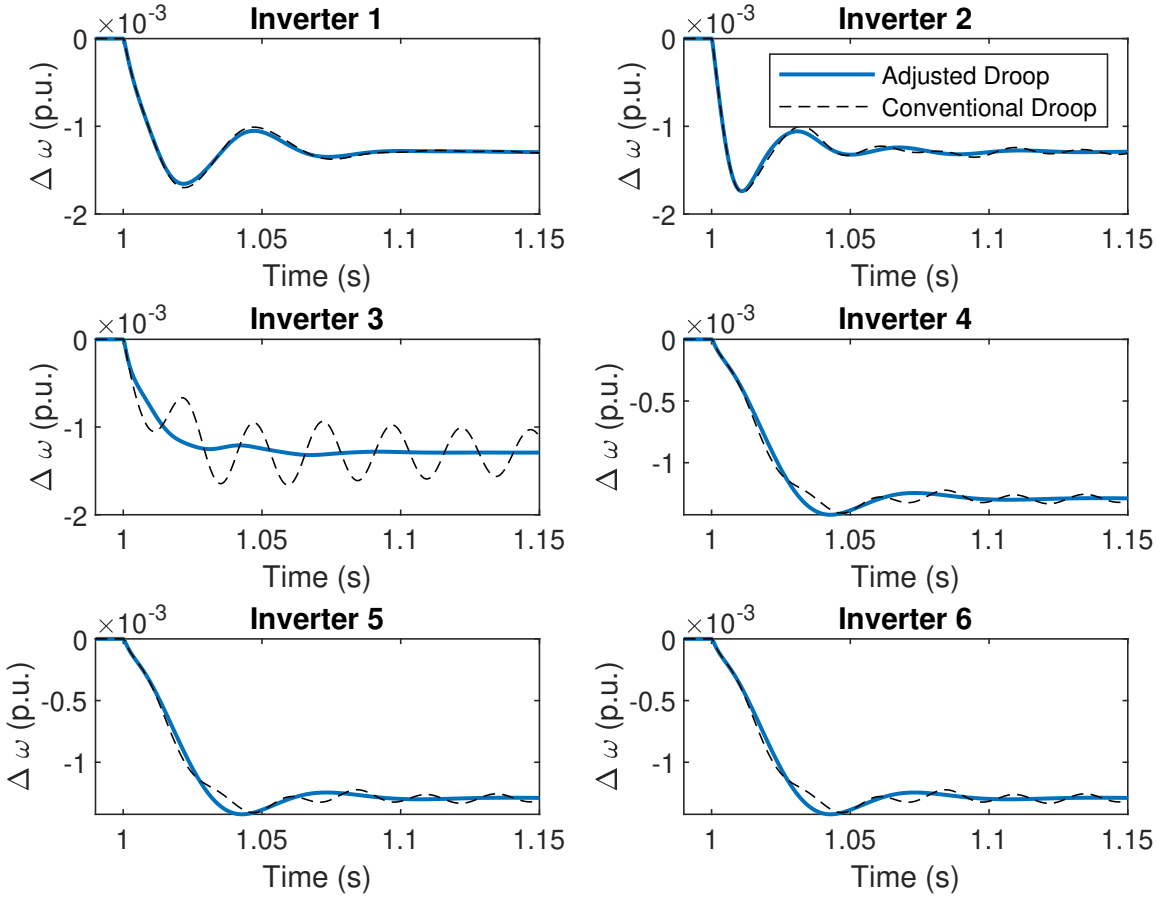


Figure A.30: Inverter frequency comparisons at each individual node, with and without droop adjustments. Results are for the full-model control synthesis; Only inverter 3 has droop adjustments

### A.3.4 Regional-Model; All Inverters Controlled

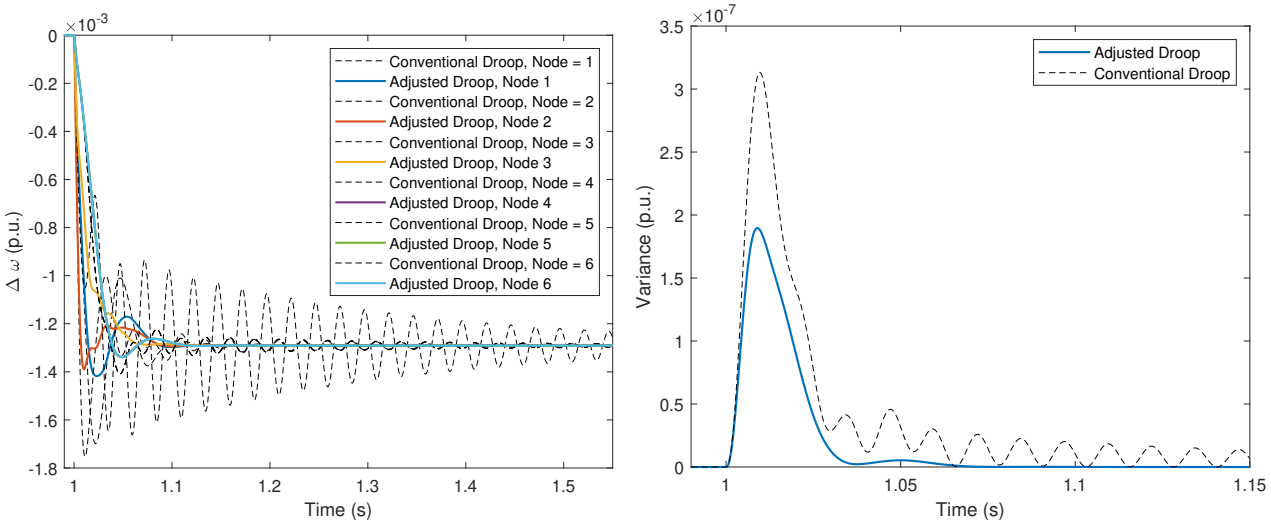


(a) Inverter output frequencies.

(b) Associated variance for inverter frequencies.

Figure A.31: Inverter output frequencies and associated variance for the regional-model control synthesis; all inverters have droop adjustments.

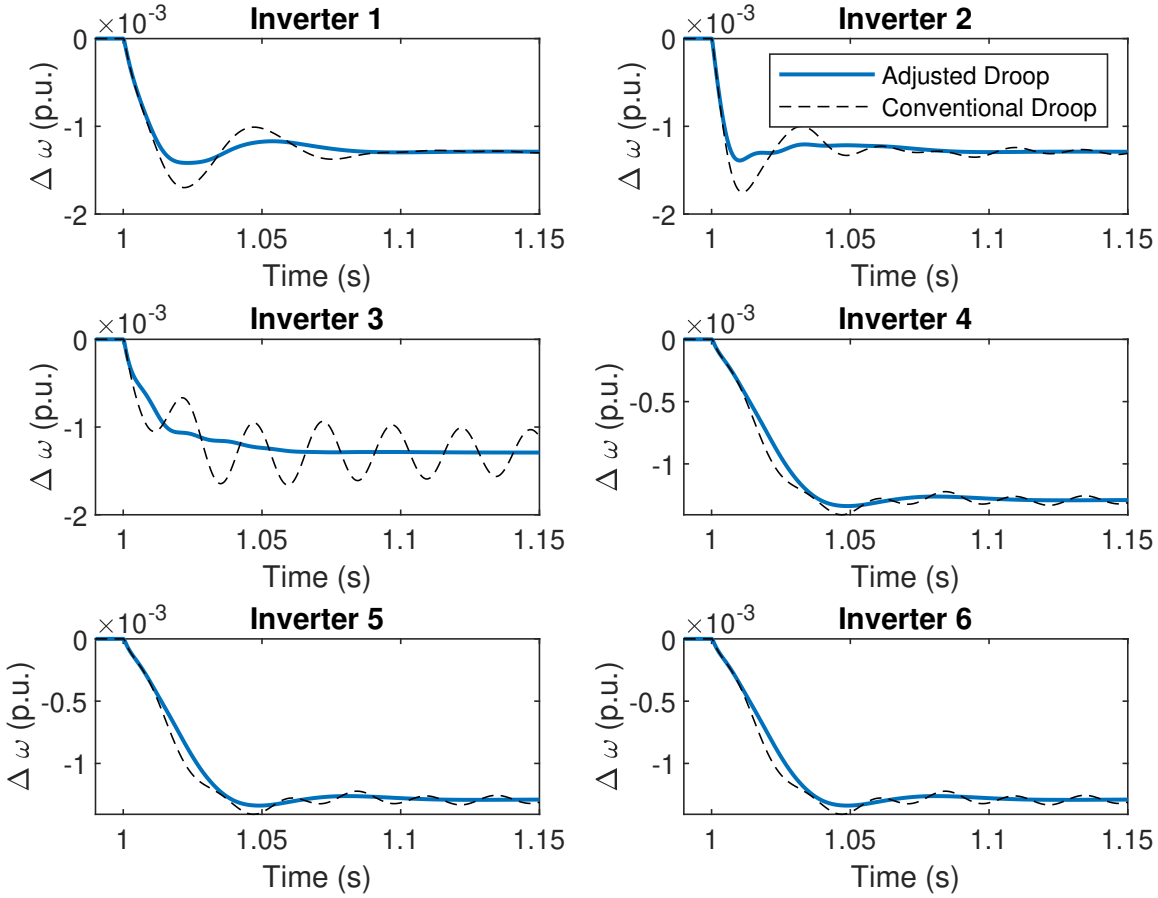


Figure A.32: Inverter frequency comparisons at each individual node, with and without droop adjustments. Results are for the regional-model control synthesis; all inverters have droop adjustments.

### A.3.5 Regional-Model; Inverters 2,3 Controlled

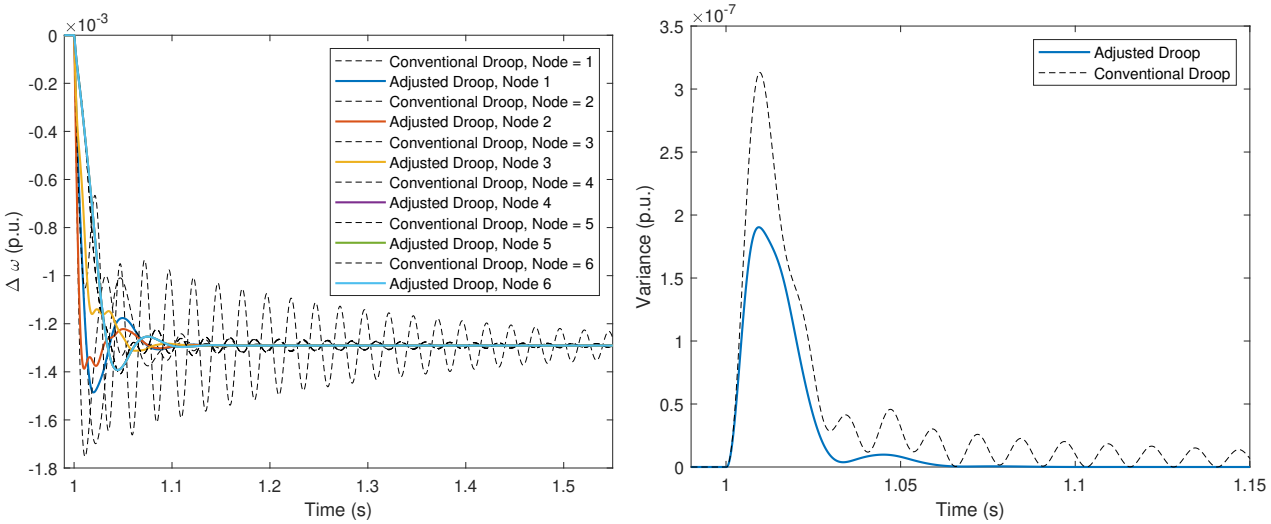


(a) Inverter output frequencies.

(b) Associated variance for inverter frequencies.

Figure A.33: Inverter output frequencies and associated variance for the regional-model control synthesis; only inverters 2 and 3 have droop adjustments.

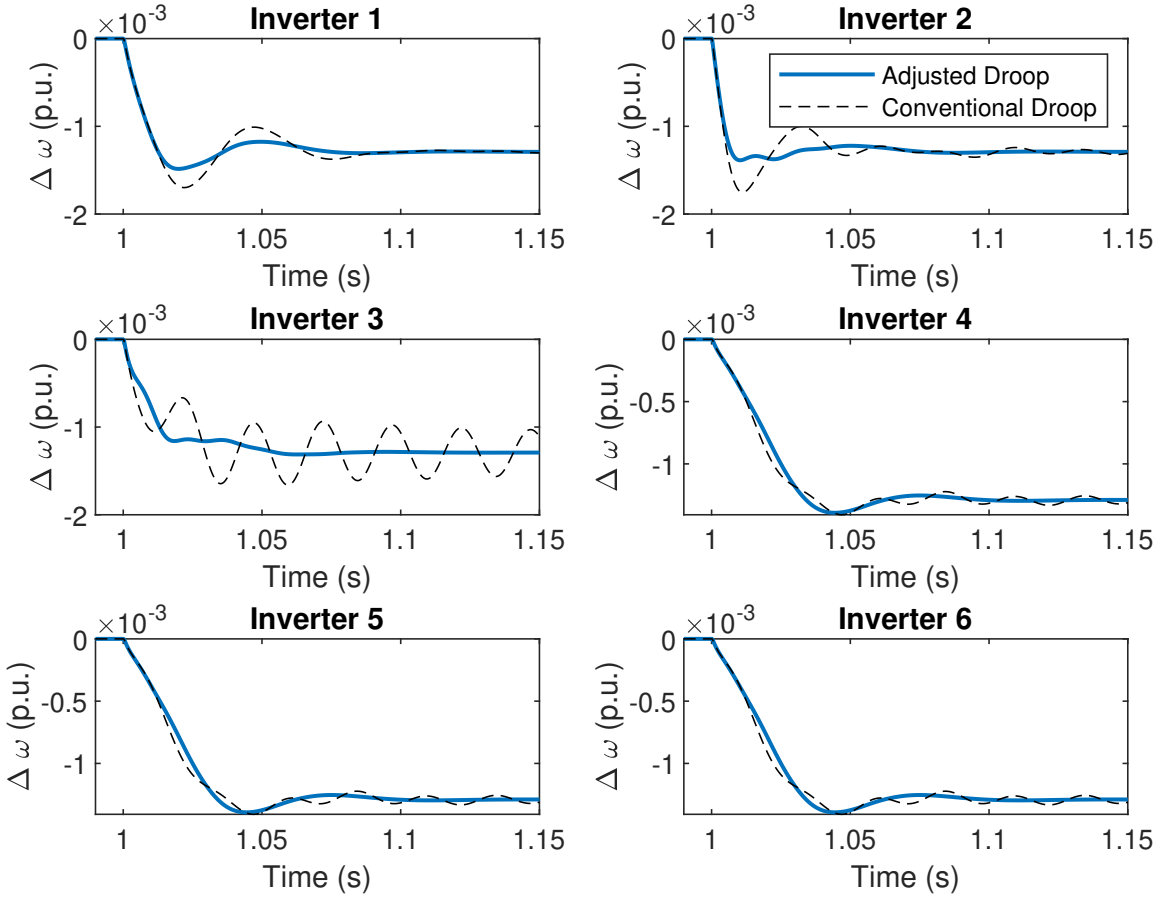


Figure A.34: Inverter frequency comparisons at each individual node, with and without droop adjustments. Results are for the regional-model control synthesis; only inverters 2 and 3 have droop adjustments.

### A.3.6 Solitary-Model; All Inverters Controlled

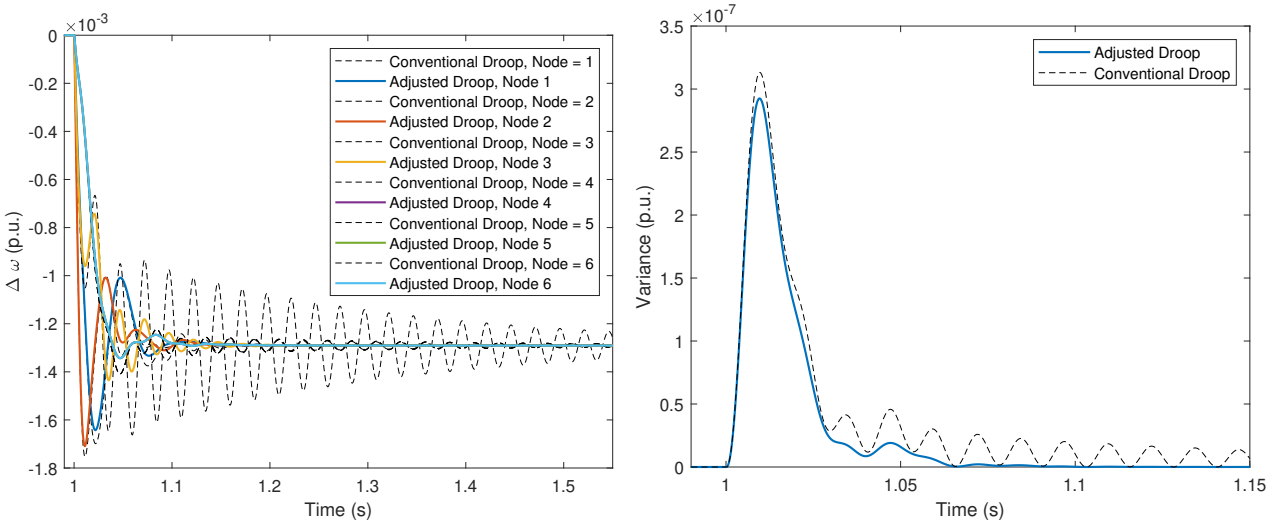


(a) Inverter output frequencies.

(b) Associated variance for inverter frequencies.

Figure A.35: Inverter output frequencies and associated variance for the solitary-model control synthesis; all inverters have droop adjustments.

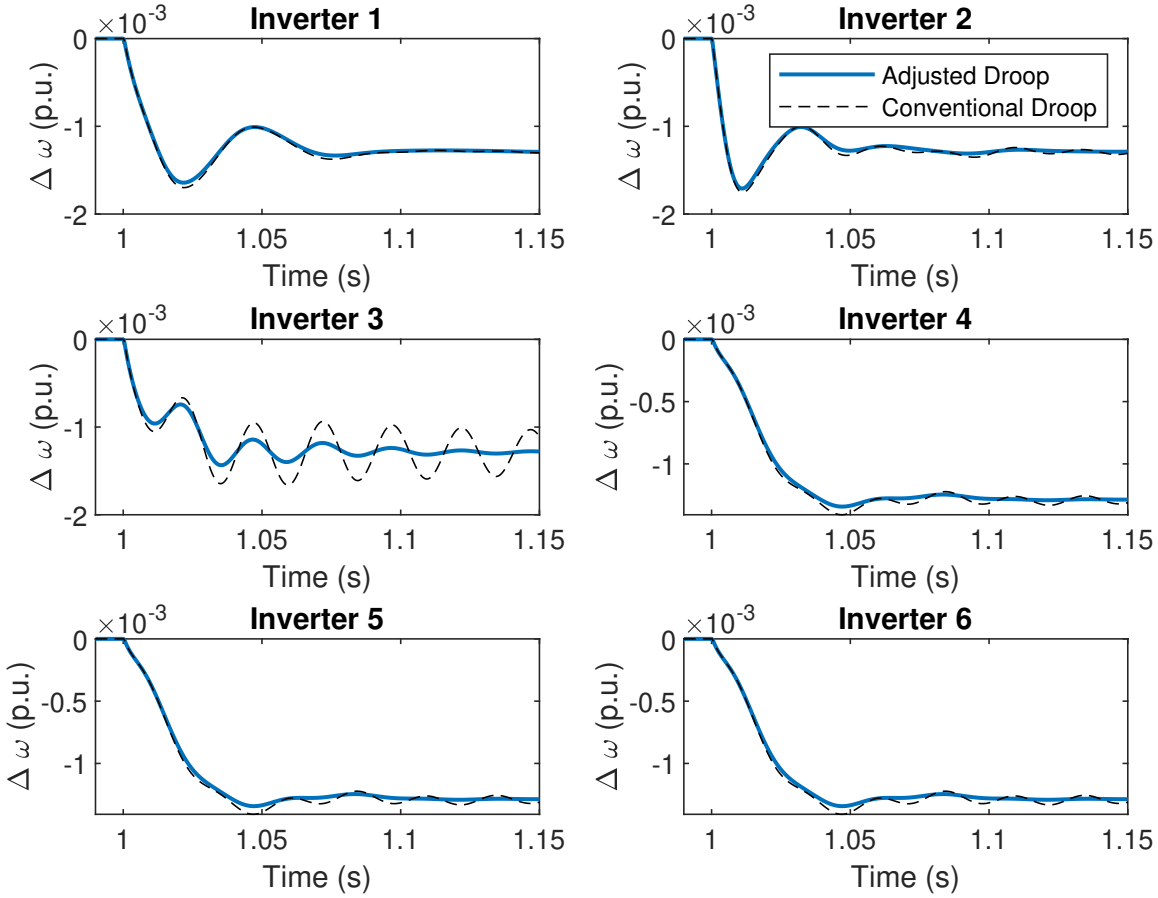


Figure A.36: Inverter frequency comparisons at each individual node, with and without droop adjustments. Results are for the solitary-model control synthesis; all inverters have droop adjustments.

# Bibliography

[1] N. Hatziargyriou, H. Asano, R. Iravani, and C. Marnay, "Microgrids: An Overview of Ongoing Research, Development, and Demonstration Projects," *IEEE Power and Energy Magazine*, pp. 78–94, 2007.

[2] R. H. Lasseter and P. Piagi, "Microgrid: A Conceptual Solution," p. 6, June 2004.

[3] A. Llaria, O. Curea, J. Jiménez, and H. Camblong, "Survey on microgrids: Unplanned islanding and related inverter control techniques," *Renewable Energy*, vol. 36, pp. 2052–2061, Aug. 2011.

[4] R. Lasseter, A. Akhil, C. Marnay, J. Stephens, J. Dagle, R. Guttromsom, A. S. Meliopoulous, R. Yinger, and J. Eto, "Integration of distributed energy resources. The CERTS Microgrid Concept," Tech. Rep. LBNL–50829, 799644, Apr. 2002.

[5] A. von Meier, *Electric Power Systems: A Conceptual Introduction.* Hoboken, New Jersey: John Wiley & Sons, 2006.

[6] A. Ulbig, T. S. Borsche, and G. Andersson, "Impact of Low Rotational Inertia on Power System Stability and Operation," *IFAC Proceedings Volumes*, vol. 47, no. 3, pp. 7290–7297, 2014.

[7] H. Gu, R. Yan, and T. K. Saha, "Minimum Synchronous Inertia Requirement of Renewable Power Systems," *IEEE Transactions on Power Systems*, vol. 33, pp. 1533–1543, Mar. 2018.

[8] F. Katiraei, M. Iravani, and P. Lehn, "Micro-Grid Autonomous Operation During and Subsequent to Islanding Process," *IEEE Transactions on Power Delivery*, vol. 20, pp. 248–257, Jan. 2005.

[9] KEMA, "Microgrids- Benefits, Models, Barriers, and Suggested Policy Initiatives for the Commonwealth of Massachusetts," technical Report, Massachusetts Clean Energy Center, Feb. 2014.

[10] M. Kelly, "Two Years After Hurricane Sandy, Recognition of Princeton's Microgrid Still Surges," *Princeton Office of Communications*, Oct. 2014.

[11] N. Pogaku, M. Prodanovic, and T. C. Green, "Modeling, Analysis, and Testing of Autonomous Operation of an Inverter-Based MIcrogrid," *IEEE Transactions on Power Electronics*, vol. 22, pp. 613–626, Mar. 2007.

[12] Y. Levron, J. Belikov, and D. Baimel, "A Tutorial on Dynamics and Control of Power Systems with Distributed and Renewable Energy Sources Based on the DQ0 Transformation," *Applied Sciences*, vol. 8, p. 1661, Sept. 2018.

[13] M. Yazdanian and A. Mehrizi-Sani, "Distributed Control Techniques in Microgrids," *IEEE Transactions on Smart Grid*, vol. 5, pp. 2901–2909, Nov. 2014.

[14] D. D. Siljak, *Decentralized Control of Complex Systems*. Academic Press, 1991.

[15] J. Guerrero, L. GarciadeVicuna, J. Matas, M. Castilla, and J. Miret, "A Wireless Controller to Enhance Dynamic Performance of Parallel Inverters in Distributed Generation Systems," *IEEE Transactions on Power Electronics*, vol. 19, pp. 1205–1213, Sept. 2004.

[16] N. M. Dehkordi, N. Sadati, and M. Hamzeh, "Robust tuning of transient droop gains based on Kharitonov's stability theorem in droop-controlled microgrids," *IET Generation, Transmission & Distribution*, vol. 12, pp. 3495–3501, Aug. 2018.

[17] M. Hassanzahraee and A. Bakhshai, "Transient droop control strategy for parallel operation of voltage source converters in an islanded mode microgrid," in *2011 IEEE 33rd International Telecommunications Energy Conference (INTELEC)*, (Amsterdam, Netherlands), pp. 1–9, IEEE, Oct. 2011.

[18] Y. Mohamed and E. El-Saadany, "Adaptive Decentralized Droop Controller to Preserve Power Sharing Stability of Paralleled Inverters in Distributed Generation Microgrids," *IEEE Transactions on Power Electronics*, vol. 23, pp. 2806–2816, Nov. 2008.

[19] C. A. Canizares, D. E. Olivares, A. Mehiziri-Sani, A. H. Etemadi, R. Iravani, M. Kazerani, A. H. Hajimiragha, O. Gomis-Bellmunt, M. Saeedifard, R. Palma-Behnke, G. A. Jimenez-Estevez, and N. Hatziargyriou, "Trends in Microgrid Control," *IEEE Transactions on Smart Grid*, 2014.

[20] Z. Jiang and X. Yu, "Active Power-Voltage Control Scheme for Islanding Operation of Inverter-Interfaced Microgrids," *IEEE Power and Energy Society General Meeting*, 2009.

[21] W. Huang, M. Lu, and L. Zhang, "Survey on Microgrid Control," *Energy Procedia*, 2011.

[22] M. Prodanovic, T. Green, and H. Mansir, "A survey of control methods for three phase inverters in parallel connection," *Power Electronics and Variable Speed Drives*, 2000.

[23] N. Cai and J. Mitra, "A multi-level control architecture for master-slave organized microgrids with power electronic interfaces," *Electric Power Systems Research*, 2014.

[24] H. Bevrani, M. R. Feizi, and S. Ataee, "Robust Frequency Control in an Islanded Microgrid: H$\infty$ and $\mu$-Synthesis Approaches," *IEEE Transactions on Smart Grid*, pp. 1–1, 2015.

[25] G. Weiss, Q.-C. Zhong, T. Green, and J. Liang, "H-Infinity Repetitive Control of DC-AC Converters in Microgrids," *IEEE Transactions on Power Electronics*, vol. 19, pp. 219–230, Jan. 2004.

[26] T.-S. Lee and Chang, Jhy-Ming, "H-Infinity Loop-Shaping Controller Designs for the Single-Phase UPS Inverters," *IEEE TRANSACTIONS ON POWER ELECTRONICS*, vol. 16, no. 4, p. 9, 2001.

[27] K. Masui and T. Namerikawa, "Load frequency control of a microgrid based on H$\infty$ control considering response speed of generators," in *2015 54th IEEE Conference on Decision and Control (CDC)*, (Osaka), pp. 5895–5902, IEEE, Dec. 2015.

[28] Tomonobu Senjyu, Motoki Tokudome, Atsushi Yona, Hideomi Sekine, Toshihisa Funabashi, and Chul-Hwan Kim, "A frequency control approach by decentralized generators and loads in power systems," in *2008 IEEE 2nd International Power and Energy Conference*, (Johor Bahru, Malaysia), pp. 79–84, IEEE, Dec. 2008.

[29] V. P. Singh, S. R. Mohant, N. Kishor, and P. K. Ray, "Robust $H_\infty$ load frequency control in hybrid distributed generation system," *Electrical Power and Energy Systems*, vol. 46, pp. 294–305, Nov. 2013.

[30] Z. Ma, Z. Yan, M. L. Shaltout, and D. Chen, "Optimal Real-Time Control of Wind Turbine During Partial Load Operation," *IEEE Transactions on Control Systems Technology*, vol. 23, pp. 2216–2226, Nov. 2015.

[31] A. D. Hansen, "Evaluation of power control with different electrical and control concept of wind farm: Part2 – Large systems.," *Project Upwind*, p. 93.

[32] T. Ackermann, *Wind Power in Power Systems*. John Wiley & Sons, 2005.

[33] J. Aho, A. Buckspan, J. Laks, P. Fleming, Yunho Jeong, F. Dunne, M. Churchfield, L. Pao, and K. Johnson, "A tutorial of wind turbine control for supporting grid frequency through active power control," in *2012 American Control Conference (ACC)*, (Montreal, QC), pp. 3120–3131, IEEE, June 2012.

[34] T. L. Department, "Wind Farm Transmission Grid Code Provisions: A Direction by the Commission for Energy Regulation," technical Report, Commission for Energy Regulation, Dublin, Ireland, 2004.

[35] "Wind Turbines Connected to Grids with Voltages Below 100 kV: Technical Regulations for the Properties and the Control of Wind Turbines," technical Report, Elkraft System and Eltra, Erritso, Denmark, 2003.

[36] "Technical Requirements for the Connection of Generation Facilities to the Hydro-Quebec Transmission System: Supplementary Requirements for Wind Generation," technical Report, Hydro-Quebec, Quebec, Canada, 2005.

[37] J. Morren, S. de Haan, W. Kling, and J. Ferreira, "Wind Turbines Emulating Inertia and Supporting Primary Frequency Control," *IEEE Transactions on Power Systems*, vol. 21, pp. 433–434, Feb. 2006.

[38] J. Morren, S. de Haan, and J. Ferreira, "Primary power/frequency control with wind turbines and fuel cells," in *2006 IEEE Power Engineering Society General Meeting*, (Montreal, Que., Canada), p. 8 pp., IEEE, 2006.

[39] R. G. de Almeida and J. A. Pecas Lopes, "Participation of Doubly Fed Induction Wind Generators in System Frequency Regulation," *IEEE Transactions on Power Systems*, vol. 22, pp. 944–950, Aug. 2007.

[40] E. Loukarakis, I. Margaris, and P. Moutis, "Frequency control support and participation methods provided by wind generation," in *2009 IEEE Electrical Power Energy Conference (EPEC)*, pp. 1–6, Oct. 2009.

[41] K. V. Vidyanandan and N. Senroy, "Primary frequency regulation by deloaded wind turbines using variable droop," *IEEE Transactions on Power Systems*, vol. 28, pp. 837–846, May 2013.

[42] H. Bevrani, A. Ghosh, and G. Ledwich, "Renewable energy sources and frequency regulation: Survey and new perspectives," *IET Renewable Power Generation*, vol. 4, no. 5, p. 438, 2010.

[43] J. W. Choi, S. Y. Heo, and M. K. Kim, "Hybrid operation strategy of wind energy storage system for power grid frequency regulation," *Transmission Distribution IET Generation*, vol. 10, no. 3, pp. 736–749, 2016.

[44] G. He, Q. Chen, C. Kang, Q. Xia, and K. Poolla, "Cooperation of Wind Power and Battery Storage to Provide Frequency Regulation in Power Markets," *IEEE Transactions on Power Systems*, vol. 32, pp. 3559–3568, Sept. 2017.

[45] Liang Liang, Jin Zhong, and Zaibin Jiao, "Frequency regulation for a power system with wind power and battery energy storage," in *2012 IEEE International Conference on Power System Technology (POWERCON)*, (Auckland), pp. 1–6, IEEE, Oct. 2012.

[46] L. Johnston, F. Díaz-González, O. Gomis-Bellmunt, C. Corchero-García, and M. Cruz-Zambrano, "Methodology for the economic optimisation of energy storage systems for frequency support in wind power plants," *Applied Energy*, vol. 137, pp. 660–669, Jan. 2015.

[47] A. Gelb, J. F. Kasper, R. A. Nash, C. F. Price, and A. A. Sutherland, *Applied Optimal Estimation*. Cambridge, Massachusetts: M.I.T. Press, 1974.

[48] J. P. Hespanha, *Linear Systems Theory*. Princeton University Press, 2009.

[49] P. S. Maybeck, *Stochastic Models, Estimation, and Control; Volume 1*. Academic Press, 1979.

[50] R. M. Murray, *Optimization Based Control*. California Institute of Technology, 2011.

[51] F. C. Schweppe and J. Wildes, "Power System Static-State Estimation, Part I: Exact Model," *IEEE TRANSACTIONS ON POWER APPARATUS AND SYSTEMS*, p. 6, 1970.

[52] A. Gomez-Exposito, A. Abur, A. de la Villa Jaen, and C. Gomez-Quiles, "A Multilevel State Estimation Paradigm for Smart Grids," *Proceedings of the IEEE*, vol. 99, pp. 952–976, June 2011.

[53] G. N. Korres, N. D. Hatziargyriou, and P. J. Katsikas, "State estimation in Multi-Microgrids," p. 23, 2010.

[54] Y.-F. Huang, S. Werner, J. Huang, N. Kashyap, and V. Gupta, "State Estimation in Electric Power Grids: Meeting New Challenges Presented by the Requirements of the Future Grid," *IEEE Signal Processing Magazine*, vol. 29, pp. 33–43, Sept. 2012.

[55] A. Leite da Silva, M. Do Coutto Filho, and J. de Queiroz, "State forecasting in electric power systems," *IEE Proceedings C Generation, Transmission and Distribution*, vol. 130, no. 5, p. 237, 1983.

[56] N. Kashyap, S. Werner, T. Riihonen, and Y.-F. Huang, "Reduced-order synchrophasor-assisted state estimation for smart grids," in *2012 IEEE Third International Conference on Smart Grid Communications (SmartGridComm)*, (Tainan, Taiwan), pp. 605–610, IEEE, Nov. 2012.

[57] M. Rana and L. Li, "An Overview of Distributed Microgrid State Estimation and Control for Smart Grids," *Sensors*, vol. 15, pp. 4302–4325, Feb. 2015.

[58] M. Rana, L. Li, and S. Su, "Kalman filter based microgrid state estimation and control using the IoT with 5G networks," in *2015 IEEE PES Asia-Pacific Power and Energy Engineering Conference (APPEEC)*, (Brisbane, Australia), pp. 1–5, IEEE, Nov. 2015.

[59] M. Chu Cheong, P. Du, and D. Chen, "Decentralized H-Infinity Control to Mitigate Renewable Intermittency," in *ASME Dynamic Systems and Control Conference*, (Minneapolis, MN), Oct. 2016.

[60] M. Chu Cheong, P. Du, and D. Chen, "Distributed H-Infinity Frequency Control for Inverter-Connected Microgrids," in *ASME Dynamic Systems and Control Conference*, (Tysons Corner, VA), Oct. 2017.

[61] A. H. Etemad, E. J. Davison, and R. Iravani, "A Decentralized Robust Control Strategy for Multi-DER Microgrids-Part I: Fundamental Concepts," *IEEE Transactions on Power Delivery*, vol. 27, pp. 1843–1853, Oct. 2012.

[62] A. Stoorvogel, *The H-Infinity Control Problem: A State Space Approach*. PhD thesis, University of Michigan, Ann Arbor, Feb. 2000.

[63] S. Boyd, L. E. Ghaoui, E. Feron, and V. Balakrishnan, *Linear Matrix Inequalities in System and Control Theory*. SIAM, 1994.

[64] C. A. R. Crusius and A. Trofino, "Sufficient LMI Conditions for Output Feedback Control Problems," *IEEE Transactions on Automatic Control*, vol. 44, pp. 1053–1057, May 1999.

[65] J. Rubio-Massegu, J. Rossell, H. Karimi, and F. Palacios-Quinonero, "Static output-feedback control under information structure constraints," *Automatica*, vol. 49, pp. 313–316, Jan. 2013.

[66] F. Palacios-Quinonero, J. Rubio-Massegu, J. Rossell, and H. Karimi, "Recent Advances in Static Output-Feedback Controller Design with Applications to Vibration Control

of Large Structures," *Modeling, Identification and Control*, vol. 35, no. 3, pp. 169–190, 2014.

[67] M. Chu Cheong, H. Qian, J. Conger, D. Chen, and P. Du, "Distributed H-Infinity Frequency Control for Inverter Connected Microgrids," in *ASME Dynamic Systems and Control Conference*, (Tysons, Virginia, USA), ASME, Oct. 2017.

[68] A. Zecevic and D. Siljak, "Design of Robust Static Output Feedback for Large-Scale Systems," *IEEE Transactions on Automatic Control*, vol. 49, pp. 2040–2044, Nov. 2004.

[69] J. Löfberg, "YALMIP: A Toolbox for Modeling and Optimization in MATLAB," in *Proceedings of the CACSD Conference*, (Taipei, Taiwan), 2004.

[70] R. Tutuncu, K. Toh, and M. Todd, "Solving Semidefinite-Quadratic-Linear Programs using SDPT3," *Mathematical Programming Series B*, vol. 95, pp. 189–217, 2003.

[71] M. Chu Cheong, Z. Ma, H. Qian, J. Conger, P. Du, and D. Chen, "Wind Turbine Participation in Primary Frequency Control," *Journal of Dynamic Systems, Measurement, and Control*, vol. 141, p. 104501, May 2019.

# Vita

Matthew Kieran Chu Cheong was born in Champs Fleurs, Trinidad on August 29 1991, the son of Dr. Keith Chu Cheong and Parbatee Chu Cheong. He received the Bachelor of Science in Engineering degree in Mechanical Engineering, as well as a certificate in Engineering Physics, from Princeton University in the Spring of 2013. He began his graduate studies at the University of Texas at Austin in the Fall of 2013.

Contact: mkchucheong@utexas.edu

This dissertation was typeset with LaTeX[†] by the author.

[†]LaTeX is a document preparation system developed by Leslie Lamport as a special version of Donald Knuth's TeX Program.